Summer 8-15-2019

Electron Decoupling with Chirped Microwave Pulses for Magic Angle Spinning Dynamic Nuclear Polarization Nuclear Magnetic Resonance Spectroscopy

Edward Paul Saliba
Washington University in St. Louis

WASHINGTON UNIVERSITY IN ST. LOUIS

Division of Chemistry

Dissertation Examination Committee:
Alexander Barnes, Chair
Joseph Ackerman
Sophia Hayes
Richard Loomis
Jacob Schaefer

Electron Decoupling with Chirped Microwave Pulses for Magic Angle Spinning Dynamic Nuclear Polarization Nuclear Magnetic Resonance Spectroscopy

by
Edward P. Saliba

A dissertation presented to
The Graduate School
of Washington University in
partial fulfillment of the
requirements for the degree
of Doctor of Philosophy

August 2019
St. Louis, Missouri

Table of Contents

List of Figures v

List of Tables x

Acknowledgments xi

Abstract of the Dissertation xiii

Chapter 1: Introduction 1

Chapter 2: Concepts and Instrumentation in Magnetic Resonance Spectroscopy 7

2.1 Nuclear Magnetic Resonance Spectroscopy 7

2.2 Terms in the Magnetic Resonance Hamiltonian Important to this Dissertation 8

2.2.1 The Zeeman Interaction 10

2.2.2 The Chemical Shielding Interaction 10

2.2.3 The Dipolar Coupling 11

2.2.4 The Fermi Contact Interaction 12

2.3 Dynamic Nuclear Polarization 12

2.3.1 Continuous Wave DNP Mechanisms 12

2.3.2 Time Domain DNP Mechanisms 14

2.4 Electron Decoupling 15

2.5 Adiabatic Inversions in Magnetic Resonance 15

2.5.1 Simulations of Adiabatic Inversions 15

2.5.2 The Adiabaticity Factor 17

2.6 Introduction to the Instrumentation for DNP and Electron Decoupling 19

2.6.1 Frequency Agile Gyrotron 20

2.6.2 MAS DNP NMR Transmission Line Probe 22

2.6.3 Cryostat 24

2.6.4 Heat Exchanger and Cryogenic MAS 26

2.7 DMfit 29

2.7.1 The Voigt Function 29

2.7.2 Least Squares Fitting Procedure 31

2.8 Analytical Powder Averaging Methods 34

References 36

Chapter 3: Pulsed Electron Decoupling and Strategies for Time Domain Dynamic Nuclear Polarization with Magic Angle Spinning 42

Forward 42
Abstract 43
3.1 Introduction 43
3.2 Dynamic Nuclear Polarization 44
3.2.1 The Integrated Solid Effect 49
3.2.2 Off Resonance NOVEL 53
3.2.3 Electron-Nuclear Cross Polarization 54
3.3 Electron Detected Magnetic Resonance 54
3.4 Electron Decoupling 55
3.5 Microwaves from a Frequency Agile Gyrotron 57
3.5.1 Improved Electron Nutation Frequencies with Teflon Lenses 61
3.5.2 Improved Electron Nutation Frequencies with Microwave Resonators 62
3.6 Cryogenic MAS DNP Technology 63
3.7 Conclusion 66
References 66
Chapter 4: Electron Decoupling with Dynamic Nuclear Polarization in Rotating Solids 76
Forward 76
Abstract 77
4.1 Introduction 77
4.2 Electron Decoupling Pulse Sequence 79
4.3 Results 82
4.4 Conclusion 88
References 89
Chapter 5: Electron Decoupling with Cross Polarization and Dynamic Nuclear Polarization Below 6 K 94
Forward 94
Abstract 95
5.1 Introduction 95
5.2 Experimental Methods 97
5.3 Results 102
5.3.1 High-Resolution DNP-NMR Below 6 K in Model Systems 102
5.3.2 Electron Decoupling with Cross Polarization 106
5.3.3 Electron Decoupling with Cross Polarization 108
5.4 Conclusions 109

References 110
Chapter 6: Fast Electron Paramagnetic Resonance Magic Angle Spinning Simulations Using Analytical Powder Averaging Techniques 116
Forward 116
Abstract 117
6.1 Introduction 118
6.2 Theory 121
6.2.1 Static TEMPO Powder Pattern 121
6.2.2 TEMPO Powder Pattern Under MAS 127
6.3 Simulations 134
6.4 Conclusions 142
References 143
Chapter 7: Conclusions and Outlook 149
7.1 Electron Decoupling 149
7.1.1 Conclusions 149
7.1.2 Outlook 150
7.2 Magic Angle Spinning Below 6 K with Liquid Helium 150
7.2.1 Conclusions 150
7.2.2 Outlook 150
7.3 Analytical Powder Averaging 151
7.3.1 Conclusions 151
7.3.2 Outlook 151
References 151

List of Figures

Figure 2.1: (a) The trajectory of the magnetization of the SA-BDPA unpaired electron under and adiabatic chirp of 840 kHz nutation frequency. (b) The z-component of the SA-BDPA during a 13.75 μs chirp with a perfectly homogeneous nutation field (dashed line) and with and inhomogeneous one (solid line). This figure was reproduced with modification from Hoff, D. E. M.; Albert, B. J.; Saliba, E. P.; Scott, F. J.; Choi, E. J.; Mardini, M.; Barnes, A. B. Frequency Swept Microwaves for Hyperfine Decoupling and Time Domain Dynamic Nuclear Polarization. *Solid State Nucl. Magn. Reson.* 2015, *72*[30]. ……16

Figure 2.2: The output frequency of a frequency agile gyrotron measured as a function of the accelerating voltage. This figure was reproduced from Scott, F. J.; Saliba, E. P.; Albert, B. J.; Alaniva, N.; Sesti, E. L.; Gao, C.; Golota, N. C.; Choi, E. J.; Jagtap, A. P.; Wittmann, J. J.; et al. Frequency-Agile Gyrotron for Electron Decoupling and Pulsed Dynamic Nuclear Polarization. *J. Magn. Reson.* 2018, *289*[1]. …21

Figure 2.3: a.) CAD drawing of a frequency agile gyrotron. b.) An expansion of (a) around the electron gun. c.) An expansion of (a) around the microwave cavity. d.) An expansion of (a) around the mode converter and window. This figure was reproduced with modification from Scott, F. J.; Saliba, E. P.; Albert, B. J.; Alaniva, N.; Sesti, E. L.; Gao, C.; Golota, N. C.; Choi, E. J.; Jagtap, A. P.; Wittmann, J. J.; et al. Frequency-Agile Gyrotron for Electron Decoupling and Pulsed Dynamic Nuclear Polarization. *J. Magn. Reson.* 2018, *289*[1]. ……22

Figure 2.4: a.) A basic design for an NMR probe. The tuning capacitor is used to set the resonance frequency of the circuit, and the matching capacitor is used to match the characteristic impedance of the transmission line to that of the source. The sample is in the coil and this circuit generates a large current through it to manipulate the nuclei with. b.) A CAD drawing of a portion of the circuit shown in (a). This figure was reproduced with modification from Scott, F. J.; Alaniva, N.; Golota, N. C.; Sesti, E. L.; Saliba, E. P.; Price, L. E.; Albert, B. J.; Chen, P.; Connor, R. D. O.; Barnes, A. B. A Versatile Custom Cryostat for Dynamic Nuclear Polarization Supports Multiple Cryogenic Magic Angle Spinning Transmission Line Probes. *J. Magn. Reson.* 2018, *297*, 23–32[2]. ……24

Figure 2.5: a.) A CAD drawing of the cryostat. b.) An expansion of the CAD drawing in (a) around the top of the cryostat, with the transfer lines and their supporting infrastructure shown. This figure was reproduced with modification from Scott, F. J.; Alaniva, N.; Golota, N. C.; Sesti, E. L.; Saliba, E. P.; Price, L. E.; Albert, B. J.; Chen, P.; Connor, R. D. O.; Barnes, A. B. A Versatile Custom Cryostat for Dynamic Nuclear Polarization Supports Multiple Cryogenic Magic Angle Spinning Transmission Line Probes. *J. Magn. Reson.* 2018, *297*, 23–32[2]. ……25

Figure 2.6: a.) A CAD drawing of the heat exchanger. b.) A CAD drawing of one of the 3 identical modules that is used to cool the MAS fluid. This figure was reproduced from Albert, B. J.; Pahng, S. H.; Alaniva, N.; Sesti, E. L.; Rand, P. W.; Saliba, E. P.; Scott, F. J.; Choi, E. J.; Barnes, A. B. Instrumentation for Cryogenic Magic Angle Spinning Dynamic Nuclear Polarization Using 90 L of Liquid Nitrogen per Day. *J. Magn. Reson.* 2017, *283*[31]……27

Figure 2.7: a.) A CAD drawing of the NMR magnet with the heat exchanger and helium dewar visible. b.) The Lakeshore units used to monitor MAS fluid temperatures. The sample temperature is boxed in red[3–6]. This figure was reproduced with modification from Albert, B. J.; Pahng, S. H.; Alaniva, N.; Sesti, E. L.; Rand, P. W.; Saliba, E. P.; Scott, F. J.; Choi, E. J.; Barnes, A. B. Instrumentation for Cryogenic Magic Angle Spinning Dynamic Nuclear Polarization Using 90 L of Liquid Nitrogen per Day. *J. Magn. Reson.* 2017, *283*[31]. ……28

Figure 2.8: The helium for the drive and bearing lines for MAS below 6 K is supplied by the compressed helium tanks pictured[4,6]. ……29

Figure 2.9: a.) A theoretical Voight function (red dots) fit using Equation 1.6. b.) An experimentally acquired urea spectrum fit using Equation 1.6. The agreement in both cases is excellent. ……34

Figure 2.10: The z-y-z Euler angle convention. The original reference frame is pictured in black. The coordinate axes following each successive rotation has had an additional prime added to their name. ……35

Figure 3.1: a) CP MAS enhancement spectra of 1 M U-^{13}C urea with 20 mM AMUPol at 81 K at 6 kHz. The ^{1}H enhancement was 328. The black curve is $100\times$ the signal obtained with no microwaves. The red curve denotes measurements taken with microwaves present. Figure reproduced with modifications with permission of the Journal of Magnetic Resonance. ……46

Figure 3.2: Microwaves drive zero quantum or double quantum forbidden transitions corresponding to the transitions shown. This representation of the solid effect assumes that the nucleus has a positive gyromagnetic ratio. The ket vectors are labeled as $|m_s m_I\rangle$. ……50

Figure 3.3: a.) A mildly unresolved solid effect enhancement profile for protons in 4 M [U-^{13}C,^{15}N] urea with 40 mM of the Finland Trityl radical (black). This figure was reproduced with modification with permission from the Journal of Magnetic Resonance[1]. Superimposed is the center frequency dependence of electron decoupling to demonstrate the location of the EPR spectrum of the radical (green). This figure was reproduced with modification with permission from the Journal of the American Chemical Society[7]. b.) Possible frequency swept ISE/off-resonance NOVEL pulse sequence. c.) Possible eNCP pulse sequence. Color gradients in Figures 2.3b and2. 3c indicate frequency chirped microwaves. d.) Proposed electron detected multiple dimensional pulse sequence. ……52

Figure 3.4: a) The ^{13}C Hahn-Echo pulse sequence used to demonstrate pulsed electron decoupling. b) Pulsed electron decoupling performed with a polarization time of 0.5 seconds. The linewidth is narrowed from 419 Hz to 371 Hz with pulsed electron decoupling: a narrowing of 48 Hz. c) Pulsed electron decoupling performed with a polarization time of 7 seconds. The linewidth is narrowed from 336 Hz to 309 Hz with pulsed electron decoupling: a narrowing of 27 Hz. Black spectra represent the ^{13}C signal obtained with no electron decoupling, while red spectra represent those obtained with pulsed electron decoupling. The sample is 4 M (U-^{13}C, ^{15}N) urea and 40 mM Trityl (Finland radical) in d-8 glycerol/D_2O/H_2O (60/30/10 by volume) at a sample volume of 30 µL in a 3.2 mm zirconia rotor. The experiments were conducted at 90 K and at a sample spinning frequency of 4 kHz. Figure reproduced with modifications by permission of the Journal of the American Chemical Society. ……57

Figure 3.5: a) Computer-Aided Design (CAD) drawing of a 198 GHz gyrotron. b) The gyrotron is connected by the wire highlighted in yellow to a low capacitance amplifier. c) The dependence of the gyrotron output frequency on the applied accelerating voltage. d) Rotor-synchronized microwave power output from the gyrotron. The rotor tachometer reading is shown in green, the gating voltage pulses in red, and the microwave power modulation in black. Figure reproduced with modifications by permission of the Journal of Magnetic Resonance. ……60

Figure 3.6: a) Simulated power distribution of a Gaussian beam exiting a waveguide. The white box indicates the sample location inside the rotor. b) Simulated effect on the power distribution after the Gaussian beam has passed through a cylindrical lens. c) Experimental verification of (a). d) Experimental verification of (b). Figure reproduced with modifications by permission of the Journal of Magnetic Resonance. ……61

Figure 3.7: Metalized rotors for MAS DNP. a) A rotor coated with copper by vacuum deposition. b) ^{13}C CPMAS spectrum of U-^{13}C sodium acetate at a spinning frequency of 5.4 kHz. The spectrum is an expansion around the carboxyl peak of sodium acetate. The red curve was taken with an uncoated rotor, and a copper coating is present in the blue spectrum. Figure reproduced with modifications with permission from Magnetic Resonance in Chemistry. ……63

Figure 3.8: Cryogenic technology used in DNP MAS NMR experiments from room temperature to 4.2 K. a) NMR probe head showing the path of the VT helium fluid (shown by the blue arrow) onto the sample. b) Heat exchanger that is used to cool drive, bearing, and VT fluids to 80-100 K. These figures were reproduced with permission from the Journal of Magnetic Resonance. ……65

Figure 4.1: Electron decoupling DNP NMR pulse sequence. On the electron channel, the microwave frequency is set to the zero quantum ^{13}C solid effect condition (197.715 GHz) for DNP. Electron decoupling is employed during the signal acquisition by sweeping over the electron resonance, centered at 197.640 GHz. ^{13}C magnetization is destroyed with a saturation train, which is followed by the DNP polarization time. The ^{13}C signal is acquired with a rotor synchronized Hahn echo (τ = 250 µs, $\omega_{1C}/2\pi$ = 83 KHz during pulses) and TPPM is used for proton decoupling with $\omega_{1H}/2\pi$ = 77 KHz. ……79

Figure 4.2: The anode voltage modulation used in electron decoupling experiments (a) and when electron decoupling is not performed for a control experiment (b). ……81

Figure 4.3: DNP MAS NMR spectra at 7 Tesla (^{13}C Larmor frequency of 75.495 MHz). (a) ^{13}C enhancement (without electron decoupling) with a 7 second polarization time. The enhancement is 242. (b) Comparison of DNP spectra with (red) and without (black) electron decoupling at a polarization time of 0.5 seconds. (c,d) Expansion of the isotropic urea resonance with 0.5 and 7.0 second polarization times. Electron decoupling exhibits increased NMR intensity and resonance narrowing at both polarization times. The un-normalized spectra show the intensity increase under electron decoupling. The normalized spectra show the decrease in linewidth. ……82

Figure 4.4: CPMG experiments performed without electron decoupling (top), and with electron decoupling (bottom) at 7 seconds of polarization time. ……84

Figure 4.5: Dependences of NMR linewidth differences with and without electron decoupling, $\Delta\omega_{eDEC}/2\pi$, on experimental parameters. The isotropic ^{13}C Urea resonance was fit using DMfit,[8] in which the Lorentzian vs. Gaussian composition was allowed to vary during the fit. Linewidths are reported as full width at half maximum (FWHM) (a) Dependence of electron decoupling on the polarization time. The change in $\Delta\omega_{eDEC}/2\pi$ increases drastically with polarization times below 20 seconds. (b) Dependence of electron decoupling on the center frequency of the decoupling sweeps, using a sweep width of 90 MHz. (c) Dependence of electron decoupling on the decoupling sweep width. $\Delta\omega_{eDEC}/2\pi$ has a maximum at a sweep width of 130 MHz. (d) Dependence of electron decoupling on microwave sweep time, τ_{SW}. ……85

Figure 5.1: (a) Cross-polarization magic angle spinning (CPMAS) with electron decoupling. (b) Proton-driven spin diffusion (PDSD) CPMAS. (c) The waveform input into an arbitrary waveform generator to produce the voltage sweeps to generate the frequency chirps on the gyrotron (black) and $0.001\times$ the voltage modulation actually output by the amplifier (red). ……101

Figure 5.2: DNP CPMAS NMR spectra below 6 K on model systems. (a), (b) Enhancement spectra of urea with AMUPol and trityl, respectively. Spectra in black represent no microwave irradiation while spectra in red are with microwave irradiation. T_{1DNP} of ^{1}H for urea with AMUPol (c) and trityl (d). (e), (f) Microwave power dependence on urea with AMUPol and trityl, respectively. 5.0 W of microwave power incident to the sample is shown in red and 0.23 W of microwave power is shown in black. * denote spinning side bands. ……104

Figure 5.3: Plots of the $\frac{h\nu_0}{2k_BT}$ dependence of the electron polarization commonly used in the high temperature limit (red) and the full Boltzmann expression for a spin $\frac{1}{2}$ particle, $\tanh\left(\frac{h\nu_0}{2k_BT}\right)$ (black). At 6 K the two have begun to non-negligibly deviate from one another. This deviation becomes even larger as the temperature is cooled further and the polarization of the electrons begins to approach unity. Here $h = 6.626\times10^{-34}Js$, $k_B = 1.38\times10^{-23}\frac{J}{K}$, $\nu_0 = 198\times10^{9}\ Hz$, and T is the temperature in Kelvin. The point on the Boltzmann polarization curve marks the polarization at 6 K where it is equal to 66%. ……105

Figure 5.4: Electron decoupling with cross polarization. (a) CP-DNP spectra of urea with trityl. (b) Carbonyl region from the ^{13}C spectrum of L-proline with trityl. Black spectra were recorded with no electron decoupling, while red spectra were recorded with electron decoupling. ……107

Figure 5.5: PDSD taken on [U-^{13}C, ^{15}N] L-proline with trityl below 6 K (a) and at 90 K (b). The 1D spectrum at the top of each figure is the slice of the 2D spectrum indicated by the dashed line. The total experiment time was 16 hours for the spectrum recorded at 90 K, while the experiment at 6 K required only 24 minutes. ……109

Figure 6.1: The TensorView Mathematica notebook was used to produce graphical representations of the ω-tensor, which is the effective tensor that is the result of the combined effects of the g-tensor and hyperfine coupling tensor. The TEMPO molecule is shown in (a) perpendicular to the N-O bond. The ω tensor superimposed on the TEMPO molecule is shown down the N-O bond for the $m=-1$ (b), $m=0$ (c), and $m=+1$ (d) cases. ……124

Figure 6.2: The first five Bessel functions (orders 0-4). The Bessel Functions contribute to the weighting factors in the Jacobi-Anger expansion used to produce an analytical solution for the integration over the α Euler angle. ……126

Figure 6.3: Simulations performed using only numerical integration for the powder average (a) and analytical integration over the α Euler angle (b). In (b), the individual powder patterns that correspond to each value of m for the ^{14}N nucleus are plotted. If the reduction in resources is considered, we observe a 97.5% reduction in simulation time using analytical averaging methods over numerical methods, with higher quality results. ……137

Figure 6.4: An example Fibonacci sphere. The Fibonacci Sphere is an extremely uniform distribution of points over a unit sphere, and was used to generate the powder set used for numerical averaging. The homogeneity of the distribution of powder angles helps to keep the number of required angles relatively low. ……138

Figure 6.5: (a) The spinning sideband manifolds produced in simulations of the TEMPO powder patterns for the $m = -1$ (green), $m = 0$ (blue), and $m = +1$ (black) states of the ^{14}N nucleus. The sum is shown in red. The insets show expansions of their respective powder patterns on the interval from -0.7 MHz to 0.7 MHz offset. (b) An expansion of the curves shown in (a) on the interval from -0.23 MHz to 0.23 MHz offset. The spinning sidebands (SSB) are spit by the spinning frequency of 150 kHz. ….139

Figure 6.6: (a) The TEMPO powder patterns corresponding to the $m = +1$ (black), $m = 0$ (blue), and $m = -1$ (green) states of the ^{14}N that the electron is coupled to under 1 MHz MAS superimposed on one another. The shadow effect allows each individual powder pattern to be seen. (b) An expansion of (a) about 0 MHz offset. The summed powder pattern is shown in red. Unlike Figure 5.5b, the spinning sideband manifolds are resolved from one another at the new spinning frequency. ……140

Figure 6.7: Simulations of the TEMPO powder pattern including the first term in Equation (5.37) (blue), the first 6 terms (green) and the first 10 terms (red). There is only a small difference between the one involving 6 terms and the one with 10 terms. The rapid convergence of the series in Equation (5.37) means that it can be heavily truncated to save time. ……141

List of Tables

Table 5.1: Experimental parameters used in the experiments described here. 98

Table 5.2: Effect of radicals and electron decoupling on linewidths of [U-^{13}C, ^{15}N] urea with and without trityl. Electron decoupling (eDEC) coupled with cross polarization (CP) results in ^{13}C linewidths approaching those without any radical present. 108

Acknowledgments

I would like to thank my advisor Alexander Barnes who provided me with many opportunities to advance my career such as going to conferences and nominating me for teaching awards and whose energy and determination was very inspiring. I always enjoyed having stimulating scientific discussions with him and he always made good suggestions about experiments, giving great advice.

I would also like to thank all of the other members of the Barnes Lab who have become my friends and have helped me throughout my Ph. D. work. I always had a lot of fun working with all of them.

Thank you also to Sophia Hayes, Richard Loomis, Jacob Schaefer, and Joseph Ackerman who are on my committee who guided me along the way and for useful discussions we have had.

I would like to give a special thanks to my Mom, Dad, and two brothers John and Andrew Saliba who have always supported me any way they could.

Funding was provided through the National Science Foundation Career Award CAREER DBI-1553577, The National Institutes of Health New Innovator Award DP2GM119131, the Graduate Assistance in Areas of National Need Fellowship, the Camille Dreyfus Teacher-Scholars Awards Program, and the National Center for Research Resources 1S10RR022984-01A1.

Edward P. Saliba

Washington University in St. Louis

August 2019

Dedicated to my family.

Abstract of the Dissertation

Electron Decoupling with Chirped Microwave Pulses for Magic Angle Spinning Dynamic Nuclear Polarization Nuclear Magnetic Resonance Spectroscopy by

Edward P. Saliba

Doctor of Philosophy in Chemistry

Chemistry

Washington University in St. Louis, 2019

Alexander Barnes, Chair

Dynamic nuclear polarization (DNP) is a method of generating hyperpolarization of nuclear spins for nuclear magnetic resonance (NMR) spectroscopy. Coherent, time domain techniques make the possibility of DNP directly to spins of interest at room temperature and higher feasible in magic angle spinning (MAS) NMR, allowing for optimal experimental repetition times to be limited by the T_1 of the electron, rather than a much longer T_{1DNP}, with excellent resolution. The strong hyperfine couplings that make such direct DNP transfers possible, however, can lead to short nuclear relaxation times that result in broadening of nuclear resonances and reduce sensitivity. This dissertation describes the implementation of electron decoupling, performed by rapidly chirping the irradiating microwave frequency through the electron resonance frequency of the narrow line Trityl Finland radical. The frequency chirps are produced by modulating the accelerating voltage of a frequency agile gyrotron. The voltage modulation is programed into the spectrometer arbitrary waveform generator using MATLAB. The experiments described here were performed both at a common DNP temperature of 90 K and with the first MAS experiments performed below 6 K. Experiments were performed using both direct polarization of the nuclei from the electrons, and with indirect polarization using cross polarization. Electron decoupling both narrows nuclear resonances and improves their integrated area. A method for performing analytical powder averaging for fast simulations of electron detected MAS DNP

experiments is also described, anticipating the incorporation of electron detection into magnetic resonance experiments under ultra-fast MAS for excellent sensitivity. The simulations are performed using a home written PYTHON code.

Chapter 1: Introduction

Nuclear magnetic resonance (NMR) spectroscopy is a powerful tool for investigating molecular structure and dynamics in a wide range of fields including pharmacology, materials science, biology, and others[1–3]. In solution state samples, anisotropic interactions are averaged to zero by rapid molecular tumbling. In solid samples, however, anisotropic interactions lead to broad resonances. Magic angle spinning (MAS), where the sample is rapidly spun at the "magic angle" of 54.74° with respect to the external magnetic field, can remove these anisotropic interactions, recovering the narrow resonances that makes NMR an important analytical technique[4]. One drawback to NMR, however, is that the energy splittings associated with nuclear spins in a magnetic field are typically much smaller than the thermal energy present. For this reason, many NMR experiments suffer from poor sensitivity[5–9].

One strategy to overcome the poor sensitivity of NMR is to use a technique called dynamic nuclear polarization (DNP)[5,6,10,11]. In DNP, a small amount of a radical is added to the sample. Upon irradiation with an appropriate frequency of microwaves, a large improvement in sensitivity is obtained as polarization is transferred from the electron spins to the nuclear spins. The same strong electron-nuclear (hyperfine) couplings that make DNP possible, however, can also lead to substantial broadening of nuclear resonances and shorten homogeneous relaxation times. Broadening of nuclear resonances decreases spectral resolution, and dipolar recoupling sequences such as rotational echo double resonance (REDOR) require long homogeneous relaxation times to achieve sufficient sensitivity[6–8].

Similar difficulties to those described above that are posed by the presence of unpaired electrons in a sample are also often encountered when ^{1}H nuclei are present. Because of this, ^{1}H decoupling is commonly applied, attenuating the strong magnetic interactions of the ^{1}H nuclei with the nuclei of interest. Many such decoupling schemes exist, such as CW, TPPM[12], WALTZ-16[13] and others.

Implementation of these decoupling methods for electron spins is complicated, however, by the difficulty of generating electron nutation frequencies sufficient to excite the entire bandwidth of most radicals at high magnetic fields and with magic angle spinning[1,7,14,15]. In static experiments, this is accomplished by using low magnetic fields to narrow g-factor broadened spectra, and by building microwave resonators to achieve high nutation frequencies with limited microwave power.

This dissertation describes the first electron decoupling experiments, where hyperfine couplings between the unpaired electrons on the radicals introduced for DNP and the observed ^{13}C nuclei are attenuated[1,7,14]. This is accomplished by use of frequency chirped microwave pulses which allow for broadband microwave irradiation[1,7,14–16]. The high power microwaves for electron decoupling and DNP are generated using a microwave source known as a gyrotron[17]. Electron decoupling has been performed using both direct polarization of the carbons from the electrons, and indirectly by first polarizing the protons, following this with cross polarization (CP) [1,7,14]. Surprisingly, in addition to a narrowing of the nuclear resonances, electron decoupling also improves their integrated area, leading to an improvement in sensitivity. When direct

polarization of the carbons in urea is employed, a reduction in linewidth of 48 Hz is observed with a 14% improvement in integrated area[14].

In addition to DNP, future MAS NMR experiments could utilize electron detection as another strategy to improve sensitivity. The Larmor frequency of an electron is $657\times$ that of a ^{1}H nucleus[1,7,14], and the amplitude of the voltage induced across an NMR coil increases with increasing frequency, leading to a better signal-to-noise ratio[18]. Simulations will aid in the design and optimization of these experiments. Modern solid state NMR simulations, however, can be quite lengthy, due to the number of powder angles that usually need to be included in the simulation.

In addition to the electron decoupling described above, this dissertation also discusses a new technique to quickly evaluate powder averages of certain systems in which the powder average is determined analytically over one of the Euler angles, rather than with more common numerical algorithms. This drastically reduces the size of the powder pattern needed to accurately characterize the powder pattern. The simulations performed use the g-value and hyperfine coupling values of the TEMPO nitroxide radical in both the static and MAS cases. In the static case, analytical powder averaging over the α Euler angle reduces the simulation time by 97.5%, if the reduction in resources from 8 computer processors to 1 is considered. In the MAS case, the resulting spinning sideband manifold has sidebands split by the simulated spinning frequency, as expected. Although the simulations performed here were done on the TEMPO radical, the techniques described are perfectly applicable to conventional NMR simulations as well.

(1) Saliba, E. P.; Sesti, E. L.; Alaniva, N.; Barnes, A. B. Pulsed Electron Decoupling and Strategies for Time Domain Dynamic Nuclear Polarization with Magic Angle Spinning. *J. Phys. Chem. Lett.* **2018**, *9*, 5539–5547.

(2) Hayes, S.; Van Wüllen, L.; Eckert, H.; Even, W. R.; Crocker, R. W.; Zhang, Z. Solid-State NMR Strategies for the Structural Investigation of Carbon-Based Anode Materials. *Chem. Mater.* **1997**, *9* (4), 901–911.

(3) Yang, H.; Staveness, D.; Ryckbosch, S. M.; Axtman, A. D.; Loy, B. A.; Barnes, A. B.; Pande, V. S.; Schaefer, J.; Wender, P. A.; Cegelski, L. REDOR NMR Reveals Multiple Conformers for a Protein Kinase c Ligand in a Membrane Environment. *ACS Cent. Sci.* **2018**, *4* (1), 89–96.

(4) Andrew, E. R. Magic Angle Spinning in Solid State n.m.r. Spectroscopy. *Philos. Trans. R. Soc. A Math. Phys. Eng. Sci.* **1981**, *299* (1452), 505–520.

(5) Judge, P. T.; Sesti, E. L.; Saliba, E. P.; Alaniva, N.; Halbritter, T.; Sigurdsson, S. T.; Barnes, A. B. Sensitivity Analysis of Magic Angle Spinning Dynamic Nuclear Polarization Below 6 K. *J. Magn. Reson.* **2019**.

(6) Alaniva, N.; Saliba, E. P. .; Sesti, E. L.; Judge, P. T.; Barnes, A. B. Electron Decoupling with Chirped Microwave Pulses for Rapid Signal Acquisition and Electron Saturation Recovery. *Angew. Chemie* **2019**.

(7) Sesti, E. L.; Saliba, E. P.; Alaniva, N.; Barnes, A. B. Electron Decoupling with Cross Polarization and Dynamic Nuclear Polarization below 6 K. *J. Magn. Reson.* **2018**, *295*, 1–5.

(8) Saliba, E. P.; Sesti, E. L.; Scott, F. J.; Albert, B. J.; Choi, E. J.; Alaniva, N.; Gao, C.; Barnes, A. B. Electron Decoupling with Dynamic Nuclear Polarization in Rotating Solids.

J. Am. Chem. Soc. **2017**, *139* (18), 6310–6313.

(9) Albert, B. J.; Gao, C.; Sesti, E. L.; Saliba, E. P.; Alaniva, N.; Scott, F. J.; Sigurdsson, S. T.; Barnes, A. B. Dynamic Nuclear Polarization Nuclear Magnetic Resonance in Human Cells Using Fluorescent Polarizing Agents. *Biochemistry* **2018**, *57* (31), 4741–4746.

(10) Wylie, B. J.; Dzikovski, B. G.; Pawsey, S.; Caporini, M.; Rosay, M.; Freed, J. H.; McDermott, A. E. Dynamic Nuclear Polarization of Membrane Proteins: Covalently Bound Spin-Labels at Protein-Protein Interfaces. *J. Biomol. NMR* **2015**, *61* (3–4), 361–367.

(11) Becerra, L. R.; Gerfen, G. J.; Temkin, R. J.; Singel, D. J.; Griffin, R. G. Dynamic Nuclear Polarization with a Cyclotron Resonance Maser at 5 T. *Phys. Rev. Lett.* **1993**, *71* (21), 3561–3564.

(12) Bennett, A. E.; Rienstra, C. M.; Auger, M.; Lakshmi, K. V.; Griffin, R. G. Heteronuclear Decoupling in Rotating Solids. *J. Chem. Phys.* **1995**, *103*, 6951.

(13) Shaka, A. J.; Keeler, J.; Freeman, R. Evaluation of a New Broadband Decoupling Sequence : **1983**, *340* (53), 313–340.

(14) Saliba, E. P.; Sesti, E. L.; Scott, F. J.; Albert, B. J.; Choi, E. J.; Alaniva, N.; Gao, C.; Barnes, A. B. Electron Decoupling with Dynamic Nuclear Polarization in Rotating Solids. *J. Am. Chem. Soc.* **2017**, *139* (18).

(15) Kupce, Ē.; Freeman, R. Stretched Adiabatic Pulses for Broadband Spin Inversion. *J. Magn. Reson. Ser. A* **1995**, *117* (2), 246–256.

(16) Luyten, P.; Ollander, D.; Heerschap, A. Broadband Proton Decoupling in Human 31P NMR Author Information Abstract MeSH Terms. *NMR Biomed.* **1989**, *1* (4), 177–183.

(17) Scott, F. J.; Saliba, E. P.; Albert, B. J.; Alaniva, N.; Sesti, E. L.; Gao, C.; Golota, N. C.;

Choi, E. J.; Jagtap, A. P.; Wittmann, J. J.; et al. Frequency-Agile Gyrotron for Electron Decoupling and Pulsed Dynamic Nuclear Polarization. *J. Magn. Reson.* **2018**, *289*.

(18) Levitt, M. H. *Spin Dynamics*, 2nd ed.; John Wiley & Sons Ltd.: West Sussex, 2008.

Chapter 2: Concepts and Instrumentation in Magnetic Resonance Spectroscopy

2.1 Nuclear Magnetic Resonance Spectroscopy

Nuclear magnetic resonance spectroscopy (NMR) is a powerful tool widely used for probing the structure and dynamics of a multitude of different chemical architectures including those studied in biochemistry, materials science, and pharmaceuticals[1–3]. In NMR, the sample is typically placed in a strong external magnetic field and radio frequency (RF) pulses are used to manipulate magnetically active nuclei[2,4–7]. The final signal is detected as a voltage across a coil in most NMR experiments, which is induced by the precession of the components of the spins' magnetic moments perpendicular to the external magnetic field[8–10]. In addition to generating the signal from spin precession, the external magnetic field is also usually used to initially polarize the spins. The degree of polarization can be determined through the use of Boltzmann statistics. For a spin 1/2 system, the polarization is given by Equation (2.1) below:

$$P = -\tanh\left(\frac{h\nu_0}{2k_BT}\right) \tag{2.1}$$

Here, h is Planck's constant, ν_0 is the nuclear Larmor frequency, k_B is Boltzmann's constant, and T is the temperature in Kelvin[1,11–13]. In NMR, the thermal energy, k_BT, is typically much greater than the energy splitting, $h\nu_0$. Because of this, the polarizations achieved are usually very small, leading to poor sensitivity when compared with other forms of spectroscopy[8–10].

In liquid state experiments, NMR usually has excellent resolution. However, the molecular tumbling that leads to this level of resolution is not present in solids. Broad powder patterns due

to the chemical shift anisotropy and dipolar interactions destroy the resolution observed in liquid spectra. Narrow resonances can be recovered, however, by rapidly spinning the sample at what is known as the "magic angle" of $\cos^{-1}\left(\frac{1}{\sqrt{3}}\right) = 54.74°$ with respect to the external magnetic field. This time-averages the second rank components of these tensor valued quantities to zero[14,15].

2.2 Terms in the Magnetic Resonance Hamiltonian Important to this Dissertation

The Hamiltonian ($\widehat{H}$) is the operator that describes the system energy. In general, Hamiltonians in NMR can be written in the lab frame in the form given by Equation (2.2)[15]:

$$\widehat{H} = \sum_{l=0}^{2} \sum_{m=-l}^{l} a_m^{(l)} \hat{s}_m^{(l)} \tag{2.2}$$

Here, the $a_m^{(l)}$'s are spatial functions that depend on the orientation of the system, and the $\hat{s}_m^{(l)}$'s are related to the spin operators of the spin and the magnetic field that they are interacting with. Fortuitously, in most magnetic resonance systems most of the terms either are identically 0 or very quickly average to 0 in the large external magnetic field. In this approximation, known as the secular approximation, the Hamiltonian takes the form shown in Equation (2.3)[15]:

$$\widehat{H} = a_0^{(0)} \hat{s}_0^{(0)} + a_0^{(2)} \hat{s}_0^{(2)} \tag{2.3}$$

Under the secular approximation, the Hamiltonian is reduced from nine terms to the much more manageable two. The $a_m^{(l)}$'s and $\hat{s}_m^{(l)}$'s are defined in Equations (2.4)-(2.7)[15]:

$$a_0^{(0)} = -\sqrt{3} a_{iso} \tag{2.4}$$

$$a_0^{(2)} = \frac{1}{2}\sqrt{\frac{3}{2}} a_{aniso}\left(3\cos^2(\beta) - 1 - \eta\sin^2(\beta)\cos(2\alpha)\right) \tag{2.5}$$

$$\hat{s}_0^{(0)} = -\frac{1}{\sqrt{3}}\left(\hat{O}_x\hat{I}_x + \hat{O}_y\hat{I}_y + \hat{O}_z\hat{I}_z\right) \tag{2.6}$$

$$\hat{s}_0^{(2)} = \frac{1}{\sqrt{6}}\left(2\hat{O}_z\hat{I}_z - \hat{O}_x\hat{I}_x - \hat{O}_y\hat{I}_y\right) \tag{2.7}$$

Here, $\hat{I}_x$, $\hat{I}_y$, and $\hat{I}_z$ are the spin operators that correspond to the spin of interest, and $\hat{O}_x$, $\hat{O}_y$, and $\hat{O}_z$ correspond to the components of the magnetic field that the spin is interacting with (for example, they may be the components of the external magnetic field or the spin operators of another spin). α and β are the Euler angles that describe the orientation of the principle axes of the interaction relative to the magnetic field. a_{iso}, a_{aniso}, η are defined in Equations (2.8)-(2.10) below[15]:

$$a_{iso} = \frac{1}{3}\left(a_{XX} + a_{YY} + a_{ZZ}\right) \tag{2.8}$$

$$a_{aniso} = a_{ZZ} - a_{iso} \tag{2.9}$$

$$\eta = \frac{a_{YY} - a_{XX}}{a_{aniso}} \tag{2.10}$$

Here, a_{XX}, a_{YY}, and a_{ZZ} are the principle axis components of the interaction. It should be noted that although the secular approximation is used here, nonsecular terms cannot always be discarded. For example, some DNP mechanisms depend on nonsecular terms for polarization transfer to happen. Some specific terms in the Hamiltonian are discussed below. Note that only

terms that are important to the work in this dissertation are described, and that this is not an exhaustive list.

2.2.1 The Zeeman Interaction

The Zeeman interaction is the energy associated with a bare nucleus or electron in the external magnetic field arising from its intrinsic spin. The Zeeman interaction is typically the largest interaction in the magnetic resonance Hamiltonian and is primarily responsible for the initial polarization of the spins[15]. The Zeeman interaction is usually considered to be a purely isotropic interaction, and if the magnetic field is taken to be aligned along the z-axis, then Equations (2.3)-(2.10) can be used to write the Zeeman Hamiltonian in the form given in Equation (2.11). $\hbar$ is the reduced Planck's constant, γ is the gyromagnetic ratio of the spin, and B_0 is the strength of the external magnetic field[15]:

$$\widehat{H}_{Zeeman} = -\hbar\gamma B_0 \hat{I}_z \tag{2.11}$$

2.2.2 The Chemical Shielding Interaction

The chemical shielding interaction arises from the fact that the spins that are observed in nuclear magnetic resonance are not bare nuclei, but are surrounded by a cloud of electrons. The electron cloud responds to the magnetic field in such a way as to slightly "cancel out" the Zeeman interaction. Differences in the electronic structure around nuclei in different environments create observable differences in the resonant frequency of the nuclei, allowing them to be distinguished in a spectrum[16]. The chemical shielding can be quantified with a number called the "shielding

parameter" (σ). It has both isotropic and anisotropic components. The chemical shielding Hamiltonian can be written using Equations (2.3)-(2.10) in the manner below[15]:

$$\widehat{H}_{CS} = \hbar\gamma B_0 \left[\sigma_{iso} + \frac{1}{2}\sigma_{aniso}\left(3\cos^2(\beta) - 1 - \eta\sin^2(\beta)\cos(2\alpha)\right)\right]\hat{I}_z \tag{2.12}$$

It should be noted that, from a practical point of view, the g-tensor portion of the electron Hamiltonian behaves in a similar manner to the sum of the Zeeman and chemical shielding interactions acting on a nucleus.

2.2.3 The Dipolar Coupling

The dipolar coupling arises from the interaction between different spins in the system. The dipolar coupling is important for two main reasons. Firstly, it is a source of broadening. This is the primary interaction that decoupling methods are intended to remove in solid samples. It can be useful, however, because it is inversely proportional to the cube of the distance between the spins and can be used as a ruler for measuring the distances between them[16,17]. When an electron and a nucleus are coupled to one another, this makes up part of what is known collectively as the "hyperfine coupling[1]." The Hamiltonian for the heteronuclear dipolar coupling, which this dissertation is primarily interested in, is shown below. Here, γ_1 is the gyromagnetic ratio of spin 1, γ_2 is the gyromagnetic ratio of spin 2, and r is the distance between them[15]:

$$\widehat{H}_{dip} = -\frac{\mu_0}{4\pi}\frac{\gamma_1\gamma_2\hbar^2}{r^3}\left(3\cos^2(\beta) - 1\right)\hat{I}_z\hat{S}_z \tag{2.13}$$

2.2.4 The Fermi Contact Interaction

The Fermi contact interaction is a largely isotropic interaction that arises from an electron occasionally being located in the same place as the nucleus. It is the isotropic part of the hyperfine coupling, and is analogous to the J-coupling of NMR. The Hamiltonian for the Fermi contact interaction is given in Equation (2.14) below[1,16]:

$$\widehat{H}_{Fermi} = \hbar A_{iso} \hat{I}_z \hat{S}_z \tag{2.14}$$

2.3 Dynamic Nuclear Polarization

One method to remedy the poor sensitivity of NMR is known as dynamic nuclear polarization (DNP). In DNP, a small amount of a stable radical is typically doped into the sample. The unpaired electron on a radical has a gyromagnetic ratio approximately $657\times$ that of a ^{1}H nucleus, leading to Boltzmann polarizations much larger than any nucleus. Upon irradiation with an appropriate frequency of microwaves, the sensitivity improves dramatically as the large Boltzmann polarization of the electrons is transferred to the nuclei. There are several mechanisms that can be used to perform DNP[18–22]. These can be divided into two classes: continuous wave (CW) DNP, and time domain DNP. DNP is discussed further in Chapters 3-5.

2.3.1 Continuous Wave DNP Mechanisms

Three of the most common DNP mechanisms used today are the continuous wave mechanisms known as the solid effect, cross effect, and Overhauser effect. In the solid effect, the microwave

frequency is set one nuclear Larmor frequency away from electron's resonance frequency. This drives a forbidden transition that causes an electron and a nucleus to flip simultaneously. This process creates hyperpolarization of the nuclei. In the cross effect, DNP is achieved by saturating one spin packet of electrons with microwave irradiation. This spin packet then undergoes three spin transitions with one nuclear spin and an electron from a separate spin packet one nuclear Larmor frequency away[1,21].

The cross effect and solid effect are both continuous wave mechanisms, where the microwaves are usually irradiating the sample at all times. This method has a couple of disadvantages. Firstly, continuous wave mechanisms are slow. In most samples, the electron longitudinal relaxation time at room temperature is far too short to perform efficient polarization transfers. For this reason, most DNP experiments are run at a temperature of 100 K or less. Not only does the cryogenic temperature vastly increase the technical requirements of experiments, but it can also lead to broadening of resonances, as the molecular motion that keeps resonances narrow is removed. Furthermore, the efficiency of the solid effect decreases proportionally with $1/B_0^2$, and the efficiency of the cross effect decreases proportionally with $1/B_0$, where B_0 is the strength of the external magnetic field. Time domain methods, on the other hand, are not predicted to have such detrimental field dependencies[23].

One continuous wave mechanism that actually improves with increasing magnetic field is the Overhauser effect, first demonstrated in insulating solids by Can et al.[24]. It arises from the difference in zero quantum and double quantum relaxation rates[25]. The enhancement obtained through the Overhauser effect tends to scale linearly with the magnetic field[24].

2.3.2 Time Domain DNP Mechanisms

Time domain DNP methods, which involve pulsed DNP and frequency chirped DNP, have been shown to be able to produce enhancements on samples up to room temperature. These include nuclear spin orientation via electron spin locking (NOVEL), off resonance NOVEL, and the integrated solid effect (ISE)[1,23,26–28]. All of these mechanisms are discussed further in Chapter 3. A further advantage of time domain mechanisms is that if the radical is tethered to spin of interest, placing the unpaired electron in direct dipolar contact with it, then the spin diffusion step, which is typically the rate limiting step in polarization, can be avoided. This will allow experiments to be repeated on a timescale comparable to the longitudinal relaxation time of the electron, rather than having to wait for a slow spin diffusion process to take place. The direct dipolar contact, however, will lead to substantial paramagnetic effects that broaden nuclear signals and shorten homogeneous T_2's. Electron decoupling will be necessary to remove these paramagnetic effects[1].

Although time domain DNP mechanisms have been used to produce enhancements up to room temperature, these experiments were performed in low magnetic fields with no magic angle spinning and using a microwave resonator. In MAS, the infrastructure used to spin the sample takes up the space that would normally be used for a microwave resonator. In order to make up for this, high power microwave sources are necessary to generate the requisite electron nutation frequencies for time domain DNP experiments[1]. Time domain DNP is discussed further in Chapter 3.

2.4 Electron Decoupling

DNP of nuclei directly coupled to unpaired electrons will require electron decoupling to remove strong paramagnetic effects[1]. Electron decoupling was produced by rapidly chirping the microwave frequency back and forth over the electron resonance frequency with the intent of performing a series of adiabatic inversions. In an adiabatic inversion, a long microwave pulse is applied to the sample with a simultaneous ramp of the microwave frequency[18,20]. Rather than rapidly inverting the magnetization, adiabatic methods slowly drag the magnetization from the positive z-axis to the negative z-axis, and in doing so can accomplish a high efficiency inversion of the magnetization with substantially less power than a hard pulse would require[1,18,20,29]. Although the microwave power available for these electron decoupling experiments was probably not sufficient to produce full adiabatic inversions of the electrons, the presence of the microwave chirps dramatically improved the effectiveness of the decoupling over the continuous wave case. Adiabatic inversions are discussed further in the next section. In order to perform the frequency chirps, as well as to perform electron decoupling in the same experiment as DNP, a frequency agile microwave source is required. The implementation of electron decoupling is the subject of Chapters 4 and 5.

2.5 Adiabatic Inversions in Magnetic Resonance

2.5.1 Simulations of Adiabatic Inversions

In an adiabatic inversion the microwave frequency is slowly swept over the resonance frequency of a spin, dragging its magnetization vector from the positive z-axis to the negative z-axis. A

simulated trajectory of the magnetization of the unpaired electron on the radical SA-BDPA is shown in Figure 2.1a. Figure 2.1b demonstrates another advantage of adiabatic methods: there insensitivity to microwave inhomogeneity. The dashed line in Figure 2.1b shows the z-component of the magnetization of the SA-BDPA radical during a 13.75 μs microwave chirp. The simulation assumes a perfectly homogenous nutation frequency of 840 kHz and a homogeneous T_2 of 3.3 μs. The simulation predicts that 57% of the initial magnetization of the Trityl will make it to the –z-axis using these parameters. The solid line is a simulation of an adiabatic inversion of the SA-BDPA magnetization with a distribution of nutation frequencies with an average of 840 kHz and a standard deviation of 200 kHz. In this case 46 % of the intial magnetization is predicted to make it to the –z-axis, which is still the majority of what was predicted in the uniform nutation field case.

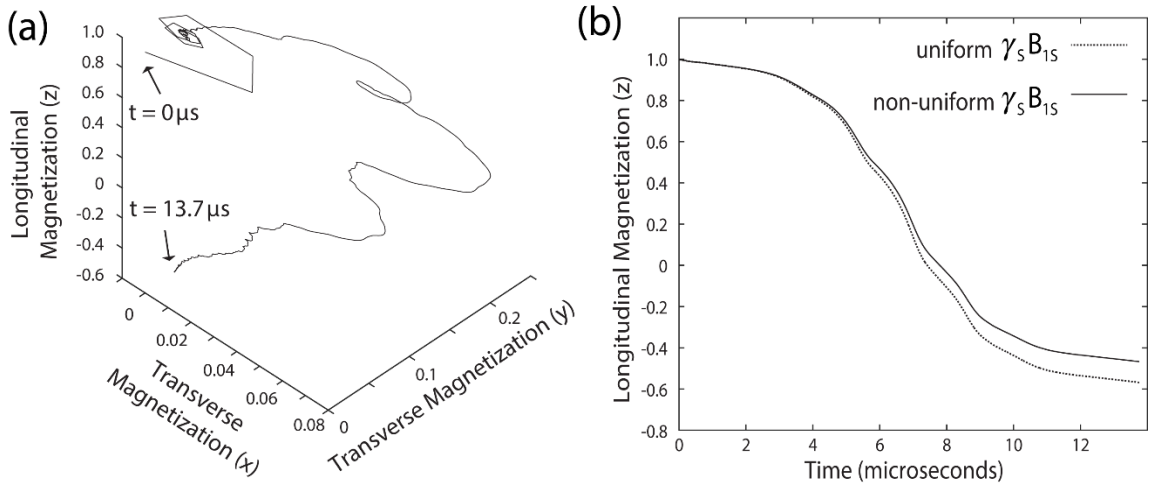

Figure 2.1: (a) The trajectory of the magnetization of the SA-BDPA unpaired electron under and adiabatic chirp of 840 kHz nutation frequency. (b) The z-component of the SA-BDPA during a 13.75 μs chirp with a perfectly homogeneous nutation field (dashed line) and with and inhomogeneous one (solid line). This figure was reproduced with modification from Hoff, D. E. M.; Albert, B. J.; Saliba, E. P.; Scott, F. J.; Choi, E. J.; Mardini, M.; Barnes, A. B. Frequency Swept Microwaves for Hyperfine Decoupling and Time Domain Dynamic Nuclear Polarization. *Solid State Nucl. Magn. Reson.* 2015, *72*[30]

2.5.2 The Adiabaticity Factor

This strategy allows for a much broader banded excitation than would typically be achievable with a hard pulse[18,30]. In addition to being the inspiration for the strategy used in electron decoupling, adiabatic techniques are also promising avenues for the implementation of time domain DNP. The "degree of adiabaticity" is typically quantified by the "adiabaticity factor", defined in Equation (2.15)[18,29,30]:

$$Q(t) = \left| \frac{\omega_{eff}(t)}{\frac{d\theta(t)}{dt}} \right| \tag{2.15}$$

Here, $\omega_{eff}(t)$ is the effective angular frequency experienced by the spin, an $\theta(t)$ is the angle of the magnetization with the x-y plane. Expressions for these quantities are given in Equations (2.16) and (2.17) below, respectively[18,29,30]:

$$\omega_{eff}(t) = \sqrt{\Delta\omega(t)^2 + \omega_1(t)^2} \tag{2.16}$$

$$\theta(t) = \tan^{-1}\left(\frac{\Delta\omega}{\omega_1}\right) \tag{2.17}$$

Here, $\Delta\omega$ is the offset of the angular frequency of the irradiating microwaves (in the case of DNP) and ω_1 is the nutation frequency of the spin. If these expressions are substituted in to Equation (2.15), Equation (2.18) is obtained[18,29,30]:

$$Q(t) = \left| \frac{\left(\Delta\omega(t)^2 + \omega_1(t)^2\right)^{3/2}}{\omega_1(t)\frac{d\Delta\omega(t)}{dt} - \Delta\omega(t)\frac{d\omega_1(t)}{dt}} \right| \tag{2.18}$$

For the work presented in this dissertation linear frequency chirps are used. In this case the offset of the microwave frequency is swept according to Equation (2.19) below[18,29,30]:

$$\Delta\omega(t) = k\left(t - \frac{1}{2}\tau\right) \tag{2.19}$$

Here, k is the sweep rate in $\frac{rad}{s^2}$, and τ is the sweep time in seconds. This can be substituted into Equation (2.18) with some rearrangement to give Equation (2.20)[18,29,30]. Here the nutation frequency of the spin is taken to be constant in time, making $\frac{d\omega_1}{dt} = 0$ rad/s^2:

$$Q(t) = \left| \frac{\left(k^2\left(t - \tau/2\right)^2 + \omega_1^2\right)^{3/2}}{\omega_1 k} \right| \tag{2.20}$$

The adiabaticity factor is usually used in conjunction with the Landau-Zener Theory of adiabatic transitions, and Landau Zener Theory only employs the minimum value of the adiabaticity factor[18,29,30]. The function in Equation (2.20) achieves its minimum value at $t = \tau/2$. The value that it achieves is given by Equation (2.21). The second equality gives the minimum adiabaticity in terms of ν_1 and $k_{Hz/s}$, the values corresponding to ω_1 and k in the more common units of Hz

and Hz/s, respectively. In the third equality, the substitution $k_{Hz/s} = \nu_{sw}/\tau$ has been made, where ν_{sw} is the sweep width[18,29,30]:

$$Q_{\min} = \frac{\omega_1^2}{k} = \frac{2\pi\nu_1^2}{k_{Hz./s}} = \frac{2\pi\nu_1^2\tau}{\nu_{sw}} \tag{2.21}$$

Typical parameters used in the experiments described in this dissertation are $\nu_1 = 380 \times 10^3$ Hz, $\tau = 13.75 \times 10^{-6}$ s, and $\nu_{sw} = 87 \times 10^6$ Hz. Using these values in Equation (2.21) yields a minimum value of the adiabaticity factor of 0.14. For full adiabatic inversions, the adiabaticity factor should be around 5 at a minimum. More microwave power will improve the nutation frequency, and make for a higher adiabaticity factor. Further improvements can be made by using shaped microwave chirps, such as in a tangential sweep of the microwave frequency with time[18,29,30].

2.6 Introduction to the Instrumentation for DNP and Electron Decoupling

In order to perform DNP and electron decoupling, a large amount of custom instrumentation is required. This includes a frequency agile gyrotron to generate microwaves, a waveguide to direct the microwaves to the sample, a probe capable of operating at cryogenic temperatures, a cryostat to protect the inside of the magnet from cryogenic fluids, and a heat exchanger for cooling the sample to cryogenic temperatures[31–33]. This section is meant to provide an introduction to the operation and basic theory of the instrumentation previously designed in the Barnes lab that I used to perform my experiments.

2.6.1 Frequency Agile Gyrotron

A gyrotron is a vacuum tube placed inside of a large external magnetic field for generating high power microwaves. At the base of the gyrotron is an electron gun that consists of an anode and a cathode[18,20,32]. The cathode is heated to ~800° C, and has a large potential of about -12 kV relative to ground pulled on it. This causes a beam of electrons to be emitted from the electron gun. As the electrons travel through the magnetic field, they tend to gyrate under a Lorentz force, an expression for which is given by Equation (2.22) below[34]:

$$\vec{F} = q\left(\vec{E} + \vec{v} \times \vec{B}\right) \tag{2.22}$$

Here, $\vec{F}$ is the force acting on the electron, q is the electric charge of the particle (here it is equal to the negative of the elementary charge), $\vec{E}$ is the electric field, and $\vec{B}$ is the magnetic field. When an appropriate accelerating voltage is applied, the gyration of the electrons due to the Lorentz force will resonate with the interaction cavity of the gyrotron and generate microwaves. The voltages applied across the electron gun are sufficient to accelerate the electrons to mildly relativistic speeds[34]. The dependence of the frequency on the accelerating voltage of a typical gyrotron is demonstrated by Figure 2.2.

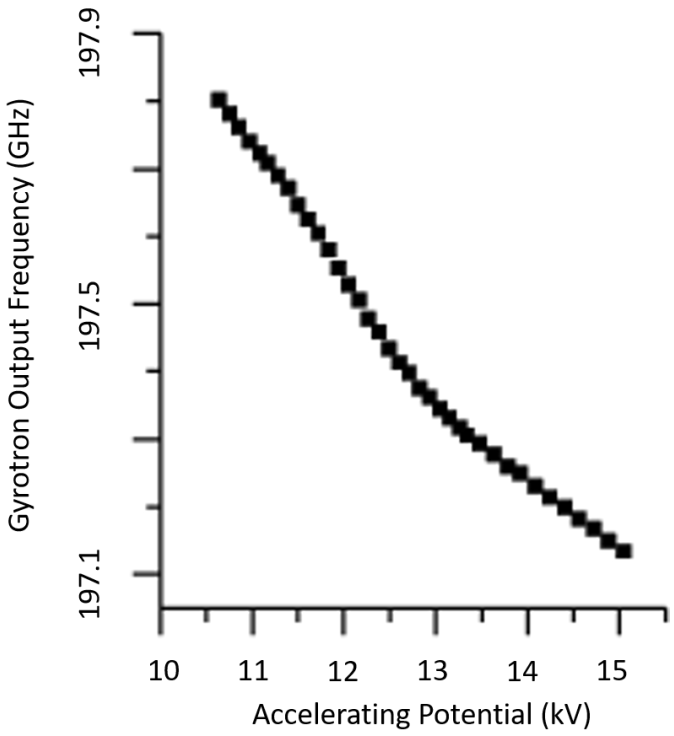

Figure 2.2: The output frequency of a frequency agile gyrotron measured as a function of the accelerating voltage. This figure was reproduced from Scott, F. J.; Saliba, E. P.; Albert, B. J.; Alaniva, N.; Sesti, E. L.; Gao, C.; Golota, N. C.; Choi, E. J.; Jagtap, A. P.; Wittmann, J. J.; et al. Frequency-Agile Gyrotron for Electron Decoupling and Pulsed Dynamic Nuclear Polarization. *J. Magn. Reson.* 2018, *289*[32].

The microwaves are generated in a transverse electric (TE) 5,2 mode[32]. This does not propagate well through the open space between the window and the waveguide, and for this reason a "mode converter" composed of a helically cut copper tube known as a "Vlaslov launcher" and a series of copper mirrors is used to convert the beam to a Gaussian mode. The microwaves propagate a sort distance through open space (~1 cm) before entering a waveguide. The waveguide directs the microwaves to the sample. A computer aided design (CAD) drawing of a gyrotron is shown in Figure 2.3 a. Expansions about the electron gun (b), interaction cavity (c) and the mode converter and window (d) are also pictured[32].

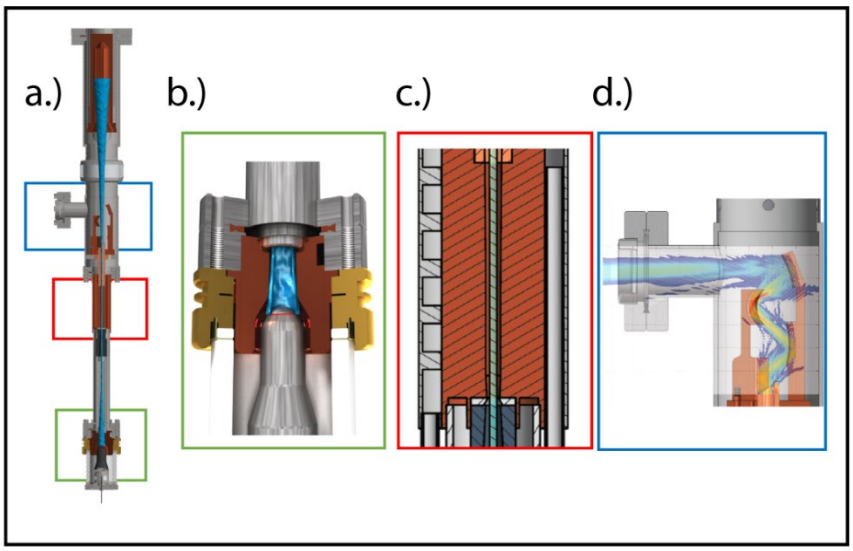

Figure 2.3: a.) CAD drawing of a frequency agile gyrotron. b.) An expansion of (a) around the electron gun. c.) An expansion of (a) around the microwave cavity. d.) An expansion of (a) around the mode converter and window. This figure was reproduced with modification from Scott, F. J.; Saliba, E. P.; Albert, B. J.; Alaniva, N.; Sesti, E. L.; Gao, C.; Golota, N. C.; Choi, E. J.; Jagtap, A. P.; Wittmann, J. J.; et al. Frequency-Agile Gyrotron for Electron Decoupling and Pulsed Dynamic Nuclear Polarization. *J. Magn. Reson.* 2018, *289*[32].

The dependence of the output frequency of the gyrotron on the voltage applied at the electron gun is key to being able to move the frequency from the DNP condition to the electron resonance frequency, and to perform the frequency chirps necessary for electron decoupling[18]. This is discussed further in Chapters 3-5.

2.6.2 MAS DNP NMR Transmission Line Probe

RF pulses to the sample and detection of the signal under MAS is achieved using a Schaefer-Mckay style transmission line probe. Such a probe is primarily constructed out of two coaxial copper tubes with the ratio of the diameters of the inner and outer conductors set to match the transmission line to 50 Ω of impedance. The Schaefer-Mckay style transmission line probe has

two major advantageous over traditional designs. Firstly, it allows for the transmission of large amounts of RF power, and secondly it allows for many different nuclei to be studied with relative ease on the same probe. This is accomplished by setting up a standing wave between the coil of the probe and the tuning capacitor for each channel. Subsequent channels can be added at the nodes of existing channels without interfering with them to a large extent.

Although the Schaefer-Mckay style transmission line probe has major advantages over other probe designs, its basic circuit setup is just like other common NMR probe design. This basic design is shown in Figure 2.4 a. A high alternating voltage is supplied from an amplifier that amplifies an RF pulse from the spectrometer ($V_{source} \approx 100\ V$). When the tuning capacitor in the "tank circuit" , C_{tune}, is set to the correct capacitance, it will resonate with the coil at the frequency input from the voltage source. The matching capacitor is then used to match the characteristic impedance of the probe to the impedance of the voltage source, which maximizes the power delivered to the tank circuit, of which the coil (with an inductance, L) is part. Such a design allows for large currents to be generated in the tank circuit ($\approx 50\ amps$) while the voltage source only sees a relatively small current pass through it. ($\approx 2\ amps$). The impedance of the source is equal to its internal resistance which is standardized at $50\ \Omega$. The resistance of the tank circuit is represented by R_{load}. The dashed box indicates components outside of the probe. A CAD drawing of how the tuning and matching capacitors are actually situated in the probe is shown in Figure 2.4 b. The actual coil used for NMR is further down the transmission line formed by the inner and outer conductors and is not pictured. The coils that are pictured are part of the traps used to prevent RF power from the other channels from going down this channel.

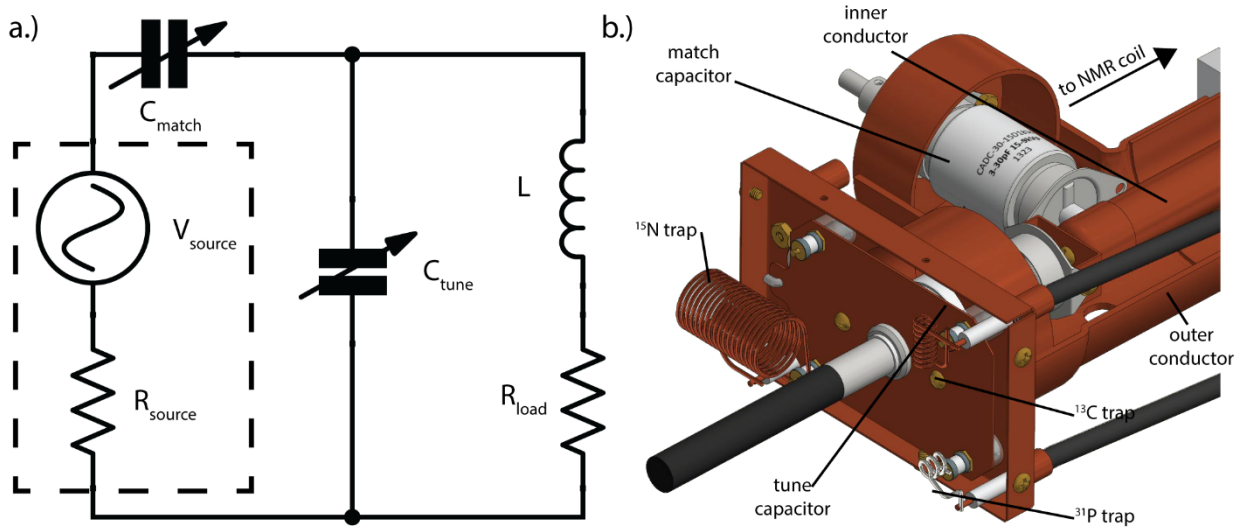

Figure 2.4: a.) A basic design for an NMR probe. The tuning capacitor is used to set the resonance frequency of the circuit, and the matching capacitor is used to match the characteristic impedance of the transmission line to that of the source. The sample is in the coil and this circuit generates a large current through it to manipulate the nuclei with. b.) A CAD drawing of a portion of the circuit shown in (a). This figure was reproduced with modification from Scott, F. J.; Alaniva, N.; Golota, N. C.; Sesti, E. L.; Saliba, E. P.; Price, L. E.; Albert, B. J.; Chen, P.; Connor, R. D. O.; Barnes, A. B. A Versatile Custom Cryostat for Dynamic Nuclear Polarization Supports Multiple Cryogenic Magic Angle Spinning Transmission Line Probes. *J. Magn. Reson.* 2018, *297*, 23–32[33].

2.6.3 Cryostat

The sample typically needs to be maintained at cryogenic temperatures for DNP to work. The magnet bore cannot be exposed to these temperatures, however, and so a cryostat is used to protect the inside of the magnet from the cryogenic gases that are blowing on the sample. A CAD drawing of the cryostat is shown in Figure 2.5 a[33]. A vacuum port at the bottom of the cryostat allows for a vacuum to be established between the two inner brass walls of about 5×10^{-8} torr. This vacuum acts as an excellent insulator, as very little heat can flow across a high vacuum. Ports at the top of the cryostat allow for the waveguide, sample eject lines, and

cryogenic transfer lines to be inserted into it through the aluminum top cap. A cross section of the top of the cryostat with the various brass lines inserted into it is shown in Figure 2.5 b[33]. Before being placed through the ports at the top of the cryostat, the brass lines are first passed through a brass plate, and an o-ring is placed on each line beneath the plate. All of the lines are then placed through the ports on the cryostat. Three threaded rods (one of which is shown in Figure 2.5 b) are screwed through a brass plate attached to the top of the magnet and used to compress the o-rings to form a tight seal[33].

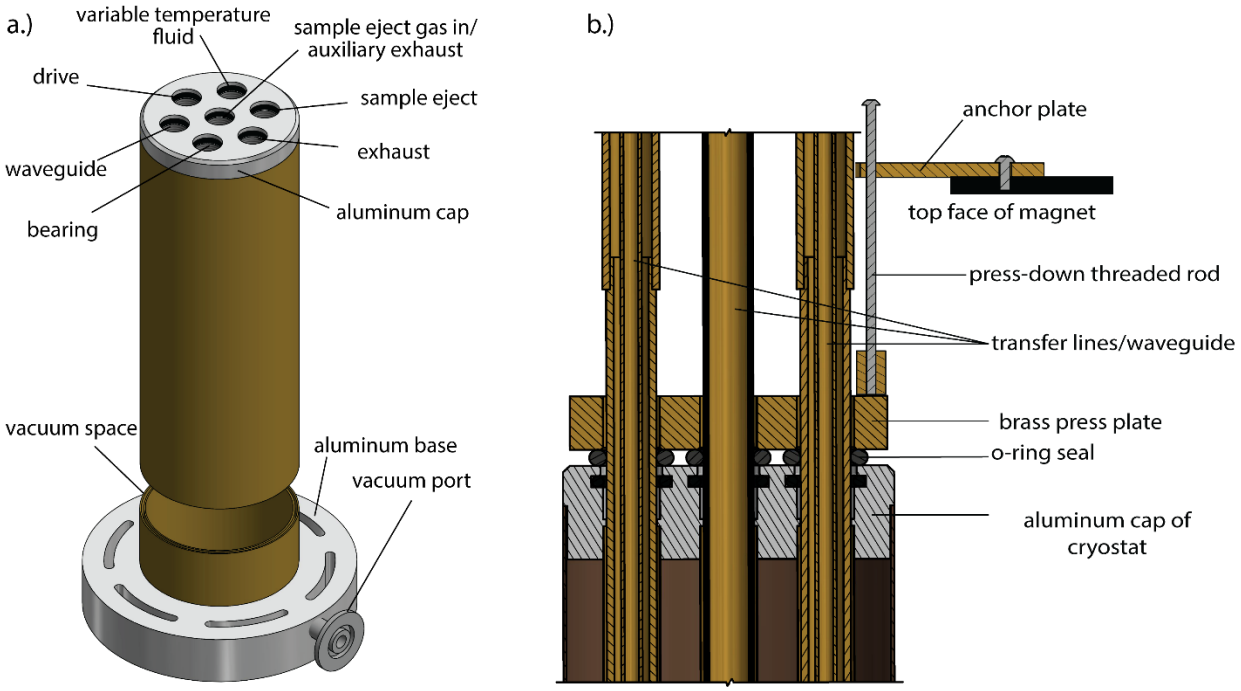

Figure 2.5: a.) A CAD drawing of the cryostat. b.) An expansion of the CAD drawing in (a) around the top of the cryostat, with the transfer lines and their supporting infrastructure shown. This figure was reproduced with modification from Scott, F. J.; Alaniva, N.; Golota, N. C.; Sesti, E. L.; Saliba, E. P.; Price, L. E.; Albert, B. J.; Chen, P.; Connor, R. D. O.; Barnes, A. B. A Versatile Custom Cryostat for Dynamic Nuclear Polarization Supports Multiple Cryogenic Magic Angle Spinning Transmission Line Probes. *J. Magn. Reson.* 2018, *297*, 23–32[33].

2.6.4 Heat Exchanger and Cryogenic MAS

The heat exchanger used to cool the samples is shown in Figure 2.6 a[35]. The heat exchanger is composed of a large, cylindrical, stainless steel dewar. At the top of the dewar is a piece of G-10 that supports three stainless steel modules for cooling the MAS fluid: one for the drive gas, one for the bearing gas, and one for the variable temperature fluid[35]. A CAD drawing of one of these modules is shown in Figure 2.6 b[35]. The dewar is filled with liquid nitrogen until the bottom can on each module is submerged. When using nitrogen as an MAS fluid, the nitrogen is purified from the air and 1/3 of it is sent to each of the modules. In the modules, the nitrogen is first cooled by the ~100 K nitrogen returning from the probe in the pre-cooling stage using a counter flow system, shown in green in Figure 2.6 b[35]. The nitrogen then flows into the main cooling stage in the can in the bottom of the module, where a variable density of gaseous nitrogen controlled by pressure regulators outside the module allows for control of the degree of thermal contact between the gas flowing through the coil and the nitrogen bath in the dewar. Once the nitrogen has been cooled to ~90 K, it flows through a vacuum jacketed transfer line (not shown) to the probe. The gas then leaves the probe head through an exhaust line where it goes back to the heat exchanger module to pre-cool the new nitrogen coming in[35].

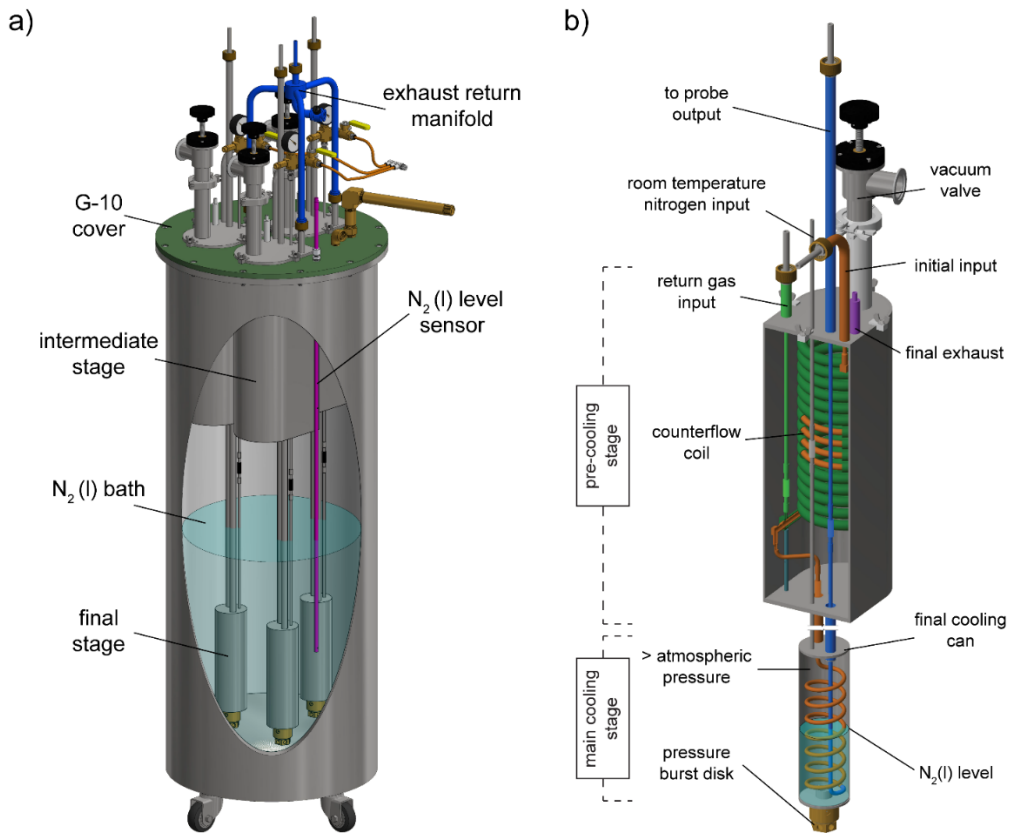

Figure 2.6: a.) A CAD drawing of the heat exchanger. b.) A CAD drawing of one of the 3 identical modules that is used to cool the MAS fluid. This figure was reproduced from Albert, B. J.; Pahng, S. H.; Alaniva, N.; Sesti, E. L.; Rand, P. W.; Saliba, E. P.; Scott, F. J.; Choi, E. J.; Barnes, A. B. Instrumentation for Cryogenic Magic Angle Spinning Dynamic Nuclear Polarization Using 90 L of Liquid Nitrogen per Day. *J. Magn. Reson.* 2017, *283*[31].

Nitrogen is used as an MAS fluid when experiments are performed at ~90 K[18,20,36–39]. Experiments performed below 6 K require helium to be used as an MAS fluid. In this case the variable temperature line is replaced by a new one that carries liquid helium from a dewar to the sample (Figure 2.7 a)[35]. When the liquid helium blows on the side of the rotor, it cools the sample below 6 K. The actual reading on the Cernox temperature sensor right next to the sample reads ~4.4 K, as shown by the boxed temperature readout in Figure 2.7 b[20,39].

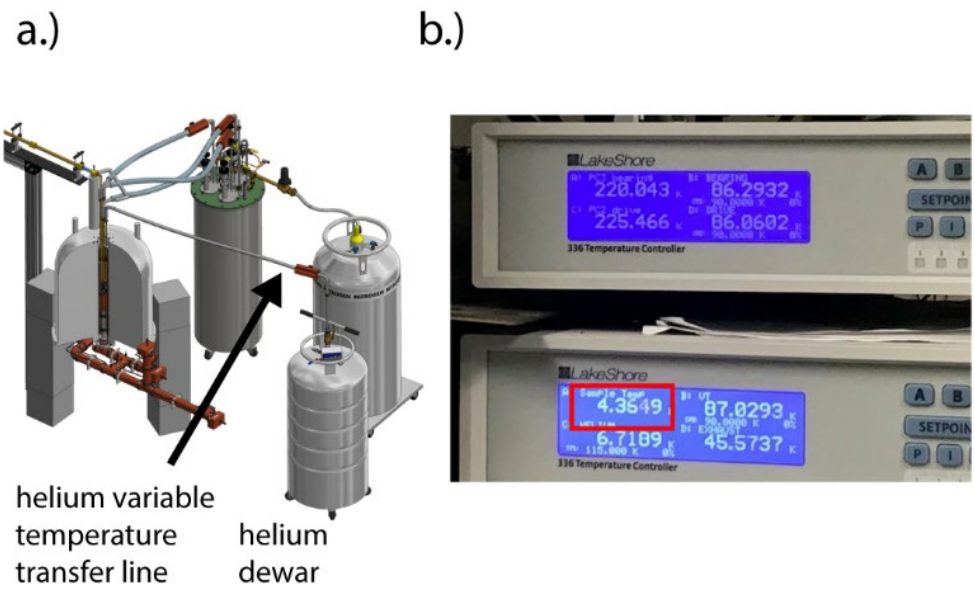

Figure 2.7: a.) A CAD drawing of the NMR magnet with the heat exchanger and helium dewar visible. b.) The Lakeshore units used to monitor MAS fluid temperatures. The sample temperature is boxed in red[20,31,39,40]. This figure was reproduced with modification from Albert, B. J.; Pahng, S. H.; Alaniva, N.; Sesti, E. L.; Rand, P. W.; Saliba, E. P.; Scott, F. J.; Choi, E. J.; Barnes, A. B. Instrumentation for Cryogenic Magic Angle Spinning Dynamic Nuclear Polarization Using 90 L of Liquid Nitrogen per Day. *J. Magn. Reson.* 2017, *283*[31].

When performing MAS below 6 K, the drive and bearing gasses are supplied by the compressed helium tanks shown in Figure 2.8[20,39]. A series of tubes leads from the helium tanks to a manifold of valves (boxed in red) that allows for new tanks to be switched in while the experiment is being performed without having to stop and waste the valuable liquid helium blowing onto the rotor[20,39]. Another tube leads from there to a purging valve for eliminating air from the system (boxed in yellow). The helium finally goes through a tube to the heat exchanger, where it is cooled from room temperature to 77 K[20,39]. Magic angle spinning below 6 K is discussed further in Chapters 3 and 5.

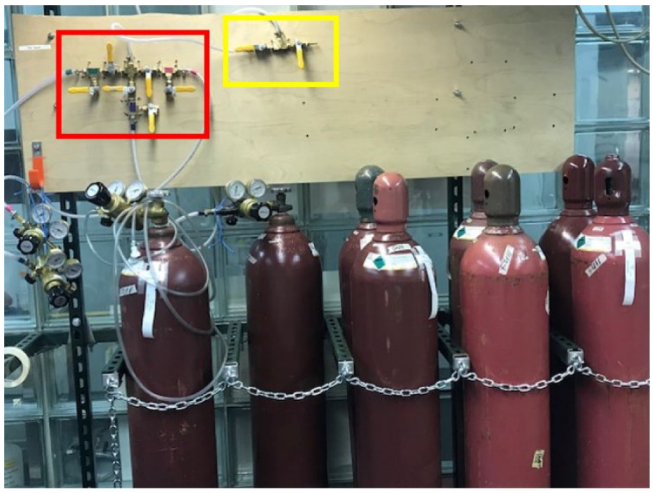

Figure 2.8: The helium for the drive and bearing lines for MAS below 6 K is supplied by the compressed helium tanks pictured[20,39].

2.7 DMfit

DMfit[41] is a program used to fit NMR spectra. Parameters such as the linewidth and integrated area of the resonances presented here were extracted from the fits provided by DMfit. What follows is a description of NMR lineshapes and how DMfit fits them.

2.7.1 The Voigt Function

A magnetic resonance lineshape is given by a Voigt function, the functional form of which can be defined as the convolution of a Gaussian ($G(\nu)$) and a Lorentzian ($L(\nu)$) as shown in Equation (2.23):

$$V(\nu) = A\left[\frac{\int_{-\infty}^{\infty} G(\nu')L(\nu-\nu')d\nu'}{\int_{-\infty}^{\infty} G(\nu')L(\nu_0-\nu')d\nu'}\right] \tag{2.23}$$

In Equation (2.23), $V(\nu)$ is the Voigt function, ν is the frequency, ν_0 is the center of the profile, A is the maximum height, and ν' is a dummy integration variable. The shape is dictated by the

integral in the numerator and the integral in the denominator makes sure that the maximum height of the function is equal to A. The functional forms of the Gaussian and Lorentzian functions are given by Equations (2.24) and (2.25), respectively:

$$G(\nu) = \exp\left(-4\ln(2)\left(\frac{\nu-\nu_0}{F_G}\right)^2\right) \tag{2.24}$$

$$L(\nu) = \frac{1}{1+4\left(\frac{\nu-\nu_0}{F_L}\right)^2} \tag{2.25}$$

Here, F_G and F_L are the full width at half maximum of the Gaussian and Lorentzian functions, respectively.

DMfit uses an approximation of the Voigt function that is described by a linear combination of a Gaussian and Lorentzian function, rather than their convolution. Such a function is given by Equation (2.26)[41]:

$$V(\nu) \approx A\left[g\exp\left(-4\ln(2)\left(\frac{\nu-\nu_0}{F}\right)^2\right)+(1-g)\frac{1}{1+4\left(\frac{\nu-\nu_0}{F}\right)^2}\right] \tag{2.26}$$

Here, g is the "Gaussian/Lorentzian ratio" defined in the program, and acts as a weighting factor that determines the amplitudes of the Gaussian and Lorentzian functions used. A is the amplitude, ν the frequency, and ν_0 the frequency of the maximum of the function as described previously. The full width at half maximum is taken to be $F_g = F_L = F$.

2.7.2 Least Squares Fitting Procedure

The fitting parameters given by DMfit can be obtained using a least squares fitting procedure. In order to perform a least squares fit, the gradient of the function to be fit with respect to the fitting parameters first needs to be determined. This is done in the expressions given in Equations (2.27)-(2.30), where the V_i's and ν_i's are the value of the Voigt function and the corresponding frequencies determined by the spectrometer, respectively:

$$\frac{\partial V_i}{\partial A} = g\exp\left(-4\ln(2)\left(\frac{\nu_i-\nu_0}{F}\right)^2\right)+(1-g)\frac{1}{1+4\left(\frac{\nu_i-\nu_0}{F}\right)^2} \tag{2.27}$$

$$\frac{\partial V_i}{\partial g} = A\left[\exp\left(-4\ln(2)\left(\frac{\nu_i-\nu_0}{F}\right)^2\right)-\frac{1}{1+4\left(\frac{\nu_i-\nu_0}{F}\right)^2}\right] \tag{2.28}$$

$$\frac{\partial V_i}{\partial \nu_0} = A\left[g\left(\frac{8\ln(2)(\nu_i-\nu_0)}{F^2}\right)\exp\left(-4\ln(2)\left(\frac{\nu_i-\nu_0}{F}\right)^2\right)+(1-g)\left(\frac{8(\nu_i-\nu_0)}{F^2}\right)\frac{1}{\left[1+4\left(\frac{\nu_i-\nu_0}{F}\right)^2\right]^2}\right] \tag{2.29}$$

$$\frac{\partial V_i}{\partial F} = A\left[g\left(\frac{8\ln(2)(\nu_i-\nu_0)^2}{F^3}\right)\exp\left(-4\ln(2)\left(\frac{\nu_i-\nu_0}{F}\right)^2\right)+(1-g)\left(\frac{8(\nu_i-\nu_0)^2}{F^3}\right)\frac{1}{\left[1+4\left(\frac{\nu_i-\nu_0}{F}\right)^2\right]^2}\right] \tag{2.30}$$

These equations describe a matrix known as the Jacobian, whose columns are the derivatives of $V(\nu)$ evaluated at each frequency with respect to each fitting parameter. Guesses for each value provide initial values for the matrix elements of the Jacobian. Although the guesses should not be extremely far from the true values, the least squares fitting algorithm is quite robust to errors in the initial guesses.

The guess values for the fitting parameters can also be used to determine the values of all of the residuals (r_i), which are the differences between each point predicted by the fit and the actual, experimental values. These are given by Equation (2.31):

$$r_i = V(\nu_i) - V_i \tag{2.31}$$

From here, the optimal values for the fitting parameters can be solved for iteratively using the Newton-Gauss Method defined by Equation (2.32):

$$\vec{\beta}_n = \vec{\beta}_{n-1} - (J^T J)^{-1} J^T \vec{r} \tag{2.32}$$

Here, $\vec{\beta}$ is a vector of the fitting coefficients (A,g,ν_0, and F), J is the Jacobian matrix, and $\vec{r}$ is the vector of residuals. After each iteration, the fitting parameters are updated in $\vec{\beta}$, and the new

values are used to reevaluate J and $\vec{r}$. This algorithm usually has excellent convergence properties and an accurate answer can be obtained in only a handful of iterations.

The red dots in Figure 2.9a are points lying on a theoretical Voigt function using Equation (2.23) . The parameters used to produce the Voigt function were: $A = 1{,}000$, $F_G = 100\ Hz$, $F_L = 100\ Hz$, $\nu_0 = 0\ Hz$. The full width at half max of a Voigt in terms of the individual linewidths is given to excellent approximation in Equation (2.33)[42]:

$$F = 0.5346F_L + \sqrt{0.2166F_L^2 + F_G^2} \tag{2.33}$$

Using this equation, the full width half max of the theoretical Voigt function is approximately 163.76 Hz.

The blue line is the best fit to this Voigt function using Equation 1.6. The optimal fitting parameters as determined by a least squares fit and are: $A = 1007.27$, $g = 0.40$, $\nu_0 = -1.03 \times 10^{-4}\ Hz$ and $F = 163.09\ Hz$. These are in excellent agreement with the simulated values. The R^2 value for this fit is 1.00. The red points in Figure 2.8b are an experimentally acquired urea spectrum, fit using Equation (2.26). The optimal fitting parameters as determined by a least squares fit and are: $A = 175{,}242.01$, $g = 0.49$, $\nu_0 = -3{,}537.56\ Hz$ and $F = 246.17\ Hz$. The R^2 value is 1.00.

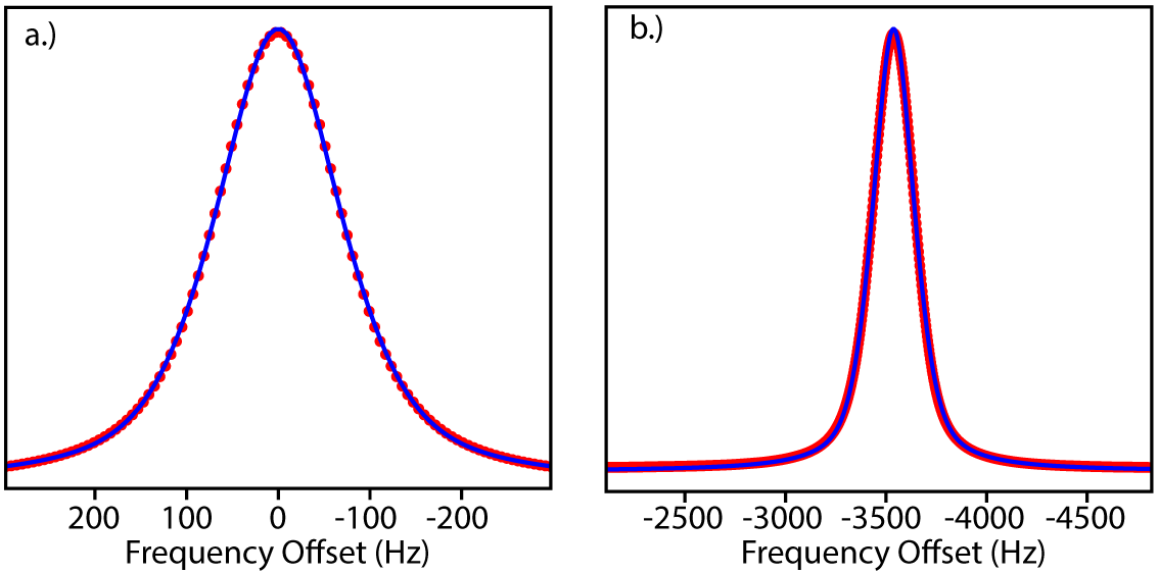

Figure 2.9: a.) A theoretical Voight function (red dots) fit using Equation (2.26). b.) An experimentally acquired urea spectrum fit using Equation (2.26). The agreement in both cases is excellent.

2.8 Analytical Powder Averaging Methods

Simulations are commonly used in magnetic resonance to design experiments and interpret data. These simulations, however, can be quite time consuming. In a solid powder, the molecules are oriented in a random distribution with respect to the main magnetic field. These powder orientations are described by a series of three "Euler angles." There are many ways that the Euler angles are defined, but the most common is known as the "z-y-z" convention. This is pictured in Figure 2.9[15]. In this convention, a set of coordinate axes fixed on the object to be rotated begins aligned with an initial coordinate frame (unprimed, in black). For the purposes of magnetic resonance, this usually means the principle axis frame of one of the interactions present in the system. The object fixed axes are then rotated by an angle, α, around the original z axis. The new coordinates in the primed frame are shown in dashed blue lines in Figure 2.10. This rotation is followed by a second rotation about the primed y-axis through an angle, β, giving the

double primed frame shown in red with circular dots in Figure 2.10. Finally, a rotation of γ is performed around the z-axis in the double primed frame to give the triple primed frame shown in green with square dots. Depending on the situation, multiple stages of these transformations may need to be performed. For example, one may want to rotate from the principle axis frame of an interaction to a frame of reference fixed on an MAS rotor, and then transform the rotor fixed frame to the lab frame[15].

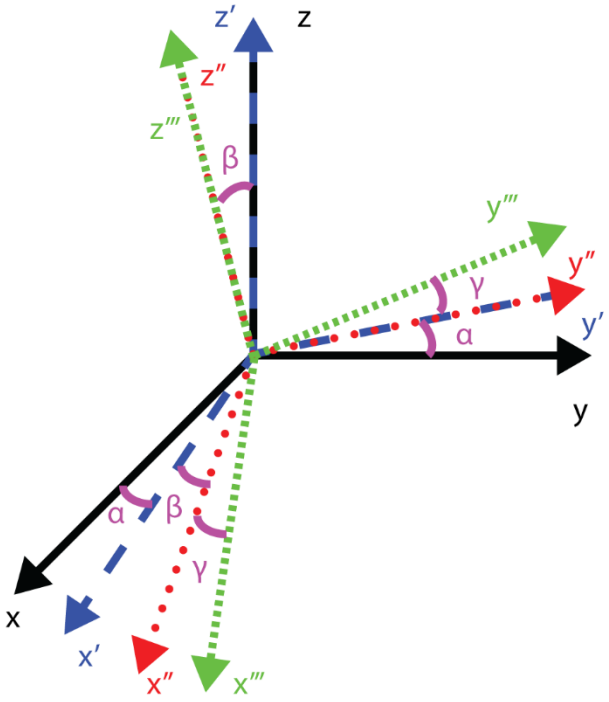

Figure 2.10: The z-y-z Euler angle convention. The original reference frame is pictured in black. The coordinate axes following each successive rotation has had an additional prime added to their name.

Traditional simulation techniques involve simulating the spectrum using a large number of powder angles and averaging these separate spectra together to obtain an approximation of the powder pattern. The simulation of hundreds or thousands of powder patterns is what leads to such long simulation times. This is a particular problem in electron paramagnetic resonance (EPR) spectra due to their spectral width. Analytically averaging these simulated spectra over at

least one of the powder angles, however, can drastically reduce simulation time. This is described further in Chapter 6.

References

(1) Saliba, E. P.; Sesti, E. L.; Alaniva, N.; Barnes, A. B. Pulsed Electron Decoupling and Strategies for Time Domain Dynamic Nuclear Polarization with Magic Angle Spinning. *J. Phys. Chem. Lett.* **2018**, *9*, 5539–5547.

(2) Hayes, S.; Van Wüllen, L.; Eckert, H.; Even, W. R.; Crocker, R. W.; Zhang, Z. Solid-State NMR Strategies for the Structural Investigation of Carbon-Based Anode Materials. *Chem. Mater.* **1997**, *9* (4), 901–911.

(3) Yang, H.; Staveness, D.; Ryckbosch, S. M.; Axtman, A. D.; Loy, B. A.; Barnes, A. B.; Pande, V. S.; Schaefer, J.; Wender, P. A.; Cegelski, L. REDOR NMR Reveals Multiple Conformers for a Protein Kinase c Ligand in a Membrane Environment. *ACS Cent. Sci.* **2018**, *4* (1), 89–96.

(4) Rossini, A. J.; Widdifield, C. M.; Zagdoun, A.; Lelli, M.; Schwarzwälder, M.; Copéret, C.; Lesage, A.; Emsley, L. Dynamic Nuclear Polarization Enhanced NMR Spectroscopy for Pharmaceutical Formulations. *J. Am. Chem. Soc.* **2014**, *136* (6), 2324–2334.

(5) Mak-Jurkauskas, M. L.; Bajaj, V. S.; Hornstein, M. K.; Belenky, M.; Griffin, R. G.; Herzfeld, J. Energy Transformations Early in the Bacteriorhodopsin Photocycle Revealed by DNP-Enhanced Solid-State NMR. *Proc. Natl. Acad. Sci.* **2008**, *105* (3), 883–888.

(6) Kaplan, M.; Narasimhan, S.; de Heus, C.; Mance, D.; van Doorn, S.; Houben, K.; Popov-Čeleketić, D.; Damman, R.; Katrukha, E. A.; Jain, P.; et al. EGFR Dynamics Change during Activation in Native Membranes as Revealed by NMR. *Cell* **2016**, *167* (5), 1241-

1251.e11.

(7) Baker, L. A.; Sinnige, T.; Schellenberger, P.; de Keyzer, J.; Siebert, C. A.; Driessen, A. J. M.; Baldus, M.; Grünewald, K. Combined 1H-Detected Solid-State NMR Spectroscopy and Electron Cryotomography to Study Membrane Proteins across Resolutions in Native Environments. *Structure* **2018**, *26* (1), 161-170.e3.

(8) Traficante, D. D. Introduction to Transmission Lines Basic Principles and Applications of Quarter Wavelength Cables and Impedance Matching. *Concepts Magn. Reson.* **1993**, *5* (1), 57–86.

(9) Traficante, D. D. Imepedance: What It Is, and Why It Must Be Matched. *Concepts Magn. Reson.* **1989**, *1*, 73–92.

(10) Barnes, A. B.; Mak-Jurkauskas, M. L.; Matsuki, Y.; Bajaj, V. S.; van der Wel, P. C. A.; DeRocher, R.; Bryant, J.; Sirigiri, J. R.; Temkin, R. J.; Lugtenburg, J.; et al. Cryogenic Sample Exchange NMR Probe for Magic Angle Spinning Dynamic Nuclear Polarization. *J. Magn. Reson.* **2009**, *198* (2), 261–270.

(11) Carver, T. R.; Slichter, C. P. Polarization of Nuclear Spins in Metals. *Phys. Rev.* **1953**, *92* (1), 212–213.

(12) Kubicki, D. J.; Rossini, A. J.; Purea, A.; Zagdoun, A.; Ouari, O.; Tordo, P.; Engelke, F.; Lesage, A.; Emsley, L. Amplifying Dynamic Nuclear Polarization of Frozen Solutions by Incorporating Dielectric Particles. *J. Am. Chem. Soc.* **2014**, *136* (44), 15711–15718.

(13) Lilly Thankamony, A. S.; Wittmann, J. J.; Kaushik, M.; Corzilius, B. Dynamic Nuclear Polarization for Sensitivity Enhancement in Modern Solid-State NMR. *Prog. Nucl. Magn. Reson. Spectrosc.* **2017**, *102–103*, 120–195.

(14) Herzfeld, J.; Berger, A. E. Sideband Intensities in NMR Spectra of Samples Spinning at

the Magic Angle. *J. Chem. Phys.* **1980**.

(15) Mueller, L. J. Tensors and Rotations in NMR. *Concepts Magn. Reson. Part A* **2011**, *38A*, 221–235.

(16) Levitt, M. H. *Spin Dynamics*, 2nd ed.; John Wiley & Sons Ltd.: West Sussex, 2008.

(17) Gullion, T.; Schaefer, J. Rotational-Echo Double-Resonance NMR. *J. Magn. Reson.* **1989**, No. 81, 196–200.

(18) Saliba, E. P.; Sesti, E. L.; Scott, F. J.; Albert, B. J.; Choi, E. J.; Alaniva, N.; Gao, C.; Barnes, A. B. Electron Decoupling with Dynamic Nuclear Polarization in Rotating Solids. *J. Am. Chem. Soc.* **2017**, *139* (18), 6310–6313.

(19) Leavesley, A.; Wilson, C. B.; Sherwin, M.; Han, S. Effect of Water/Glycerol Polymorphism on Dynamic Nuclear Polarization. *Phys. Chem. Chem. Phys.* **2018**, *20* (15), 9897–9903.

(20) Sesti, E. L.; Saliba, E. P.; Alaniva, N.; Barnes, A. B. Electron Decoupling with Cross Polarization and Dynamic Nuclear Polarization below 6 K. *J. Magn. Reson.* **2018**, *295*, 1–5.

(21) Barnes, A. B.; Nanni, E. A.; Herzfeld, J.; Griffin, R. G.; Temkin, R. J. A 250 GHz Gyrotron With a 3 GHz Tuning Bandwidth for Dynamic Nuclear Polarization. **2013**, No. 221, 147–153.

(22) Becerra, L. R.; Gerfen, G. J.; Temkin, R. J.; Singel, D. J.; Griffin, R. G. Dynamic Nuclear Polarization with a Cyclotron Resonance Maser at 5 T. *Phys. Rev. Lett.* **1993**, *71* (21), 3561–3564.

(23) Can, T. V.; Weber, R. T.; Walish, J. J.; Swager, T. M.; Griffin, R. G. Frequency-Swept Integrated Solid Effect. *Angew. Chemie - Int. Ed.* **2017**, *56* (24), 6744–6748.

(24) Can, T. V.; Caporini, M. a.; Mentink-Vigier, F.; Corzilius, B.; Walish, J. J.; Rosay, M.; Maas, W. E.; Baldus, M.; Vega, S.; Swager, T. M.; et al. Overhauser Effects in Insulating Solids. *J. Chem. Phys.* **2014**, *141* (6), 064202.

(25) Maly, T.; Debelouchina, G. T.; Bajaj, V. S.; Hu, K.-N.; Joo, C.-G.; Mak–Jurkauskas, M. L.; Sirigiri, J. R.; van der Wel, P. C. A.; Herzfeld, J.; Temkin, R. J.; et al. Dynamic Nuclear Polarization at High Magnetic Fields. *J. Chem. Phys.* **2008**, *128* (5), 052211.

(26) Henstra, A.; Dirksen, P.; Wenckebach, W. T. Enhanced Dynamic Nuclear Polarization by the Integrated Solid Effect. *Phys. Lett. A* **1988**, *134* (2), 134–136.

(27) Henstra, A.; Dirksen, P.; Schmidt, J.; Wenckebach, W. T. Nuclear Spin Orientation via Electron Spin Locking (NOVEL). *J. Magn. Reson.* **1988**, *77*, 389–393.

(28) Jain, S. K.; Mathies, G.; Griffin, R. G. Off-Resonance NOVEL. *J. Chem. Phys.* **2017**, *147* (16).

(29) Kupce, Ē.; Freeman, R. Stretched Adiabatic Pulses for Broadband Spin Inversion. *J. Magn. Reson. Ser. A* **1995**, *117* (2), 246–256.

(30) Hoff, D. E. M.; Albert, B. J.; Saliba, E. P.; Scott, F. J.; Choi, E. J.; Mardini, M.; Barnes, A. B. Frequency Swept Microwaves for Hyperfine Decoupling and Time Domain Dynamic Nuclear Polarization. *Solid State Nucl. Magn. Reson.* **2015**, *72*.

(31) Albert, B. J.; Pahng, S. H.; Alaniva, N.; Sesti, E. L.; Rand, P. W.; Saliba, E. P.; Scott, F. J.; Choi, E. J.; Barnes, A. B. Instrumentation for Cryogenic Magic Angle Spinning Dynamic Nuclear Polarization Using 90 L of Liquid Nitrogen per Day. *J. Magn. Reson.* **2017**, *283*, 71–78.

(32) Scott, F. J.; Saliba, E. P.; Albert, B. J.; Alaniva, N.; Sesti, E. L.; Gao, C.; Golota, N. C.; Choi, E. J.; Jagtap, A. P.; Wittmann, J. J.; et al. Frequency-Agile Gyrotron for Electron

Decoupling and Pulsed Dynamic Nuclear Polarization. *J. Magn. Reson.* **2018**, *289*.

(33) Scott, F. J.; Alaniva, N.; Golota, N. C.; Sesti, E. L.; Saliba, E. P.; Price, L. E.; Albert, B. J.; Chen, P.; Connor, R. D. O.; Barnes, A. B. A Versatile Custom Cryostat for Dynamic Nuclear Polarization Supports Multiple Cryogenic Magic Angle Spinning Transmission Line Probes. *J. Magn. Reson.* **2018**, *297*, 23–32.

(34) Nusinovich, G. S. *Introduction to the Physics of Gyrotrons*; Johns Hopkins University Press, 2004.

(35) Albert, B. J.; Pahng, S. H.; Alaniva, N.; Sesti, E. L.; Rand, P. W.; Saliba, E. P.; Scott, F. J.; Choi, E. J.; Barnes, A. B. Instrumentation for Cryogenic Magic Angle Spinning Dynamic Nuclear Polarization Using 90 L of Liquid Nitrogen per Day. *J. Magn. Reson.* **2017**, *283*.

(36) Hu, K.-N.; Yu, H.; Swager, T. M.; Griffin, R. G. Dynamic Nuclear Polarization with Biradicals. *J. Am. Chem. Soc.* **2004**, *126* (35), 10844–10845.

(37) Griffin, R. G. Dynamic Nuclear Polarization at 9T Using a Novel 250 Gyrotron Microwave Source. *J. Magn. Reson.* **2011**, *213* (2), 410–412.

(38) Albert, B. J.; Gao, C.; Sesti, E. L.; Saliba, E. P.; Alaniva, N.; Scott, F. J.; Sigurdsson, S. T.; Barnes, A. B. Dynamic Nuclear Polarization Nuclear Magnetic Resonance in Human Cells Using Fluorescent Polarizing Agents. *Biochemistry* **2018**, *57* (31), 4741–4746.

(39) Alaniva, N.; Saliba, E. P. .; Sesti, E. L.; Judge, P. T.; Barnes, A. B. Electron Decoupling with Chirped Microwave Pulses for Rapid Signal Acquisition and Electron Saturation Recovery. *Angew. Chemie* **2019**.

(40) Sesti, E. L.; Alaniva, N.; Rand, P. W.; Choi, E. J.; Albert, B. J.; Saliba, E. P.; Scott, F. J.; Barnes, A. B. Magic Angle Spinning NMR below 6 K with a Computational Fluid

Dynamics Analysis of Fluid Flow and Temperature Gradients. *J. Magn. Reson.* **2018**, *286*, 1–9.

(41) Massiot, D.; Fayon, F.; Capron, M.; King, I.; Le Calvé, S.; Alonso, B.; Durand, J. O.; Bujoli, B.; Gan, Z.; Hoatson, G. Modelling One- and Two-Dimensional Solid-State NMR Spectra. *Magn. Reson. Chem.* **2002**, *40* (1), 70–76.

(42) Nocedal, J.; Wright, S. J. *Numerical Optimization*; Springer, 1999.

Chapter 3: Pulsed Electron Decoupling and Strategies for Time Domain Dynamic Nuclear Polarization with Magic Angle Spinning

Forward

This chapter was adapted from the paper "Pulsed Electron Decoupling and Strategies for Time Domain Dynamic Nuclear Polarization with Magic Angle Spinning" by Edward P. Saliba, Erika L. Sesti, Nicholas Alaniva, and Alexander B. Barnes. This paper is a review article describing work done on electron decoupling and time domain DNP. This is an unofficial adaptation of an article that appeared in an ACS publication. ACS has not endorsed the content of this adaptation or the context of its use. This chapter provides the background behind why the electron decoupling experiments and powder averaging techniques for fast magnetic resonance simulations presented in the subsequent chapters is important. The implementation of direct transfer DNP mechanisms with electron decoupling is one promising technique to produce DNP enhancements at room temperature or higher while avoiding detrimental paramagnetic broadening and short homogeneous relaxation times that could be present if a radical is directly chemically connected to the sample molecule. This paper received the Editor's Choice award from the Journal of Physical Chemistry Letters. Citation: Saliba, E. P.; Sesti, E. L.; Alaniva, N.; Barnes, A. B. Pulsed Electron Decoupling and Strategies for Time Domain Dynamic Nuclear Polarization with Magic Angle Spinning. *J. Phys. Chem. Lett.* 2018, *9*, 5539–5547.

Abstract

Magic angle spinning (MAS) dynamic nuclear polarization (DNP) is widely used to increase nuclear magnetic resonance (NMR) signal intensity. Frequency-chirped microwaves yield superior control of electron spins, and are expected to play a central role in the development of DNP MAS experiments. Time domain electron control with MAS has considerable promise to improve DNP performance at higher fields and temperatures. Pulsed electron decoupling has been demonstrated using frequency-chirped microwaves to improve MAS DNP experiments by partially attenuating detrimental hyperfine interactions. The continued development of pulsed electron decoupling will enable a new suite of MAS DNP experiments which transfer polarization directly to observed spins. Time domain DNP transfers to nuclear spins in conjunction with pulsed electron decoupling is described as a viable avenue toward DNP-enhanced, high-resolution NMR spectroscopy over a range of temperatures from <6K to 320 K.

3.1 Introduction

Nuclear magnetic resonance (NMR) spectroscopy is a powerful tool that can provide details about the molecular structure and dynamics of myriad systems[1–5]. NMR can routinely yield multiple distinguishable signals with site-specific resolution[6]. Not only does the chemical shift provide information about the electronic environment, but spatial and through-bond magnetic interactions provide distance and connectivity information, which determine constraints on molecular structure[7–12]. Solid-state NMR (ssNMR) is often employed in conjunction with magic angle spinning (MAS) to extend coherence lifetimes and improve spectral resolution[13–16].

While NMR has advantages over other forms of spectroscopy, it suffers from an inherent lack of sensitivity due to the small Boltzmann polarization of nuclear spins, given by Equation (3.1):

$$P = -\tanh\left(\frac{h\nu_0}{2k_BT}\right) \tag{3.1}$$

where h is Planck's constant, k_B is Boltzmann's constant, ν_0 is the Larmor frequency of the spin, and T is the temperature in Kelvin[17–19]. The small spin polarization results in a weak electromotive force induced in the coil of the probe, and a correspondingly poor signal-to-noise ratio (S/N) in the NMR spectrum[20–22]. Common strategies to increase NMR S/N involve performing experiments at high magnetic fields (7-25 Tesla), using large samples, and averaging signals for as long as months[23].

3.2 Dynamic Nuclear Polarization

Dynamic nuclear polarization (DNP) can increase NMR S/N by orders of magnitude, greatly shortening signal-averaging times, and expanding the range of systems that can be studied with NMR[24]. In MAS DNP, samples are typically doped with an exogenous stable radical (known as a polarizing agent) and, upon CW irradiation with an appropriate microwave frequency, the large electron spin polarization is transferred to nuclear spins through hyperfine interactions. Most applications of DNP also rely on proton dipolar couplings to spread the enhanced polarization throughout a proton network, resulting in bulk nuclear hyperpolarization[25].

The gyromagnetic ratio of a bare electron ($g = 2.0023$) is 658-times larger than that of a proton, leading to higher spin polarization, and also strong hyperfine couplings. Dipolar hyperfine

couplings are typically leveraged in DNP for polarization transfer, but can also lead to detrimental paramagnetic relaxation effects of nuclear spins in the vicinity of the polarizing agent. An example of the exceptional NMR sensitivity achievable with DNP is shown in Figure 3.1, which compares cross polarization (CP) MAS ^{13}C -NMR spectra recorded with and without microwave irradiation. DNP increases the NMR signal intensity by a factor of 328 using microwaves from a high-power, 198 GHz gyrotron. MAS DNP is commonly performed below 120 K, but improved technology and methodology will result in better DNP performance at room temperature.

Much of the success and popularity of MAS DNP is derived from the microwave and probe technology development at M.I.T. by Griffin, Temkin, and co-workers[6,26–31]. Continuous wave (CW) gyrotron oscillators and cryogenic MAS probes provide access to sufficient microwave powers and sample temperatures to transform DNP into to a widely applicable magnetic resonance technique. Improvements in microwave technology and cryogenics are also expected to play a primary role in future DNP development. Coherent, frequency-agile microwave sources will permit time domain DNP transfers, and access to sample temperatures below 6 K will be achieved by employing helium cryogens. This chapter reviews recent developments in time domain microwave methods and cryogenics employed in MAS DNP and electron decoupling. Progress towards time domain DNP with magic angle spinning for applications between 4.2 and 320 K is also discussed.

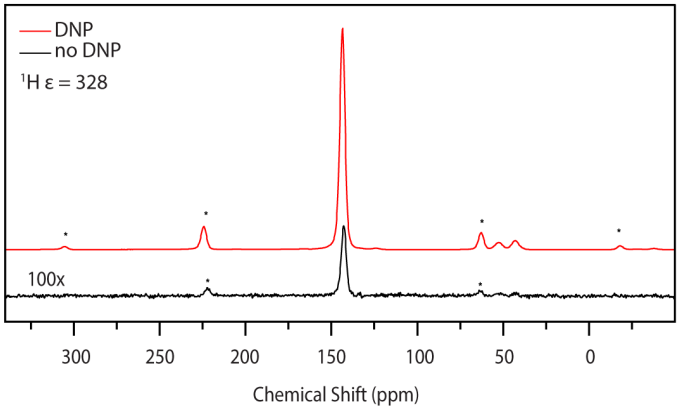

Figure 3.1: a) CP MAS enhancement spectra of 1 M U-^{13}C urea with 20 mM AMUPol at 81 K at 6 kHz. The ^{1}H enhancement was 328. The black curve is 100 × the signal obtained with no microwaves. The red curve denotes measurements taken with microwaves present. Figure reproduced with modifications with permission of the Journal of Magnetic Resonance[32].

The spectra shown in Figure 3.1 were recorded with a sample temperature of 81 K, which is typical in MAS DNP experiments. Cryogenic temperatures are required in MAS DNP experiments (with notable exceptions in model systems[33–36]) due to electronic spin relaxation at room temperature interfering with polarization transfer, and nuclear relaxation preventing the build-up of bulk nuclear spin polarization via proton spin diffusion.

The major disadvantage of cryogenically freezing biological samples is that the cryogenically trapped molecular state is not necessarily the same conformation that exists at physiological temperature. This is because the freezing time ranges from hundreds of microseconds to hours. Molecules can change structure to occupy altered minima in the free energy landscape throughout the freezing process. For example, crystallography shows pronounced differences of protein structures determined at cryogenic and room temperature[37]. Hydrogen bonding networks are particularly prone to rearrangement upon cryogenic freezing, and detailed structural

measurements on molecular conformations that differ from the relevant ones are less meaningful. In addition, cryogenic DNP severely limits measurements of molecular dynamics.

Magnetic resonance is superbly suited to experimentally determine the molecular dynamics that play a fundamental role in molecular function. Nuclear and electronic interactions yield rich information on motion ranging from nanoseconds to seconds. However, low thermal energy at cryogenic temperatures results in a mostly static snapshot of molecules, so current cryogenic DNP NMR methods cannot be used to study extensive molecular dynamics. DNP NMR experiments near room temperature will allow for the determination of molecular dynamics. Molecular motion near room temperature can also result in exquisite spectral resolution in NMR.

Although MAS NMR spectra of many solids exhibit excellent resolution near room temperature due to dynamic averaging of multiple conformations with different chemical shifts, they often smear into broad, indistinguishable lineshapes at cryogenic temperatures[6]. This is true even for cryoprotected samples. Notable exceptions include model systems with cryogenic MAS, in which more homogenous conformational ensembles result in narrow resonances, even after freeze-trapping[6,22,38–40]. Performing DNP near room temperature will result in well-resolved spectra of a much wider range of samples, and also reduce the cost of DNP spectrometers. Refrigerators, liquid nitrogen dewars, cryostats, and associated equipment are expensive and require valuable laboratory space. Non-cryogenic DNP spectrometers will result in broader dissemination of high-sensitivity solid state NMR technology.

Time domain DNP performed directly to nuclei of interest with subsequent pulsed electron decoupling is a promising route toward broadly applicable room temperature (RT) MAS DNP. For instance, the relatively slow proton spin diffusion which partially prevents RT DNP is not required. The polarization rate is instead dominated by the hyperfine interaction, radio frequency (RF), and microwave (MW) fields. Repetition rates in such "direct transfer" DNP experiments are only limited by the longitudinal electronic relaxation (T_{1S}) rather than much longer nuclear $T_{1I,DNP}$. Such experiments have already been applied in static NMR, resulting in DNP enhancements above 200 at room temperature[41–43]. Additionally, the resulting short polarization times allow for a very low duty cycle of the microwave source, preventing excessive heating.

Although delays between transients are reduced by eliminating the requirement for spin diffusion, electrons must be in direct dipolar contact with the nuclear spin of interest. This can lead to dramatic paramagnetic effects such as large hyperfine shifts and hyperfine broadening of the nuclear resonances[44]. Electron decoupling has recently been shown to successfully attenuate these detrimental effects by employing pulsed electron decoupling with frequency-chirped microwave irradiation[45]. Although pulsed electron decoupling has been demonstrated in conjunction with MAS, this has yet to be accomplished with time domain DNP. Challenges include generating sufficiently intense microwave fields within MAS rotors and shaping microwave pulses in the time domain.

Three promising time domain DNP techniques that have been described in the literature are the integrated solid effect (ISE)[42,46], off-resonance nuclear orientation via electron spin locking

(NOVEL)[41], and electron-nuclear cross-polarization (eNCP)[47,48]. Importantly, all three of these time-domain DNP transfers can be implemented with chirped frequency microwave irradiation, rather than square, hard pulses. Such frequency-swept strategies are highly robust to microwave field inhomogeneity. Note that pulsed DNP strategies, which require very homogenous microwave fields, will be restricted to small sample volumes, and perhaps negate increases in S/N afforded by DNP.

3.2.1 The Integrated Solid Effect

Wenckebach and coworkers originally implemented the ISE with a magnetic field sweep to improve solid effect DNP efficiency on samples with poorly resolved solid effect matching condition profiles[46]. Later, Griffin and coworkers implemented the ISE with a microwave frequency sweep[42]. However, both of these demonstrations were at field strengths < 7 T, and not performed with MAS.

The matching condition for the solid effect[43] is given by Equation (3.2):

$$\nu_S^{eff} = \pm\nu_I \tag{3.2}$$

where ν_I is the Larmor frequency of the nucleus of interest. ν_S^{eff} is given by Equation (3.3):

$$\nu_S^{eff} = \sqrt{\left(\nu_S - \nu_{mw}\right)^2 + \nu_{1S}^2} \tag{3.3}$$

where ν_S is the Larmor frequency of the electron, ν_{mw} is the microwave frequency irradiating the sample, and ν_{1S} is the Rabi frequency (γB_1) of the electrons[43]. Figure 3.2 demonstrates the

energy levels involved in the traditional solid effect[29], in which $\nu_S - \nu_{mw} \gg \nu_{1S}$. In this case, the effective field is essentially equal to the microwave frequency offset from the electron resonant frequency. The green circles represent the populations of the states shown at thermal equilibrium (not drawn to scale). The double headed arrows connect the states whose populations are equalized under microwave irradiation at the frequencies shown. The lowest energy level of the system is taken to be the zero of the energy scale.

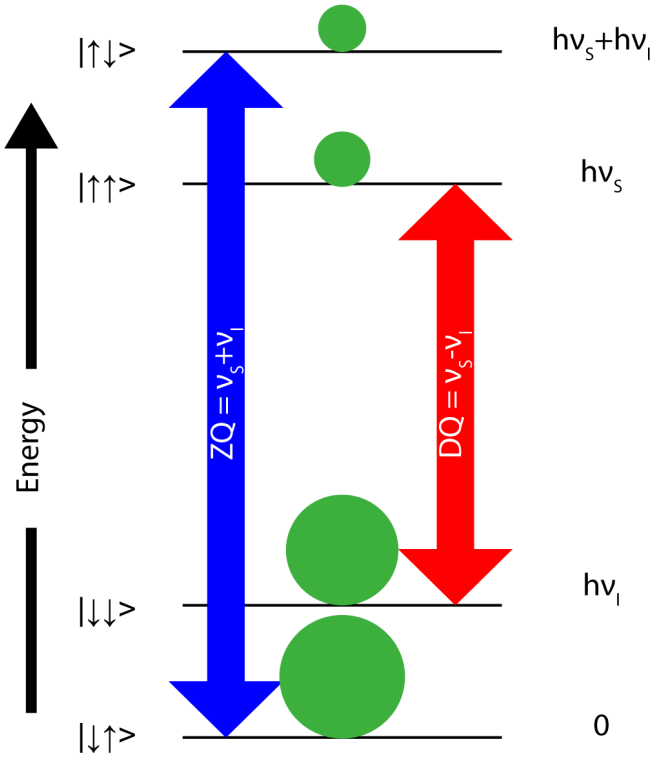

Figure 3.2: Microwaves drive zero quantum or double quantum forbidden transitions corresponding to the transitions shown. This representation of the solid effect assumes that the nucleus has a positive gyromagnetic ratio. The ket vectors are labeled as $|m_s m_I\rangle$.

Figure 3.3a provides an example of a solid effect enhancement profile that is not fully resolved (black), with the electron decoupling profile superimposed (green) to provide a guide to the position of the electron paramagnetic resonance (EPR) lineshape. When the solid effect conditions are not adequately resolved, the double-quantum (DQ) and zero-quantum (ZQ) matching conditions[50] given in Equation 2.2 can be simultaneously fulfilled. In this case, the polarization rates of the DQ and ZQ conditions subtract, leading to poor enhancement in the overlapping region. This is explicitly stated in Equation 2.4, where $\frac{dP}{dt}$ is the total rate of polarization, $\frac{dP_{DQ}}{dt}$ is the rate of polarization due to the DQ solid effect, and $\frac{dP_{ZQ}}{dt}$ is the rate of polarization due to the ZQ solid effect:

$$\left|\frac{dP}{dt}\right| = \left|\frac{dP_{DQ}}{dt} - \frac{dP_{ZQ}}{dt}\right| \tag{3.4}$$

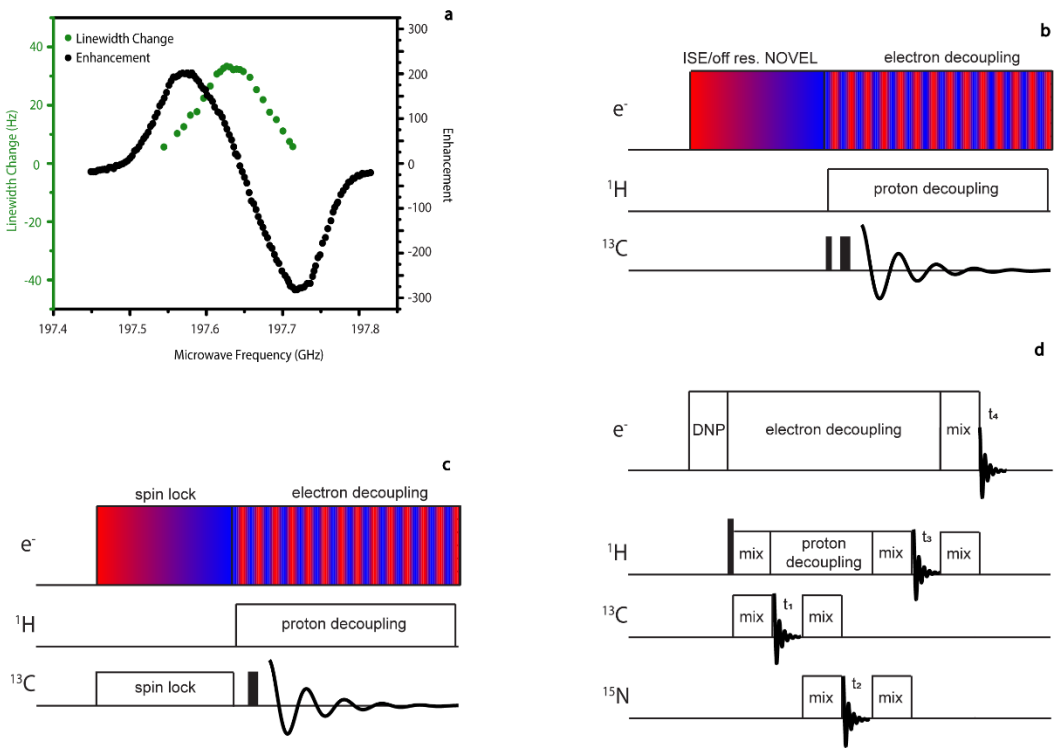

Figure 3.3: a.) A mildly unresolved solid effect enhancement profile for protons in 4 M [U-^{13}C,^{15}N] urea with 40 mM of the Finland Trityl radical (black). This figure was reproduced with modification with permission from the Journal of Magnetic Resonance[53]. Superimposed is the center frequency dependence of electron decoupling to demonstrate the location of the EPR spectrum of the radical (green). This figure was reproduced with modification with permission from the Journal of the American Chemical Society[45]. b.) Possible frequency swept ISE/off-resonance NOVEL pulse sequence. c.) Possible eNCP pulse sequence. Color gradients in Figures 3.3b and 3. 3c indicate frequency chirped microwaves. d.) Proposed electron detected multiple dimensional pulse sequence.

In the frequency-swept ISE, the microwave frequency initially fulfills either the DQ or ZQ solid effect conditions, and is swept through the electron resonance condition to the other solid effect condition. This is shown in Figure 3.3b, which also includes pulsed electron decoupling during the echo detection of the NMR signal. During the ISE sweep, electron spins are adiabatically inverted, effectively reversing the direction of the ZQ, or DQ contribution to the polarization rate (depending on the direction of the sweep). The rate of polarization is then given by Equation (3.5):

$$\left|\frac{dP}{dt}\right| = \left|\frac{dP_{DQ}}{dt} + \frac{dP_{ZQ}}{dt}\right| \tag{3.5}$$

This improvement in the polarization rate derived from coherent control of electron spins has been used to obtain ^{1}H enhancements on static samples at 0.35 T [42].

3.2.2 Off Resonance NOVEL

Closely related to the ISE is off-resonance NOVEL[43], which relaxes the largely prohibitive matching condition for on-resonance NOVEL. NOVEL requires matching the electron Rabi frequency with the nuclear Larmor frequency. Even for nuclei with relatively small gyromagnetic ratios at moderate magnetic fields, such as ^{15}N at a field strength of 7 Tesla, an electron γB_1 of 30 MHz is required for on-resonance NOVEL. NOVEL to protons at 21 T requires a 900 MHz electron Rabi frequency, which corresponds to a currently inaccessible power of >10 MW [49]. In off-resonance NOVEL, the electron γB_1 is made as large as possible, and the offset of the microwave frequency from the electron resonance frequency is used to reach the matching condition given in Equation (3.2). Typically, the NOVEL experiment begins with a pulse on the electron spins to tilt their magnetization into the transverse plane, followed by a spin lock. Alternatively, a frequency-chirp of the irradiating microwaves can be employed in an adiabatic half passage to generate transverse magnetization. It should be noted that the easing of the matching condition for off-resonance NOVEL over on-resonance NOVEL comes at the expense of a scaling of the maximum enhancement obtainable as derived previously in the literature[43]. The expression for the corresponding scaling factor (κ_{NOVEL}) is given in Equation (3.6):

$$\kappa_{NOVEL} = \left(\frac{\nu_S - \nu_{mw}}{\sqrt{(\nu_S - \nu_{mw})^2 + \nu_{1S}^2}} \right)^3 \mp \left(\frac{\nu_S - \nu_{mw}}{\sqrt{(\nu_S - \nu_{mw})^2 + \nu_{1S}^2}} \right)^2 \pm 1 \tag{3.6}$$

The pulse sequence for a frequency-swept, off-resonance NOVEL experiment is essentially the same as the ISE shown in Figure 3.3b, but with a larger γB_1.

3.2.3 Electron-Nuclear Cross Polarization

eNCP (Figure 3.3c) is another promising time-domain DNP experiment[47,48], and could be implemented with readily available frequency-agile gyrotron microwave sources. Large hyperfine couplings present in a direct transfer eNCP experiment result in differing effective fields between the $+\frac{1}{2}$ and $-\frac{1}{2}$ spin states of the nuclei and electrons The matching condition for eNCP is given by Equation 2.6, where $\nu_{S\alpha}^{eff}$ and $\nu_{S\beta}^{eff}$ are the effective fields of the $+\frac{1}{2}$ and $-\frac{1}{2}$ electrons, respectively, and $\nu_{I\alpha}^{eff}$ and $\nu_{I\beta}^{eff}$ are the effective fields of the $+\frac{1}{2}$ and $-\frac{1}{2}$ nuclei, respectively. The expressions for calculating these effective fields have been shown previously in the literature and appear in Equation (3.7)[47,48].

$$\left(\nu_{S\alpha}^{eff} + \nu_{S\beta}^{eff}\right) = \pm\left(\nu_{I\alpha}^{eff} + \nu_{I\beta}^{eff}\right) \tag{3.7}$$

3.3 Electron Detected Magnetic Resonance

In magnetic resonance experiments, large gyromagnetic ratios result in more sensitive signal detection. The S/N in the experiment can therefore be optimized further by detecting the EPR signal of the electrons rather than the NMR signal of the nuclei. Electron nuclear double

resonance (ENDOR)[51] and electron spin echo envelope modulation (ESEEM)[52] are two techniques currently used to monitor NMR transitions through EPR detection. Integration of pulsed EPR and NMR with MAS will allow for electron detected, high-resolution multiple dimensional NMR experiments to be performed. Figure 3.3d provides an example of such a sequence. Polarization could first be transferred from the electrons to the protons which are directly coupled with time domain DNP methods. This initial transfer could be followed by a series of mixing and evolution periods on various nuclear spins detected in indirect dimensions, as is commonly employed in high-resolution multi-dimensional NMR. A final mixing period could transfer magnetization back to the electrons for detection in the direct dimension. Electron decoupling would be necessary in such experiments to maintain long nuclear spin-spin relaxation times as well as resolution in the indirect dimensions.

The time domain DNP experiments listed above will be used in conjunction with direct transfer DNP, in which the electron spin polarization is transferred directly to the sample nuclei. While this technique saves experimental time by removing slow nuclear spin diffusion, observed nuclei must be close to the paramagnetic radical electrons, which can have detrimental effects on the resolution of the resulting spectrum. Electron decoupling (eDEC) can be employed to partially average out hyperfine interactions and will be a crucial aspect of direct-transfer DNP.

3.4 Electron Decoupling

Electron decoupling has been successfully implemented in MAS NMR experiments[45]. The pulse sequence for a ^{13}C-Hahn echo detected eDEC DNP MAS experiment is shown in Figure 3.4a.

During the polarization period the microwave frequency is maintained at a constant value for DNP solid effect enhancement. The microwave frequency is then chirped over the electron resonance condition during the NMR signal detection.

Figures 3.4b and 3.4c display a comparison of spectra taken with eDEC (red) and without eDEC (black) of urea frozen in a glassy matrix with trityl using DNP polarization times of 0.5 and 7 seconds, respectively. In both cases, the spectra obtained with electron decoupling show narrower resonances, as well as increased intensity over those taken with no eDEC. The spectra obtained using a polarization time of 0.5 seconds have larger linewidths than those using a polarization time of 7 seconds. This is expected, as the nuclei that become polarized at 0.5 seconds of polarization time are closer to the radical electron than the polarized nuclear spins in the 7 second polarization time experiment. The effect of electron decoupling is greater at shorter polarization times because strongly coupled nuclei make up a larger portion of the signal in that regime, and so the signal is not washed out by more weakly coupled ones that are already not as broadened.

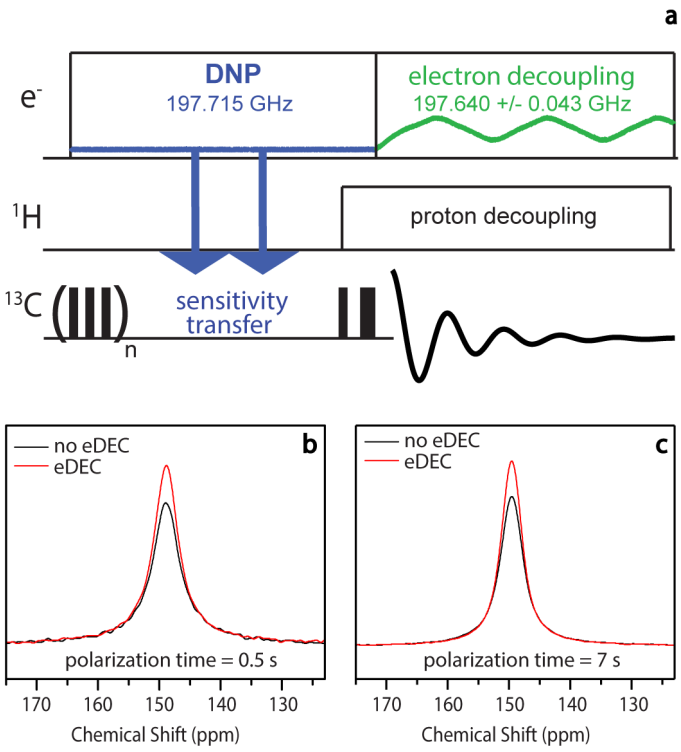

Figure 3.4: a) The ^{13}C Hahn-Echo pulse sequence used to demonstrate pulsed electron decoupling. b) Pulsed electron decoupling performed with a polarization time of 0.5 seconds. The linewidth is narrowed from 419 Hz to 371 Hz with pulsed electron decoupling: a narrowing of 48 Hz. c) Pulsed electron decoupling performed with a polarization time of 7 seconds. The linewidth is narrowed from 336 Hz to 309 Hz with pulsed electron decoupling: a narrowing of 27 Hz. Black spectra represent the ^{13}C signal obtained with no electron decoupling, while red spectra represent those obtained with pulsed electron decoupling. The sample is 4 M (U-^{13}C, ^{15}N) urea and 40 mM Trityl (Finland radical) in d-8 glycerol/D_2O/H_2O (60/30/10 by volume) at a sample volume of 30 µL in a 3.2 mm zirconia rotor. The experiments were conducted at 90 K and at a sample spinning frequency of 4 kHz. Figure reproduced with modifications by permission of the Journal of the American Chemical Society[45].

3.5 Microwaves from a Frequency Agile Gyrotron

The success of these pulsed electron decoupling experiments is due, in large part, to the frequency agility of the microwave source. Creating microwave chirps requires rapid frequency agility while maintaining power output, as well as the ability to integrate frequency chirped

microwave irradiation into the pulse sequence of the NMR spectrometer with integrated EPR excitation capability.

The implementation of frequency-agile gyrotrons has been crucial to realizing pulsed electron decoupling with MAS. A high-power, frequency-agile microwave source is required to generate the requisite electron γB_1 fields at the desired frequencies and to overcome extensive inhomogeneity in the microwave field irradiating the sample. The gyrotron generates microwaves by accelerating electrons into a mildly relativistic energy regime through a large magnetic field, which causes them to gyrate[54]. Electrons then deposit energy in the form of microwave power into a cylindrical cavity. In the gyrotron depicted in Figure 3.5a,b, the rotating $TE_{5,2}$ transverse electromagnetic mode was selected in the interaction cavity due to a wide frequency excitation profile which enables the generation of chirped microwave pulses. A helically-cut Vlasov launcher and mode converter transforms the microwave power distributed in the high-order mode, into a Gaussian profile that couples efficiently to the HE_{11} mode supported in the over-moded waveguide (Figure 3.5a)[49,55].

Frequency agility is achieved by quickly changing the accelerating voltage on the gyrotron anode[53]. An arbitrary waveform generator in the NMR spectrometer generates voltage sweeps which are amplified by a low capacitance amplifier, allowing for frequency chirped microwave irradiation to be readily implemented into the NMR pulse sequences. The amplifier output is then connected to the accelerating anode of the gyrotron (yellow cable in Figure 3.5b). Figure 3.5c shows a decrease in the output frequency when the accelerating voltage is increased[53,54].

The gyrotron accelerating voltage can also be used for microwave gating. Microwave irradiation is rapidly terminated (over about 10 microseconds) by setting the potential to a voltage with a cyclotron frequency well outside the resonant condition of the cavity. Microwave gating via voltage control can generate rotor-synchronized microwave power, as shown in Figure 3.5d. This technique could also be used to duty cycle the microwave irradiation and minimize sample heating.

Approximately 7.1% of microwave power is dissipated as heat in a frozen glycerol-water sample[49]. With an input microwave power of 5 W, the 0.4 W of power deposited in the sample is easily dissipated by the large cooling capacity of the cryogenic fluid supplied by the MAS system[56]. At room temperature dielectric heating of aqueous samples will dramatically increase due to a higher dielectric loss tangent of liquids compared to frozen solids. Therefore the ability to keep the microwave irradiation at a low duty cycle will be crucial to prevent excessive heating of aqueous samples. As discussed previously, more intense microwave fields will also be required to yield the required coherent electron spin control for efficient DNP at room temperature. Note, this microwave duty cycle is not providing true microwave "pulses" for pulsed DNP applications.

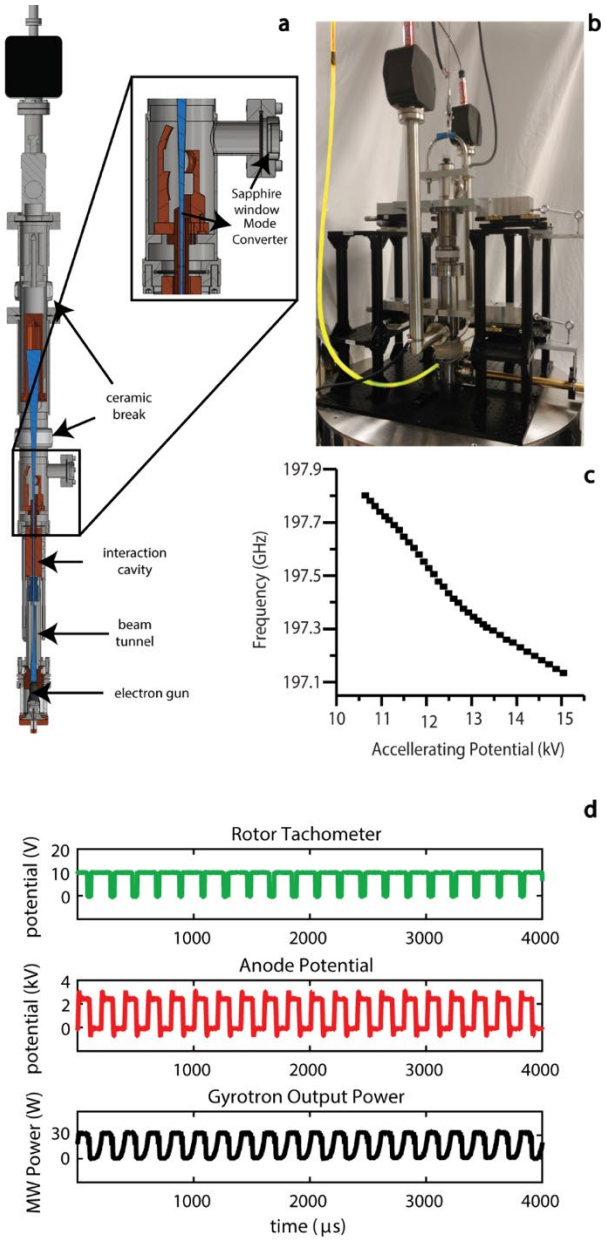

Figure 3.5: a) Computer-Aided Design (CAD) drawing of a 198 GHz gyrotron. b) The gyrotron is connected by the wire highlighted in yellow to a low capacitance amplifier. c) The dependence of the gyrotron output frequency on the applied accelerating voltage. d) Rotor-synchronized microwave power output from the gyrotron. The rotor tachometer reading is shown in green, the gating voltage pulses in red, and the microwave power modulation in black. Figure reproduced with modifications by permission of the Journal of Magnetic Resonance[53].

3.5.1 Improved Electron Nutation Frequencies with Teflon Lenses

In addition to increasing the power generated by the microwave source, Teflon lenses can also increase the electron Rabi frequency by focusing the microwave irradiation into the sample[26]. Figure 3.6a is a simulation of the microwave power distribution of a Gaussian microwave beam irradiating a 4 mm outside diameter MAS rotor[26]. With no lens, a considerable amount of microwave power misses the sample (indicated by the white box). However, by using a cylindrical Teflon lens that compresses the beam along the rotor short axis, a higher portion of the power is focused into the sample (Figure 3.6b)[26]. Figures 3.6c and 3.6d show experiments confirming the results of the simulation without and with the lens, respectively[26].

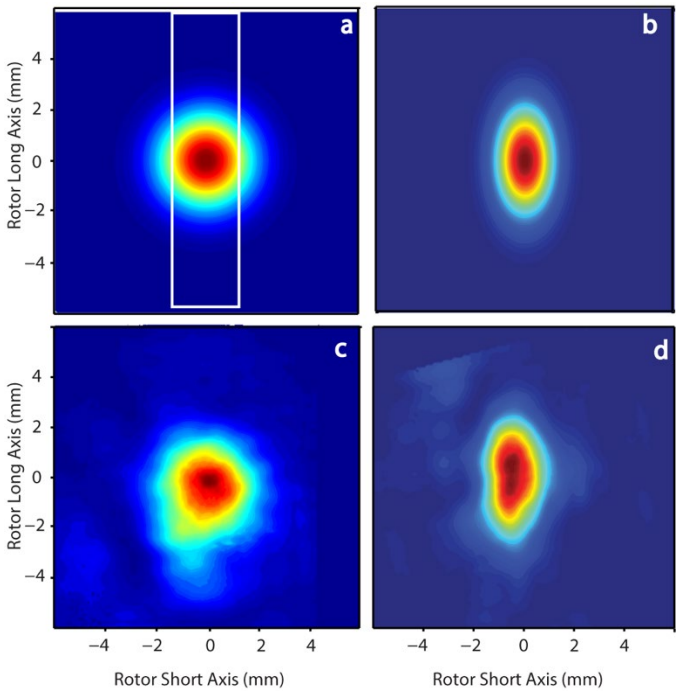

Figure 3.6: a) Simulated power distribution of a Gaussian beam exiting a waveguide. The white box indicates the sample location inside the rotor. b) Simulated effect on the power distribution after the Gaussian beam has passed through a cylindrical lens. c) Experimental verification of (a). d) Experimental verification of (b). Figure reproduced with modifications by permission of the Journal of Magnetic Resonance[26].

3.5.2 Improved Electron Nutation Frequencies with Microwave Resonators

Another route to improve the electron γB_1 is to construct a resonant cavity around the sample[57], as is commonly employed in EPR and static DNP instruments. However, the components required for MAS, such as the bearings and rotor, greatly complicate the implementation of microwave cavities in such a way[27]. One strategy to overcome this problem that has been suggested is to coat the rotor with a thin layer of metal, in order to form a microwave resonance structure within the rotor[57].

An example of the copper coated rotor is shown in Figure 3.7a. The rotor was coated by vacuum deposition to a thickness of 50 nm, with a gap to provide an iris for coupling of the microwave power into the cylindrical cavity. The metal coating is thin enough to pass radio waves, but thick enough to reflect microwaves[57], leveraging the differences in skin-depth at radio and microwave frequencies. This leads to only a mild reduction in ^{13}C signal intensity of metal-coated rotors (Figure 3.7b). Additionally, the resolution of J-couplings is maintained, indicating excellent magnetic field homogeneity even with the rotor surface metalized. The 3.2 mm outside diameter rotors were also able to spin up to 5 kHz, demonstrating that the metal does not create eddy currents sufficient to prohibit MAS.

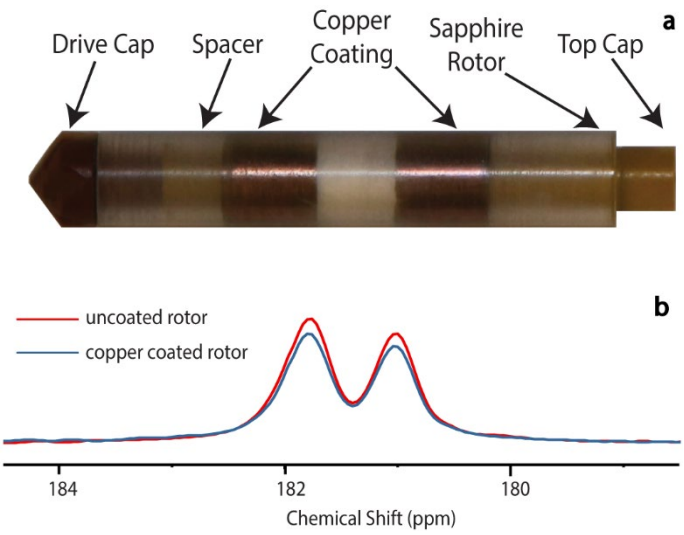

Figure 3.7: Metalized rotors for MAS DNP. a) A rotor coated with copper by vacuum deposition. b) ^{13}C CPMAS spectrum of U-^{13}C sodium acetate at a spinning frequency of 5.4 kHz. The spectrum is an expansion around the carboxyl peak of sodium acetate. The red curve was taken with an uncoated rotor, and a copper coating is present in the blue spectrum. Figure reproduced with modifications with permission from Magnetic Resonance in Chemistry[57].

3.6 Cryogenic MAS DNP Technology

In addition to improving DNP performance at higher temperatures, access to cryogenic temperatures from 4 to 110 K is also an important avenue of technological development. Cryogenic temperatures not only yield excellent sensitivity due to higher Boltzmann polarization, but also provide more accommodating sample properties to demonstrate time domain MAS DNP.

Cryogenic instrumentation for MAS DNP below 80 K has been developed by multiple groups[58–61]. One method employs nitrogen gas to support (bearing) and spin (drive) the sample rotor,

while cold helium gas blows directly on the center of the rotor to cool the sample to 25 K. Elongated 4 mm rotors and Teflon baffles are used to provide physical barriers between the warmer nitrogen, and cooler helium regions. This configuration prevents liquefaction of the nitrogen gas and preserves spinning up to 7 kHz, with a sample temperature of 25 K[58,59,62].

In a similar strategy, the nitrogen gas used for bearing and drive is replaced with chilled helium gas at 80 K (Figure 3.8a)[55]. With this substitution, sample temperatures below 6 K are attainable while maintaining spinning of 6 kHz. Computational fluid dynamics (CFD) was used to optimize the fluid flow, minimize sample temperatures, and also provide a means to measure the sample temperature. For example, a temperature sensor is placed directly in the helium fluid path near the rotor, at which point the CFD calculations indicate the same temperature as the sample. The ^{79}Br T_1 is commonly employed to measure sample temperatures in cryogenic MAS experiments, but below 6 K the ^{79}Br T_1 is too long (>20 minutes) to use as a temperature indicator. Also, in this pure helium implementation of MAS, long rotors are not required as nitrogen liquefaction is no longer an issue. Short rotors permit cryogenic sample exchange, allowing for more than 5 samples to be examined with MAS below 6 K within a 4-hour period. The helium consumption of this apparatus is high (~30 L/hr), but because the cryogen exhaust is pure helium, a closed loop helium recirculation system could be readily implemented[60].

Cryogenic technology for MAS at temperatures > 80 K, which can be conducted with nitrogen cryogens, is important due to the expense and difficulty associated with helium cryogens for MAS. Even though nitrogen cryogens are more affordable than helium, MAS DNP

spectrometers typically require >200 L of N_2(l) per day of operation[63]. The heat exchanger design shown in Figure 3.8b makes use of a counterflow coil to reduce nitrogen consumption. This feature conserves liquid nitrogen by collecting the relatively cold exhaust gas from the probe head, and using it to pre-cool incoming warm nitrogen gas. A lower temperature of the incoming spinning gases reduces the amount of boil-off of the liquid nitrogen cooling reservoir, and results in a liquid nitrogen consumption of only 90 L/day when conducting MAS experiments[32].

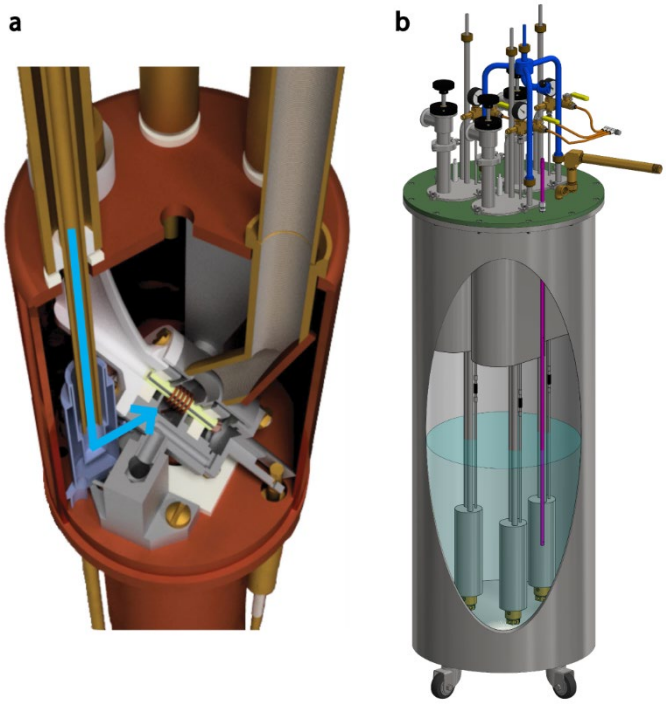

Figure 3.8: Cryogenic technology used in DNP MAS NMR experiments from room temperature to 4.2 K. a) NMR probe head showing the path of the VT helium fluid (shown by the blue arrow) onto the sample. b) Heat exchanger that is used to cool drive, bearing, and VT fluids to 80-100 K. These figures were reproduced with permission from the Journal of Magnetic Resonance[32,55].

3.7 Conclusion

MAS DNP is widely used to increase NMR signal intensity. The CW DNP methods currently employed in conjunction with MAS will eventually be replaced with time domain DNP and subsequent pulsed electron decoupling which are a promising pathway towards efficient DNP at room temperature. While room temperature DNP has many advantages, performing experiments at temperatures below 6 K will result in unparalleled NMR sensitivity. Coherent EPR control together with MAS NMR is expected to provide a powerful experimental platform leading to many high-impact directions of research in magnetic resonance.

Frequency-chirped microwaves generated with frequency-agile gyrotron oscillators provide a direct route to coherent EPR control using currently accessible technology. Time domain DNP methods using frequency chirps have already been implemented during the acquisition of the NMR signal, effectively decoupling the electrons from the nuclei. Further development of DNP instrumentation will yield significant improvements in the repertoire and performance of pulsed electron decoupling and MAS DNP experiments. High power frequency-agile gyrotrons, Teflon lenses, and spinning microwave resonators will result in coherent control of electron spins in MAS experiments. Time domain DNP and pulsed electron decoupling will ensure magnetic resonance continues to be a fertile field of research in the coming decades.

References

(1) Rossini, A. J.; Widdifield, C. M.; Zagdoun, A.; Lelli, M.; Schwarzwälder, M.; Copéret, C.; Lesage, A.; Emsley, L. Dynamic Nuclear Polarization Enhanced NMR Spectroscopy

for Pharmaceutical Formulations. *J. Am. Chem. Soc.* **2014**, *136* (6), 2324–2334.

(2) Mak-Jurkauskas, M. L.; Bajaj, V. S.; Hornstein, M. K.; Belenky, M.; Griffin, R. G.; Herzfeld, J. Energy Transformations Early in the Bacteriorhodopsin Photocycle Revealed by DNP-Enhanced Solid-State NMR. *Proc. Natl. Acad. Sci.* **2008**, *105* (3), 883–888.

(3) Hayes, S.; Van Wüllen, L.; Eckert, H.; Even, W. R.; Crocker, R. W.; Zhang, Z. Solid-State NMR Strategies for the Structural Investigation of Carbon-Based Anode Materials. *Chem. Mater.* **1997**, *9* (4), 901–911.

(4) Kaplan, M.; Narasimhan, S.; de Heus, C.; Mance, D.; van Doorn, S.; Houben, K.; Popov-Čeleketić, D.; Damman, R.; Katrukha, E. A.; Jain, P.; et al. EGFR Dynamics Change during Activation in Native Membranes as Revealed by NMR. *Cell* **2016**, *167* (5), 1241–1251.e11.

(5) Baker, L. A.; Sinnige, T.; Schellenberger, P.; de Keyzer, J.; Siebert, C. A.; Driessen, A. J. M.; Baldus, M.; Grünewald, K. Combined 1H-Detected Solid-State NMR Spectroscopy and Electron Cryotomography to Study Membrane Proteins across Resolutions in Native Environments. *Structure* **2018**, *26* (1), 161–170.e3.

(6) Barnes, A. B.; Corzilius, B.; Mak-Jurkauskas, M. L.; Andreas, L. B.; Bajaj, V. S.; Matsuki, Y.; Belenky, M. L.; Lugtenburg, J.; Sirigiri, J. R.; Temkin, R. J.; et al. Resolution and Polarization Distribution in Cryogenic DNP/MAS Experiments. **2010**, *14* (4), 384–399.

(7) Barnes, A. B.; Andreas, L. B.; Huber, M.; Ramachandran, R.; van der Wel, P. C. A.; Veshtort, M.; Griffin, R. G.; Mehta, M. A. High-Resolution Solid-State NMR Structure of Alanyl-Prolyl-Glycine. *J. Magn. Reson.* **2009**, *200* (1), 95–100.

(8) Gullion, T.; Schaefer, J. Rotational-Echo Double-Resonance NMR. *J. Magn. Reson.* **1989**, No. 81, 196–200.

(9) Yang, H.; Staveness, D.; Ryckbosch, S. M.; Axtman, A. D.; Loy, B. A.; Barnes, A. B.; Pande, V. S.; Schaefer, J.; Wender, P. A.; Cegelski, L. REDOR NMR Reveals Multiple Conformers for a Protein Kinase c Ligand in a Membrane Environment. *ACS Cent. Sci.* **2018**, *4* (1), 89–96.

(10) Jaroniec, C. P.; Filip, C.; Griffin, R. G. 3D TEDOR NMR Experiments for the Simultaneous Measurement of Multiple Carbon-Nitrogen Distances in Uniformly 13C,15N-Labeled Solids. *J. Am. Chem. Soc.* **2002**, *124* (36), 10728–10742.

(11) Braunschweiler, L.; Ernst, R. R. Coherence Transfer by Isotropic Mixing: Application to Proton Correlation Spectroscopy. *J. Magn. Reson.* **1983**, *53* (3), 521–528.

(12) Castellani, F.; Rossum, B. Van; Diehl, A.; Schubert, M.; Rehbein, K.; Oschkinat, H. Structure of a Protein Determined by Solid-State Magic-Angle-Spinning NMR Spectroscopy. **2002**, *420* (November), 23–26.

(13) Lewandowski, J. R.; Dumez, J. N.; Akbey, Ü.; Lange, S.; Emsley, L.; Oschkinat, H. Enhanced Resolution and Coherence Lifetimes in the Solid-State NMR Spectroscopy of Perdeuterated Proteins under Ultrafast Magic-Angle Spinning. *J. Phys. Chem. Lett.* **2011**, *2* (17), 2205–2211.

(14) Marchetti, A.; Jehle, S.; Felletti, M.; Knight, M. J.; Wang, Y.; Xu, Z. Q.; Park, A. Y.; Otting, G.; Lesage, A.; Emsley, L.; et al. Backbone Assignment of Fully Protonated Solid Proteins By1H Detection and Ultrafast Magic-Angle-Spinning NMR Spectroscopy. *Angew. Chemie - Int. Ed.* **2012**, *51* (43), 10756–10759.

(15) Vasa, S. K.; Janssen, H.; Van Eck, E. R. H.; Kentgens, A. P. M. High-Resolution Solid-State ^{13} C MMAS NMR with Long Coherence Life Times. *Phys. Chem. Chem. Phys.* **2011**, *13* (1), 104–106.

(16) Renault, M.; Pawsey, S.; Bos, M. P.; Koers, E. J.; Nand, D.; Tommassen-Van Boxtel, R.; Rosay, M.; Tommassen, J.; Maas, W. E.; Baldus, M. Solid-State NMR Spectroscopy on Cellular Preparations Enhanced by Dynamic Nuclear Polarization. *Angew. Chemie - Int. Ed.* **2012**, *51* (12), 2998–3001.

(17) Carver, T. R.; Slichter, C. P. Polarization of Nuclear Spins in Metals. *Phys. Rev.* **1953**, *92* (1), 212–213.

(18) Kubicki, D. J.; Rossini, A. J.; Purea, A.; Zagdoun, A.; Ouari, O.; Tordo, P.; Engelke, F.; Lesage, A.; Emsley, L. Amplifying Dynamic Nuclear Polarization of Frozen Solutions by Incorporating Dielectric Particles. *J. Am. Chem. Soc.* **2014**, *136* (44), 15711–15718.

(19) Lilly Thankamony, A. S.; Wittmann, J. J.; Kaushik, M.; Corzilius, B. Dynamic Nuclear Polarization for Sensitivity Enhancement in Modern Solid-State NMR. *Prog. Nucl. Magn. Reson. Spectrosc.* **2017**, *102–103*, 120–195.

(20) Traficante, D. D. Introduction to Transmission Lines Basic Principles and Applications of Quarter Wavelength Cables and Impedance Matching. *Concepts Magn. Reson.* **1993**, *5* (1), 57–86.

(21) Traficante, D. D. Imepedance: What It Is, and Why It Must Be Matched. *Concepts Magn. Reson.* **1989**, *1*, 73–92.

(22) Barnes, A. B.; Mak-Jurkauskas, M. L.; Matsuki, Y.; Bajaj, V. S.; van der Wel, P. C. A.;

DeRocher, R.; Bryant, J.; Sirigiri, J. R.; Temkin, R. J.; Lugtenburg, J.; et al. Cryogenic Sample Exchange NMR Probe for Magic Angle Spinning Dynamic Nuclear Polarization. *J. Magn. Reson.* **2009**, *198* (2), 261–270.

(23) Fu, R.; Brey, W. W.; Shetty, K.; Gor'kov, P.; Saha, S.; Long, J. R.; Grant, S. C.; Chekmenev, E. Y.; Hu, J.; Gan, Z.; et al. Ultra-Wide Bore 900 MHz High-Resolution NMR at the National High Magnetic Field Laboratory. *J. Magn. Reson.* **2005**, *177* (1), 1–8.

(24) Leavesley, A.; Wilson, C. B.; Sherwin, M.; Han, S. Effect of Water/Glycerol Polymorphism on Dynamic Nuclear Polarization. *Phys. Chem. Chem. Phys.* **2018**, *20* (15), 9897–9903.

(25) van der Cruijsen, E. A. W.; Koers, E. J.; Sauvée, C.; Hulse, R. E.; Weingarth, M.; Ouari, O.; Perozo, E.; Tordo, P.; Baldus, M. Biomolecular DNP-Supported NMR Spectroscopy Using Site-Directed Spin Labeling. *Chem. - A Eur. J.* **2015**, *21* (37), 12971–12977.

(26) Nanni, E. a.; Barnes, A. B.; Matsuki, Y.; Woskov, P. P.; Corzilius, B.; Griffin, R. G.; Temkin, R. J. Microwave Field Distribution in a Magic Angle Spinning Dynamic Nuclear Polarization NMR Probe. *J. Magn. Reson.* **2011**, *210* (1), 16–23.

(27) Barnes, A. B.; Nanni, E. A.; Herzfeld, J.; Griffin, R. G.; Temkin, R. J. A 250 GHz Gyrotron With a 3 GHz Tuning Bandwidth for Dynamic Nuclear Polarization. **2013**, No. 221, 147–153.

(28) Michaelis, V. K.; Smith, A. a.; Corzilius, B.; Haze, O.; Swager, T. M.; Griffin, R. G. High-Field 13C Dynamic Nuclear Polarization with a Radical Mixture. *J. Am. Chem. Soc.* **2013**, *135* (8), 2935–2938.

(29) Maly, T.; Debelouchina, G. T.; Bajaj, V. S.; Hu, K.-N.; Joo, C.-G.; Mak-Jurkauskas, M. L.; Sirigiri, J. R.; van der Wel, P. C. a; Herzfeld, J.; Temkin, R. J.; et al. Dynamic Nuclear Polarization at High Magnetic Fields. *J. Chem. Phys.* **2008**, *128* (5), 052211.

(30) Hu, K. N.; Bajaj, V. S.; Rosay, M.; Griffin, R. G. High-Frequency Dynamic Nuclear Polarization Using Mixtures of TEMPO and Trityl Radicals. *J. Chem. Phys.* **2007**, *126* (4).

(31) Corzilius, B.; Smith, A. A.; Griffin, R. G. Solid Effect in Magic Angle Spinning Dynamic Nuclear Polarization. *J. Chem. Phys.* **2012**, *137* (5), 054201.

(32) Albert, B. J.; Pahng, S. H.; Alaniva, N.; Sesti, E. L.; Rand, P. W.; Saliba, E. P.; Scott, F. J.; Choi, E. J.; Barnes, A. B. Instrumentation for Cryogenic Magic Angle Spinning Dynamic Nuclear Polarization Using 90 L of Liquid Nitrogen per Day. *J. Magn. Reson.* **2017**, *283*.

(33) Lelli, M.; Chaudhari, S. R.; Gajan, D.; Casano, G.; Rossini, A. J.; Ouari, O.; Tordo, P.; Lesage, A.; Emsley, L. Solid-State Dynamic Nuclear Polarization at 9.4 and 18.8 T from 100 K to Room Temperature. *J. Am. Chem. Soc.* **2015**, *137* (46), 14558–14561.

(34) Chaudhari, S. R.; Berruyer, P.; Gajan, D.; Reiter, C.; Engelke, F.; Silverio, D. L.; Copéret, C.; Lelli, M.; Lesage, A.; Emsley, L. Dynamic Nuclear Polarization at 40 KHz Magic Angle Spinning. *Phys. Chem. Chem. Phys.* **2016**, *18* (15), 10616–10622.

(35) Afeworki, M.; Schaefer, J. Mechanism of DNP-Enhanced Polarization Transfer across the Interface of Polycarbonate/Polystyrene Heterogeneous Blends. *Macromolecules* **1992**, *25* (16), 4092–4096.

(36) Becerra, L. R.; Gerfen, G. J.; Temkin, R. J.; Singel, D. J.; Griffin, R. G. Dynamic Nuclear Polarization with a Cyclotron Resonance Maser at 5 T. *Phys. Rev. Lett.* **1993**, *71* (21), 3561–3564.

(37) Keedy, D. A.; Van Den Bedem, H.; Sivak, D. A.; Petsko, G. A.; Ringe, D.; Wilson, M. A.; Fraser, J. S. Crystal Cryocooling Distorts Conformational Heterogeneity in a Model Michaelis Complex of DHFR. *Structure* **2014**, *22* (6), 899–910.

(38) Ni, Q. Z.; Markhasin, E.; Can, T. V.; Corzilius, B.; Tan, K. O.; Barnes, A. B.; Daviso, E.; Su, Y.; Herzfeld, J.; Griffin, R. G. Peptide and Protein Dynamics and Low-Temperature/DNP Magic Angle Spinning NMR. *J. Phys. Chem. B* **2017**, *121* (19), 4997–5006.

(39) Fricke, P.; Mance, D.; Chevelkov, V.; Giller, K.; Becker, S.; Baldus, M.; Lange, A. High Resolution Observed in 800 MHz DNP Spectra of Extremely Rigid Type III Secretion Needles. *J. Biomol. NMR* **2016**, *65* (3–4), 121–126.

(40) Sergeyev, I. V.; Itin, B.; Rogawski, R.; Day, L. A.; McDermott, A. E. Efficient Assignment and NMR Analysis of an Intact Virus Using Sequential Side-Chain Correlations and DNP Sensitization. *Proc. Natl. Acad. Sci.* **2017**, *114* (20), 5171–5176.

(41) Henstra, A.; Dirksen, P.; Schmidt, J.; Wenckebach, W. T. Nuclear Spin Orientation via Electron Spin Locking (NOVEL). *J. Magn. Reson.* **1988**, *77*, 389–393.

(42) Can, T. V.; Weber, R. T.; Walish, J. J.; Swager, T. M.; Griffin, R. G. Frequency-Swept Integrated Solid Effect. *Angew. Chemie - Int. Ed.* **2017**, *56* (24), 6744–6748.

(43) Jain, S. K.; Mathies, G.; Griffin, R. G. Off-Resonance NOVEL. *J. Chem. Phys.* **2017**, *147*

(16), 164201.

(44) Jain, S. K.; Siaw, T. A.; Equbal, A.; Wilson, C. B.; Kaminker, I.; Han, S. Reversal of Paramagnetic Effects by Electron Spin Saturation. *J. Phys. Chem. C* **2018**, *122* (10), 5578–5589.

(45) Saliba, E. P.; Sesti, E. L.; Scott, F. J.; Albert, B. J.; Choi, E. J.; Alaniva, N.; Gao, C.; Barnes, A. B. Electron Decoupling with Dynamic Nuclear Polarization in Rotating Solids. *J. Am. Chem. Soc.* **2017**, *139* (18).

(46) Henstra, a; Dirksen, P.; Wenckebach, W. T. Enhanced Dynamic Nuclear Polarization by the Integrated Solid Effect. *Phys. Lett. A* **1988**, *134* (2), 134–136.

(47) Weis, V.; Griffin, R. G. Electron-Nuclear Cross Polarization. *Solid State Nucl. Magn. Reson.* **2006**, *29* (1–3), 66–78.

(48) Rizzato, R.; Bennati, M. Cross-Polarization Electron-Nuclear Double Resonance Spectroscopy. *ChemPhysChem* **2015**, *16* (18), 3769–3773.

(49) Hoff, D. E. M.; Albert, B. J.; Saliba, E. P.; Scott, F. J.; Choi, E. J.; Mardini, M.; Barnes, A. B. Frequency Swept Microwaves for Hyperfine Decoupling and Time Domain Dynamic Nuclear Polarization. *Solid State Nucl. Magn. Reson.* **2015**, *72*, 79–89.

(50) Equbal, A.; Li, Y.; Leavesley, A.; Huang, S.; Rajca, S.; Rajca, A.; Han, S. Truncated Cross Effect Dynamic Nuclear Polarization: An Overhauser Effect Doppelgänger. *J. Phys. Chem. Lett.* **2018**, *9* (9), 2175–2180.

(51) Kwikam, A. L. Electron Nuclear Double Resonance. *Annu. Rev. Phys. Chem.* **1971**, *700* (22), 133–170.

(52) Rowan, L. G.; Hahn, E. L.; Mims, W. B. Electron-Spin-Echo Envelope Modulation. *Phys. Rev.* **1965**, *137* (1), A61–A71.

(53) Scott, F. J.; Saliba, E. P.; Albert, B. J.; Alaniva, N.; Sesti, E. L.; Gao, C.; Golota, N. C.; Choi, E. J.; Jagtap, A. P.; Wittmann, J. J.; et al. Frequency-Agile Gyrotron for Electron Decoupling and Pulsed Dynamic Nuclear Polarization. *J. Magn. Reson.* **2018**, *289*.

(54) Nusinovich, G. S. *Intrduction to the Physics of Gyrotrons*; Johns Hopkins University Press, 2004.

(55) Sesti, E. L.; Alaniva, N.; Rand, P. W.; Choi, E. J.; Albert, B. J.; Saliba, E. P.; Scott, F. J.; Barnes, A. B. Magic Angle Spinning NMR below 6 K with a Computational Fluid Dynamics Analysis of Fluid Flow and Temperature Gradients. *J. Magn. Reson.* **2018**, *286*.

(56) Haze, O.; Corzilius, B.; Smith, A. a.; Griffin, R. G.; Swager, T. M. Water-Soluble Narrow-Line Radicals for Dynamic Nuclear Polarization. *J. Am. Chem. Soc.* **2012**, *134* (35), 14287–14290.

(57) Scott, F. J.; Sesti, E. L.; Choi, E. J.; Laut, A. J.; Sirigiri, J. R.; Barnes, A. B. Magic Angle Spinning NMR with Metallized Rotors as Cylindrical Microwave Resonators. *Magn. Reson. Chem.* **2018**.

(58) Thurber, K. R.; Potapov, A.; Yau, W. M.; Tycko, R. Solid State Nuclear Magnetic Resonance with Magic-Angle Spinning and Dynamic Nuclear Polarization below 25 K. *J. Magn. Reson.* **2013**, *226*, 100–106.

(59) Thurber, K. R.; Tycko, R. Biomolecular Solid State NMR with Magic-Angle Spinning at 25 K. **2009**, *195* (2), 179–186.

(60) Lee, D.; Bouleau, E.; Saint-Bonnet, P.; Hediger, S.; De Paëpe, G. Ultra-Low Temperature MAS-DNP. *J. Magn. Reson.* **2016**, *264*, 116–124.

(61) Matsuki, Y.; Idehara, T.; Fukazawa, J.; Fujiwara, T. Advanced Instrumentation for DNP-Enhanced MAS NMR for Higher Magnetic Fields and Lower Temperatures. *J. Magn. Reson.* **2016**, *264*, 107–115.

(62) Thurber, K. R.; Yau, W. M.; Tycko, R. Low-Temperature Dynamic Nuclear Polarization at 9.4 T with a 30 mW Microwave Source. *J. Magn. Reson.* **2010**, *204* (2), 303–313.

(63) Barnes, A. B.; Markhasin, E.; Daviso, E.; Michaelis, V. K.; Nanni, E. A.; Jawla, S.; Mena, E. L.; DeRocher, R.; Thakkar, A.; Woskov, P. P.; et al. Dynamic Nuclear Polarization at 700 MHz/460 GHz. **2012**, No. 224, 1–7.

Chapter 4: Electron Decoupling with Dynamic Nuclear Polarization in Rotating Solids

Forward

This chapter was adapted from the paper "Electron Decoupling with Dynamic Nuclear Polarization in Rotating Solids" by Edward P. Saliba, Erika L. Sesti, Faith J. Scott, Brice J. Albert, Eric J. Choi, Nicholas Alaniva, Chukun Gao, and Alexander B. Barnes and describes the initial work that was performed in the implementation of the first electron decoupling experiments. This is an unofficial adaptation of an article that appeared in an ACS publication. ACS has not endorsed the content of this adaptation or the context of its use. The goal of electron decoupling is to mitigate the paramagnetic effects of the radical that has been introduced for DNP. This is important because future electron decoupling experiments performed using direct transfer DNP in dipolar recoupling sequences such as rotational echo double resonance (REDOR) and others that involve an evolution time. If a significant amount of magnetization is lost to homogeneous interactions that cannot be refocused by an echo, it can cause these experiments to become prohibitively long. The resolution that is characteristic of NMR also needs to be maintained. One of the most important results of this paper is that the effectiveness of the decoupling becomes greater at shorter polarization times, which will be highly pertinent in future direct transfer DNP experiments. Citation: Saliba, E. P.; Sesti, E. L.; Scott, F. J.; Albert, B. J.; Choi, E. J.; Alaniva, N.; Gao, C.; Barnes, A. B. Electron Decoupling with Dynamic Nuclear Polarization in Rotating Solids. *J. Am. Chem. Soc.* 2017, *139* (18), 6310–6313.

Abstract

Dynamic nuclear polarization (DNP) can enhance NMR sensitivity by orders of magnitude by transferring spin polarization from electrons to nuclei. However, paramagnetic DNP polarizing agents can have deleterious effects on NMR signals. Electron spin decoupling can mitigate these paramagnetic relaxation effects. Following a DNP and spin diffusion period, the microwave irradiation frequency is quickly tuned on-resonance with unpaired electrons on the DNP polarizing agent. The electron decoupling performance shows a strong dependence on the microwave frequency and DNP polarization time. Microwave frequency sweeps through the EPR lineshape are shown as a time domain strategy to significantly improve electron decoupling. For ^{13}C spins on biomolecules frozen in a glassy matrix, electron decoupling reduces linewidths by 11% (47 Hz) and increases intensity by 14%.

4.1 Introduction

Dynamic nuclear polarization (DNP) transfers electronic spin polarization to nuclei and has been demonstrated to increase NMR sensitivity by orders of magnitude[1–4]. The enhanced sensitivity can be applied to characterize a wide range of molecular architectures of interest to the biomedical and materials science communities[5–8]. However, paramagnetic DNP polarizing agents can have deleterious effects on NMR signals, such as line broadening and signal quenching[9–12].

Spin decoupling is commonly used in NMR experiments to reduce similar undesired interactions and extend nuclear relaxation times[13]. The resulting spin-decoupled spectrum is typically better resolved and has higher signal-to-noise. Whereas low-power decoupling schemes in solution NMR are sufficient to eliminate scalar J-couplings[14], higher-power radio frequency decoupling fields are generally required to attenuate strong proton dipolar interactions in NMR of solids[15]. In solids, proton decoupling is commonly employed after a cross polarization (CP) period, which transfers magnetization from protons to nuclei with a lower gyromagnetic ratio[16], similar to DNP. The CP experiment, followed by proton decoupling, not only results in higher signal-to-noise per transient, but also shortens the magnetization recovery delay between transients due to faster longitudinal relaxation of the proton spins.

Electron decoupling (hyperfine decoupling) has previously been applied to static electron paramagnetic resonance (EPR) experiments, in which requirements for magic angle spinning (MAS) do not complicate cryogenic cooling or microwave cavity design[17,18]. In quantum computing, hyperfine decoupling (also known as dynamical decoupling) has been applied to lengthen electron relaxation times[19]. Electron decoupling was first proposed for MAS DNP using microwave amplifiers by Griffin and colleagues[9], and our laboratory suggested a technical strategy for implementation using frequency agile gyrotrons[20]. In this chapter, the first electron decoupling experiments combined with DNP and MAS NMR are presented. Similar to proton decoupled CP, electron decoupled DNP results narrower ^{13}C resonances.

4.2 Electron Decoupling Pulse Sequence

The electron decoupling DNP pulse sequence shown in Figure 4.1 is implemented with an NMR spectrometer featuring an integrated, custom built frequency-agile gyrotron operating in the fundamental cyclotron resonance[21]. High energy electrons deposit microwave power into a $TE_{5,2}$ mode within the interaction cavity, and continuous frequency tuning is achieved by accessing hybridized axial modes[22–25]. The frequency of the microwave power generated is related to the initial accelerating voltage experienced by the electrons. An arbitrary waveform generator (AWG) whose waveform is amplified by a TREK amplifier is used to accomplish this on the order of microseconds. The AWG is controlled directly from the NMR spectrometer interface, enabling synchronized microwave and radio frequency (RF) irradiation[20]. Spectrometer control of the EPR channel also facilitates the adjustment of the microwave parameters to optimize electron decoupling.

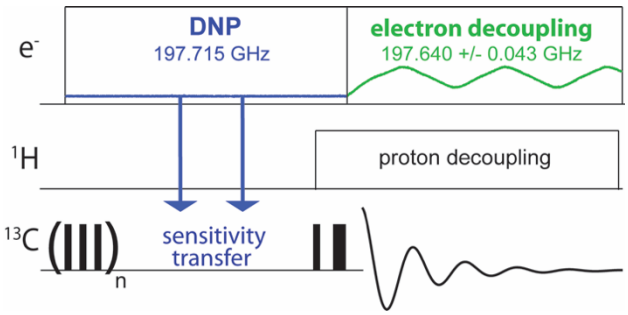

Figure 4.1: Electron decoupling DNP NMR pulse sequence. On the electron channel, the microwave frequency is set to the zero quantum ^{13}C solid effect condition (197.715 GHz) for DNP. Electron decoupling is employed during the signal acquisition by sweeping over the electron resonance, centered at 197.640 GHz. ^{13}C magnetization is destroyed with a saturation train, which is followed by the DNP polarization time. The ^{13}C signal is acquired with a rotor synchronized Hahn echo (τ = 250 μs, $\omega_{1C}/2\pi$ = 83 KHz during pulses) and TPPM is used for proton decoupling with $\omega_{1H}/2\pi$ = 77 KHz[15].

An example of how the voltage on the gyrotron anode is modulated is shown in Figure 4.2. The nominal output frequency of the gyrotron (when the AWG is set to 0% output) is set to 197.715 GHz, which corresponds to the zero quantum solid effect condition. When electron decoupling is to be performed, the anode voltage is used to rapidly chirp the microwave frequency through the Trityl resonance. The black curve in Figure 4.2a was measured directly out of the arbitrary waveform generator on an oscilloscope. The red one is $0.001 \times$ the anode voltage as measured out of the TREK amplifier. The amplifier shapes the input waveform to a small extent, but it mostly stays true to the AWG input. The traces in Figure 4.2b show how the anode voltage is modulated when electron decoupling is not being performed for comparison to the electron decoupled spectrum. In this case the chirps are centered around a frequency that is far off of any DNP condition or electron resonance frequency. This is done to make sure that microwave heating does not cause a narrowing of the resonance between the two.

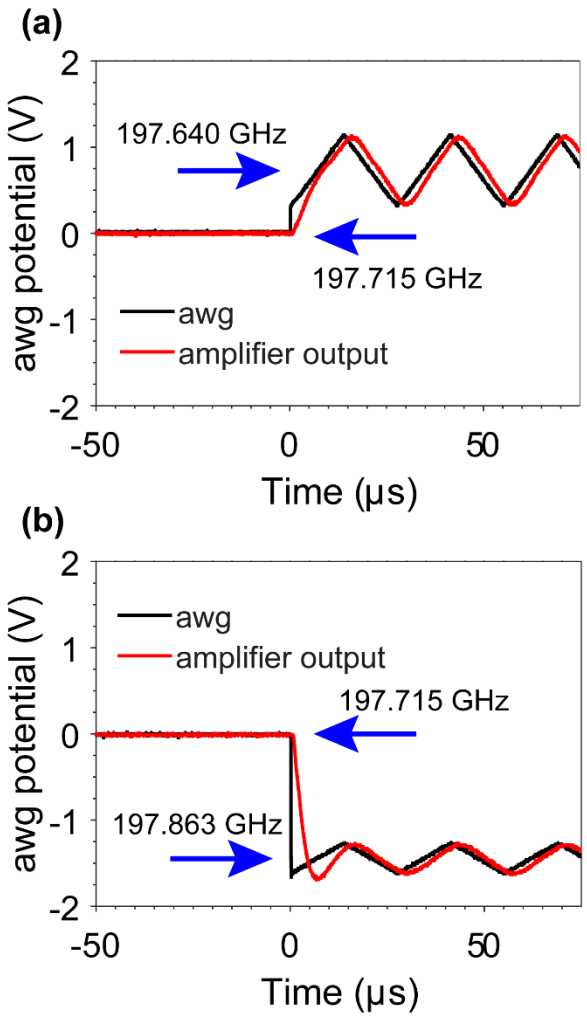

Figure 4.2: The anode voltage modulation used in electron decoupling experiments (a) and when electron decoupling is not performed for a control experiment (b).

The intensity of the oscillating magnetic field, and the resulting nutation frequency of the electron spins ($\gamma_S B_{1S} = \omega_{1S}/2\pi$, also known as the Rabi frequency) is an important factor in understanding DNP, and also electron decoupling. The average $\omega_{1S}/2\pi$ across the sample was computed to be 0.38 MHz, given 5 W of microwave input power into the sample chamber.

4.3 Results

DNP mechanisms fulfill matching conditions among EPR, NMR, and microwave frequencies. The solid effect DNP mechanism is active when the microwave irradiation frequency is offset from the EPR frequency by the nuclear Larmor frequency[26]. Microwave irradiation of the zero quantum solid effect condition at 197.715 GHz results in increased polarization of ^{13}C spins. Trityl Finland radical at 40 mM is used as the DNP polarizing agent, due to the relatively narrow electron spin resonance, long spin relaxation, and weak intramolecular hyperfine interactions[27]. Trityl is mixed with 4M [^{13}C,^{15}N]-urea in a cryoprotecting glassy matrix of D_8-glycerol/D_2O/H_2O (60%/30%/10% by volume), cooled to 90 K, and spun at 4 kHz.

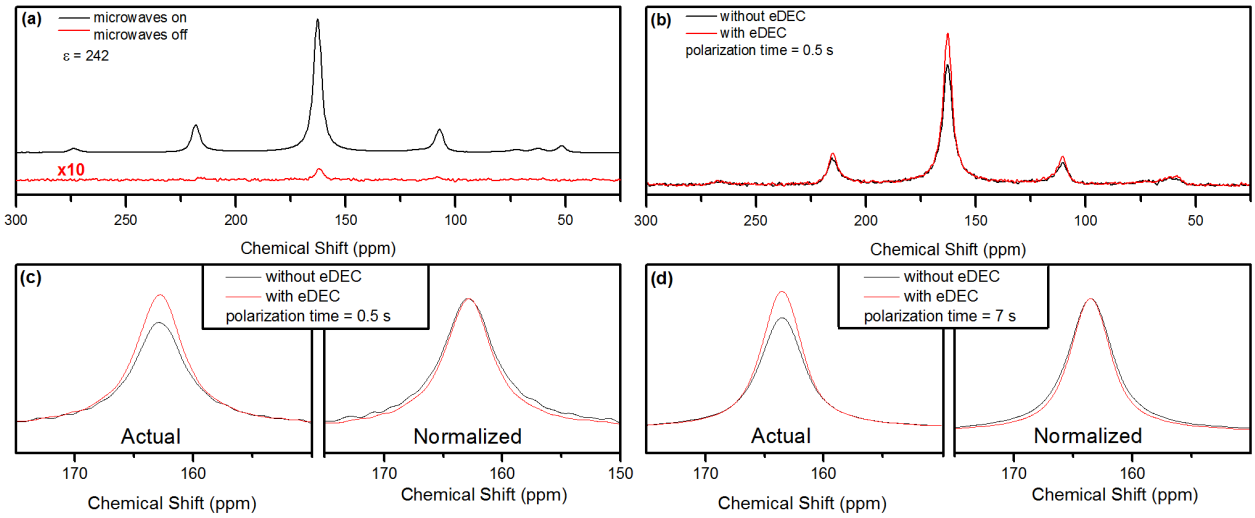

Figure 4.3: DNP MAS NMR spectra at 7 Tesla (^{13}C Larmor frequency of 75.495 MHz). (a) ^{13}C enhancement (without electron decoupling) with a 7 second polarization time. The enhancement is 242. (b) Comparison of DNP spectra with (red) and without (black) electron decoupling at a polarization time of 0.5 seconds. (c,d) Expansion of the isotropic urea resonance with 0.5 and 7.0 second polarization times. Electron decoupling exhibits increased NMR intensity and resonance narrowing at both polarization times. The un-normalized spectra show the intensity increase under electron decoupling. The normalized spectra show the decrease in linewidth.

The DNP enhancement shown in Figure 4.3a is 242. For electron decoupling after the DNP polarization period, the microwave frequency is centered on resonance with the electron spins at 197.640 GHz. The difference in frequency between the solid effect condition and the electron resonance frequency corresponds to the ^{13}C Larmor frequency of 75 MHz. Figure 4.3b-d shows the effect of electron decoupling on ^{13}C MAS NMR spectra. The electron-decoupled spectrum exhibits narrower resonances at a higher intensity. The microwave frequency during the experiment without electron decoupling is shifted to 197.863 GHz, far from the solid effect conditions and the electron resonance. In this way the microwave irradiation is still present during acquisition. The consistent microwave irradiation for experiments with and without electron decoupling confirms that the observed resonance narrowing is due to electron decoupling and not sample heating.

The central ^{13}C resonances recorded with electron decoupling have larger integrals, and longer observed transverse relaxation times (T_2*). For example, the integrals of the resonances with decoupling at polarization times of 0.5 s and 7 s are 13.84% ± 0.21% and 9.9% ± 0.14% larger than without electron decoupling, respectively. The T_2* without electron decoupling is 0.9447 ± 0.0006 ms versus 1.0415 ± 0.0014 ms with electron decoupling for a 7 s polarization time. Similar improvements in the transverse relaxation times are observed at shorter polarization times. For example, without electron decoupling the T_2* at 0.5 seconds is 0.7687 ms ± 0.0097 ms versus 0.8577 ms ± 0.0075 ms with electron decoupling. Furthermore, implementing electron decoupling during a rotor synchronized Carr-Purcell-Meiboom-Gill (CPMG) echo train with a 7 s polarization time increases the refocused transverse ^{13}C relaxation time (T_2') from 1.98 ms ± 0.11 ms to 2.20 ms ± 0.11 ms. This suggests that electron decoupling is attenuating homogenous

hyperfine interactions to a small extent[28]. The result of the CPMG experiment used to measure these relaxation times is shown in Figure 4.4, with the top echo train being taken with no electron decoupling, and the on the bottom with electron decoupling.

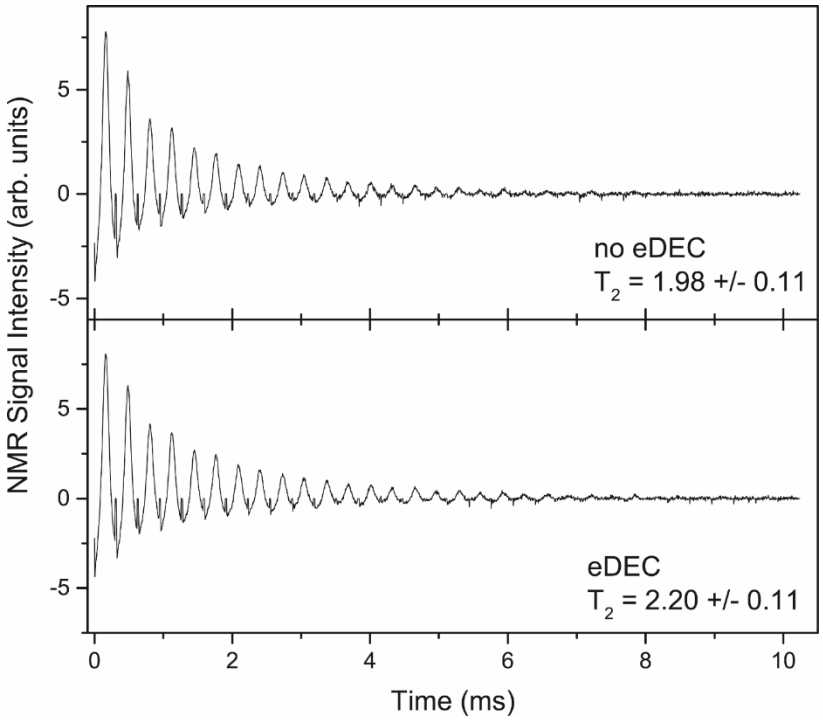

Figure 4.4: CPMG experiments performed without electron decoupling (top), and with electron decoupling (bottom) at 7 seconds of polarization time.

The larger overall intensity of the resonance suggests more ^{13}C spins near the radical are contributing to the free induction decay in the electron decoupled spectrum. The electron decoupling is on during the acquisition period which begins directly after the π pulse of the Hahn echo (pulse sequence shown in Figure 4.1). The integral of the signal in the frequency domain is proportional to the first point of the data series in the time domain prior to the Fourier transform. Therefore, transverse ^{13}C magnetization is retained after the refocusing pulse due to electron

decoupling, and the integral of the resonances in Figure 4.3b-d are larger with electron decoupling.

Note that the gain in signal intensity cannot be due to additional DNP transfer during the signal acquisition. On-resonance DNP mechanisms such as the Overhauser effect generate longitudinal magnetization[29], and would not be observed in the transverse plane.

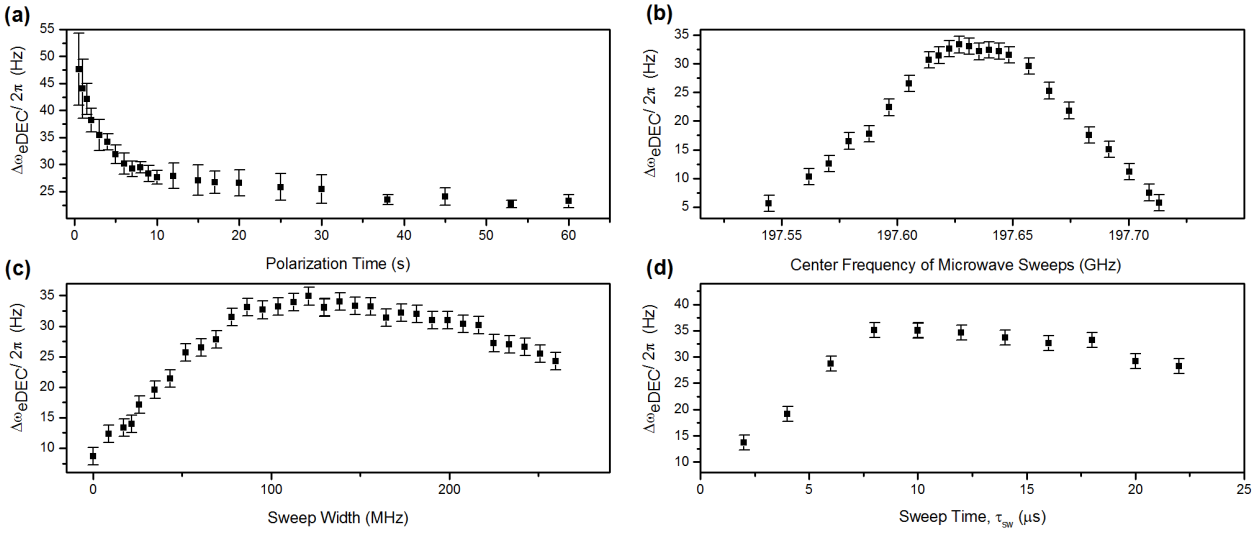

Figure 4.5: Dependences of NMR linewidth differences with and without electron decoupling, $\Delta\omega_{eDEC}/2\pi$, on experimental parameters. The isotropic ^{13}C Urea resonance was fit using DMfit,[30] in which the Lorentzian vs. Gaussian composition was allowed to vary during the fit. Linewidths are reported as full width at half maximum (FWHM) **(a)** Dependence of electron decoupling on the polarization time. The change in $\Delta\omega_{eDEC}/2\pi$ increases drastically with polarization times below 20 seconds. **(b)** Dependence of electron decoupling on the center frequency of the decoupling sweeps, using a sweep width of 90 MHz. **(c)** Dependence of electron decoupling on the decoupling sweep width. $\Delta\omega_{eDEC}/2\pi$ has a maximum at a sweep width of 130 MHz. **(d)** Dependence of electron decoupling on microwave sweep time, τ_{SW}.

The difference between NMR linewidths with and without electron decoupling, defined as $\Delta\omega_{eDEC}/2\pi$, is an indicator of electron decoupling performance. Integrating the EPR control into the NMR spectrometer enables the acquisition of transients with and without electron decoupling on alternating scans to minimize error between combined data sets. The $\Delta\omega_{eDEC}/2\pi$ dependence

on the polarization time is shown in Figure 4.5a. The carbon resonance narrows from 339 Hz to 306 Hz under electron decoupling with a 7 second polarization time, compared with 419 Hz to 371 Hz at 0.5 seconds. The ^{13}C-^{13}C spin diffusion spreads the enhanced magnetization away from the paramagnetic centers, thus increasing the average electron-nuclear distance of the observed carbon spins with longer polarization time. Longer polarization times therefore yield overall narrower resonances due to carbon spins with weaker hyperfine interactions contributing a larger fraction of the NMR signal (^{13}C T_1 = 448 seconds). However, the $\Delta\omega_{eDEC}/2\pi$ increases with lower polarization times because more of the observed carbons have stronger hyperfine interactions that are attenuated by electron decoupling.

As expected, the electron decoupling performance is optimal when the microwave frequency is centered on resonance with the electron spins (Figure 4.5b). Although unmodulated microwave irradiation directly on resonance with the electrons narrows the NMR linewidth by 7 Hz, microwave sweeps significantly improve the electron decoupling (Figure 4.5c). Triangular waveforms from an arbitrary waveform generator sweep the gyrotron voltage, and in turn the microwave frequency.

The dependence of the degree of electron decoupling on the microwave sweep width is shown in Figure 4.5c. Maximum electron decoupling is achieved with a sweep width of 130 MHz, but is nearly optimized with sweep widths between 90 and 150 MHz, which correspond to the EPR linewidth indicated in Figure 4.5b. Although a series of adiabatic inversions were attempted to produce electron decoupling, the electron nutation frequency was probably not sufficient to

produce full adiabatic inversions and further experimental and theoretical studies will be required to fully understand the mechanism of electron decoupling.

Figure 4.5d shows that the sweep time, τ_{sw}, during electron decoupling also affects the performance of electron decoupling. Sweep times shorter than 8 μs were not achievable with the current implementation of the microwave frequency agility circuit, resulting in reduced $\Delta\omega_{eDEC}/2\pi$ at the short sweep times attempted and shown in Figure 4.5d.

Note that DNP polarizing agents lead to less line-broadening if the radicals are sufficiently spatially separated from the nuclear spins of interest[31]. For example, DNP spectra acquired with CP exhibit a linewidth of 261 Hz compared to a linewidth of 228 Hz without any DNP polarizing agent. Furthermore, in cryogenic MAS experiments the NMR linewidth is typically dominated by structural and chemical shift heterogeneity which is frozen-out with reduced thermal energy[32,33]. Although some rigid crystalline samples exhibit linewidths similar to that achieved at room temperature[31,34], the typical loss of spectral resolution in cryogenic DNP experiments can best be overcome by recording NMR spectra at higher temperatures. Improving the resolution of DNP enhanced NMR is particularly important for resolving resonances of uniformly isotope-enriched proteins.

It should be noted that it is unlikely that the narrowing of the resonance is due to an interaction of the microwaves, nucleus, and rotations present in the sample, as the narrowing effect has only been observed on narrow line radicals such as the experiments with the Trityl Finland radical described here. No effect has been observed in broad line radicals such as nitroxides, which

have a spectral width of nearly 900 MHz in a 7 T magnetic field. Such an effect was a possibility due to the sidebands that arise during frequency modulation[35]. These sidebands can be many gigahertz from the center frequency of the chirps, putting some of the microwave power at frequencies corresponding to rotations within the sample.

4.4 Conclusion

Electron decoupling in conjunction with pulsed DNP methods could lead to substantially improved DNP performance at higher temperatures. With electron decoupling, stronger hyperfine couplings could be used to transfer polarization, leading to faster and more efficient transfers, even from electron spins with short relaxation times at room temperature. Without electron decoupling, stronger hyperfine couplings lead to extensive paramagnetic relaxation, and also cause a spin diffusion barrier which impedes the spread of the enhanced nuclear polarization away from the DNP polarizing agents[36]. Electron decoupling therefore has a promising role to play in extending DNP to higher temperatures, enabling the acquisition of higher resolution NMR spectra and measurements of molecular dynamics.

Electron decoupling could enable the direct polarization of nuclear spins of interest and eliminates the requirement for nuclear spin diffusion, allowing for the characterization of aprotic samples. By using aprotic samples with DNP polarizing agents, magnetization recovery delays between transients would only be limited by the electron longitudinal relaxation time.

Further work will be necessary to determine the mechanism behind electron decoupling. The goal of performing a series of microwave frequency chirps on the electron channel was to perform adiabatic inversions on the electrons for a broadband decoupling effect. The electron nutation frequency used was probably insufficient to perform adiabatic inversions, so the actual mechanism at work is currently unknown. Furthermore, more work will be needed to determine if all of the spins are being decoupled a little bit, or if a small number of carbon nuclei are being decoupled substantially.

In conclusion, electron decoupling in MAS DNP experiments reduces linewidths, lengthens transverse relaxation times, and increases the intensity of resonances in NMR spectroscopy. As microwave DNP technology continues to improve, the scope and performance of electron decoupling will expand to enable better decoupling on a wide range of DNP polarizing agents.

References

(1) Becerra, L. R.; Gerfen, G. J.; Temkin, R. J.; Singel, D. J.; Griffin, R. G. Dynamic Nuclear Polarization with a Cyclotron Resonance Maser at 5 T. *Phys. Rev. Lett.* **1993**, *71* (21), 3561–3564.

(2) Hall, D. A.; Maus, D. C.; Gerfen, G. J.; Inati, S. J.; Becerra, L. R.; Dahlquist, F. W.; Griffin, R. G. Polarization-Enhanced NMR Spectroscopy of Biomolecules in Frozen Solution. *Science (80-.).* **1997**, *276* (5314), 930–932.

(3) Kubicki, D. J.; Rossini, A. J.; Purea, A.; Zagdoun, A.; Ouari, O.; Tordo, P.; Engelke, F.; Lesage, A.; Emsley, L. Amplifying Dynamic Nuclear Polarization of Frozen Solutions by Incorporating Dielectric Particles. *J. Am. Chem. Soc.* **2014**, *136* (44), 15711–15718.

(4) Barnes, A. B.; De Paëpe, G.; van der Wel, P. C. A.; Hu, K. N.; Joo, C. G.; Bajaj, V. S.; Mak-Jurkauskas, M. L.; Sirigiri, J. R.; Herzfeld, J.; Temkin, R. J.; et al. High-Field Dynamic Nuclear Polarization for Solid and Solution Biological NMR. *Appl. Magn. Reson.* **2008**, *34* (3), 237–263.

(5) Mak-Jurkauskas, M. L.; Bajaj, V. S.; Hornstein, M. K.; Belenky, M.; Griffin, R. G.; Herzfeld, J. Energy Transformations Early in the Bacteriorhodopsin Photocycle Revealed by DNP-Enhanced Solid State NMR. *Proc. Natl. Acad. Sci. U. S. A.* **2008**, *105* (3), 883–888.

(6) Lange, S.; Franks, W. T.; Rajagopalan, N.; Döring, K.; Geiger, M. A.; Linden, A.; van Rossum, B.-J.; Kramer, G.; Bukau, B.; Oschkinat, H. Structural Analysis of a Signal Peptide inside the Ribosome Tunnel by DNP MAS NMR. *Sci. Adv.* **2016**, *2* (8), e1600379–e1600379.

(7) Frederick, K. K.; Michaelis, V. K.; Corzilius, B.; Ong, T. C.; Jacavone, A. C.; Griffin, R. G.; Lindquist, S. Sensitivity-Enhanced NMR Reveals Alterations in Protein Structure by Cellular Milieus. *Cell* **2015**, *163* (3), 620–628.

(8) Rossini, A. J.; Widdifield, C. M.; Zagdoun, A.; Lelli, M.; Schwarzwälder, M.; Copéret, C.; Lesage, A.; Emsley, L. Dynamic Nuclear Polarization Enhanced NMR Spectroscopy for Pharmaceutical Formulations. *J. Am. Chem. Soc.* **2014**, *136* (6), 2324–2334.

(9) Corzilius, B.; Andreas, L. B.; Smith, A. A.; Ni, Q. Z.; Griffin, R. G. Paramagnet Induced Signal Quenching in MAS–DNP Experiments in Frozen Homogeneous Solutions. *J. Magn. Reson.* **2014**, *240*, 113–123.

(10) Lange, S.; Linden, A. H.; Akbey, Ü.; Franks, W. T.; Loening, N. M.; van Rossum, B.-J.; Oschkinat, H. The Effect of Biradical Concentration on the Performance of DNP-MAS-

NMR. *J. Magn. Reson.* **2012**, *216*, 209–212.

(11) Mentink-Vigier, F.; Paul, S.; Lee, D.; Feintuch, A.; Hediger, S.; Vega, S.; De Paëpe, G. Nuclear Depolarization and Absolute Sensitivity in Magic-Angle Spinning Cross-Effect Dynamic Nuclear Polarization. *Phys. Chem. Chem. Phys.* **2015**, *17*, 21824–21836.

(12) Thurber, K. R.; Tycko, R. Perturbation of Nuclear Spin Polarizations in Solid State NMR of Nitroxide-Doped Samples by Magic-Angle Spinning without Microwaves. *J. Chem. Phys.* **2014**, *140* (18), 184201.

(13) Ernst, R. R. Nuclear Magnetic Double Resonance with an Incoherent Radio-Frequency Field. *J. Chem. Phys.* **1966**, *45*, 3845.

(14) Shaka, A. J.; Keeler, J.; Frenkiel, T.; Freeman, R. An Improved Sequence for Broadband Decoupling: WALTZ-16. *J. Magn. Reson.* **1983**, *52* (2), 335–338.

(15) Bennett, A. E.; Rienstra, C. M.; Auger, M.; Lakshmi, K. V.; Griffin, R. G. Heteronuclear Decoupling in Rotating Solids. *J. Chem. Phys.* **1995**, *103*, 6951.

(16) Schaefer, J.; Stejskal, E. O.; Buchdahl, R. High-Resolution Carbon-13 Nuclear Magnetic Resonance Study of Some Solid, Glassy Polymers. *Macromolecules* **1975**, *8* (3), 291–296.

(17) Jeschke, G.; Schweiger, A. Hyperfine Decoupling in Electron Spin Resonance. *J. Chem. Phys.* **1997**, *106* (24), 9979–9991.

(18) Siaw, T. A.; Wilson, B.; Jain, S.; Equibal, A.; Kaminker, I.; Han, S. Electron Spin Decoupled NMR by Using Clustered Electron Spins. In *Personal communication.*; 2017.

(19) Du, J.; Rong, X.; Zhao, N.; Wang, Y.; Yang, J.; Liu, R. B. Preserving Electron Spin Coherence in Solids by Optimal Dynamical Decoupling. *Nature* **2009**, *461* (7268), 1265–1268.

(20) Hoff, D. E. M.; Albert, B. J.; Saliba, E. P.; Scott, F. J.; Choi, E. J.; Mardini, M.; Barnes,

A. B. Frequency Swept Microwaves for Hyperfine Decoupling and Time Domain Dynamic Nuclear Polarization. *Solid State Nucl. Magn. Reson.* **2015**, *72*, 79–89.

(21) Barnes, A. B. Integrated EPR NMR with Frequency Agile Gyrotron. Patent App. #WO2015175507, 2015.

(22) Barnes, A. B.; Nanni, E. A.; Herzfeld, J.; Griffin, R. G.; Temkin, R. J. A 250 GHz Gyrotron with a 3 GHz Tuning Bandwidth for Dynamic Nuclear Polarization. *J. Magn. Reson.* **2012**, *221*, 147–153.

(23) Torrezan, A. C.; Han, S. T.; Mastovsky, I.; Shapiro, M. A.; Sirigiri, J. R.; Temkin, R. J.; Barnes, A. B.; Griffin, R. G. Continuous-Wave Operation of a Frequency-Tunable 460-GHz Second-Harmonic Gyrotron for Enhanced Nuclear Magnetic Resonance. *IEEE Trans. Plasma Sci.* **2010**, *38* (6 PART 1), 1150–1159.

(24) Matsuki, Y.; Idehara, T.; Fukazawa, J.; Fujiwara, T. Advanced Instrumentation for DNP-Enhanced MAS NMR for Higher Magnetic Fields and Lower Temperatures. *J. Magn. Reson.* **2016**, *264*, 107–115.

(25) Yoon, D.; Soundararajan, M.; Cuanillon, P.; Braunmueller, F.; Alberti, S.; Ansermet, J. P. Dynamic Nuclear Polarization by Frequency Modulation of a Tunable Gyrotron of 260 GHz. *J. Magn. Reson.* **2016**, *262*, 62–67.

(26) Afeworki, M.; Vega, S.; Schaefer, J. Direct Electron-to-Carbon Polarization Transfer in Homgeneously-Doped Polycarbonates. *Macromolecules* **1992**, *25*, 4100–4106.

(27) Can, T. V.; Walish, J. J.; Swager, T. M.; Griffin, R. G. Time Domain DNP with the NOVEL Sequence. *J. Chem. Phys.* **2015**, *143* (5), 54201.

(28) Pines, A.; Rhim, W. K.; Waugh, J. S. Homogeneous and Inhomogeneous Nuclear Spin Echoes in Solids. *J. Magn. Reson.* **1972**, *6* (4), 457–465.

(29) Carver, T. R.; Slichter, C. P. Experimental Verification of the Overhauser Nuclear Polarization Effect. *Phys. Rev.* **1956**, *102* (4), 975–980.

(30) Massiot, D.; Fayon, F.; Capron, M.; King, I.; Calvé, S. Le; Alonso, B.; Durand, J.-O.; Bujoli, B.; Gan, Z.; Hoatson, G. Modelling One- and Two-Dimensional Solid State NMR Spectra. *Magn. Reson. Chem.* **2002**, *40*, 70–76.

(31) Barnes, A. B.; Corzilius, B.; Mak-Jurkauskas, M. L.; Andreas, L. B.; Bajaj, V. S.; Matsuki, Y.; Belenky, M. L.; Lugtenburg, J.; Sirigiri, J. R.; Temkin, R. J.; et al. Resolution and Polarization Distribution in Cryogenic DNP/MAS Experiments. *Phys. Chem. Chem. Phys.* **2010**, *12* (22), 5861–5867.

(32) Siemer, A. B.; Huang, K. Y.; McDermott, A. E. Protein Linewidth and Solvent Dynamics in Frozen Solution NMR. *PLoS One* **2012**, *7* (10).

(33) Linden, A. H.; Franks, W. T.; Akbey, Ü.; Lange, S.; Van Rossum, B. J.; Oschkinat, H. Cryogenic Temperature Effects and Resolution upon Slow Cooling of Protein Preparations in Solid State NMR. *J. Biomol. NMR* **2011**, *51* (3), 283–292.

(34) Lee, D.; Bouleau, E.; Saint-Bonnet, P.; Hediger, S.; De Paëpe, G. Ultra-Low Temperature MAS-DNP. *J. Magn. Reson.* **2016**, *264*, 116–124.

(35) Seely, S. *McGraw-Hill Electrical and Electrinic Engineering Series: Radio Electronics*; The Maple Press Company: York, PA, 1956.

(36) Wolfe, J. P. Direct Observation of a Nuclear Spin Diffusion Barrier. *Phys. Rev. Lett.* **1973**, *31* (15), 907–910.

Chapter 5: Electron Decoupling with Cross Polarization and Dynamic Nuclear Polarization Below 6 K

Forward

This paper was adapted from "Electron Decoupling with Cross Polarization and Dynamic Nuclear Polarization Below 6 K" by Edward P. Saliba*, Erika L. Sesti*, Nicholas Alaniva, and Alexander B. Barnes and was the cover article for the October, 2018 issue of the Journal of Magnetic Resonance. It builds on the work on electron decoupling presented in the previous chapter. In the first paper on electron decoupling DNP was achieved with direct polarization of the ^{13}C atoms of urea from the electrons of the Trityl Finland radical. A disadvantage of performing the experiment this way, however, is the long T_{1DNP} of the carbons, which was measured to be 448 seconds. A superior way of performing the experiment with currently available continuous wave DNP methods is to first transfer the polarization from the electrons to the protons in the sample. Due to their abundance and large gyromagnetic ratios, spin diffusion through the protons is orders of magnitude faster than the carbons, leading to substantially shorter T_{1DNP}'s. The vast majority of solid state NMR experiments performed today are performed with cross polarization (CP), and so the work described here is highly pertinent to the field. Furthermore, this paper describes the first MAS experiments performed below 6 K, which will make future experiments tractable that would otherwise be prohibitively long. Citation: Sesti, E. L.* .; Saliba, E. P*. .; Alaniva, N.; Barnes, A. B. Electron Decoupling with Cross Polarization and Dynamic Nuclear Polarization below 6 K. *J. Magn. Reson.* 2018, *295*, 1–5.

Abstract

Dynamic nuclear polarization (DNP) can improve nuclear magnetic resonance (NMR) sensitivity by orders of magnitude. Polarizing agents containing unpaired electrons required for DNP can broaden nuclear resonances in the presence of appreciable hyperfine couplings. This chapter presents the first cross polarization experiments implemented with electron decoupling, which attenuates detrimental hyperfine couplings. Magic angle spinning (MAS) DNP experiments below 6 K are also presented, producing unprecedented nuclear spin polarization in rotating solids. ^{13}C correlation spectra were collected with MAS DNP below 6 K for the first time. Longitudinal magnetization recovery times with MAS DNP ($T_{1DNP, 1H}$) of urea in a frozen glassy matrix below 6 K were measured for both the solid effect and the cross effect. Trityl radicals exhibit a T_{1DNP} (^{1}H) of 18.7 s and the T_{1DNP} (^{1}H) of samples doped with 20 mM AMUPol is only 1.3 s. MAS below 6 K with DNP and electron decoupling is an effective strategy to increase NMR signal-to-noise ratios per transient while retaining short recovery periods.

5.1 Introduction

Solid-state nuclear magnetic resonance (NMR) spectroscopy is a powerful tool for studying a wide variety of molecular architectures[1–3]. When NMR is employed in conjunction with magic angle spinning (MAS), long spin coherence lifetimes deliver spectral resolution sufficient to interrogate structure at atomic resolution. Internal magnetic interactions, such as isotropic scalar couplings and anisotropic dipolar couplings, allow for the determination of molecular connectivities and three-dimensional structures. MAS NMR also enables molecular structural characterization within endogenous and heterogeneous environments relevant to biomedical and

materials science applications. However, MAS NMR typically suffers from low signal-to-noise ratios.

Poor signal-to-noise in NMR primarily arises from the small polarization of nuclear spin states at thermal equilibrium. Dynamic nuclear polarization (DNP) is one technique for biasing the polarization of spins of interest well beyond what is achievable thermally, theoretically leading to sensitivities orders of magnitudes higher[4,5]. When performing DNP, a millimolar concentration of a stable exogenous radical is typically doped into the sample. Upon irradiation of the sample with microwaves whose frequencies fulfill DNP matching conditions, the large Boltzmann polarization of the radical electrons can be transferred to the nuclei, with a theoretical maximum gain in polarization equal to the ratio of magnetic moments in the high temperature limit $\left(\frac{P_e}{P_{^1H}} \approx \left|\frac{\gamma_e}{\gamma_{^1H}}\right| = 658 \text{ for } h\nu_e \ll k_B T\right)$[6–8].

Reducing the thermal energy of the sample is another method of increasing spin polarization. MAS DNP is commonly performed at 100 K, but experiments at 25 K, at which temperature spin polarizations are $(298\ K)/(25\ K) = 12$-times larger in magnitude than at room temperature, have recently been demonstrated[9–12]. Spin polarization is further increased by cooling the sample to below 6 K. The associated NMR sensitivity gains achievable with cryogenic DNP below 6 K result in much shorter signal averaging times.

The hyperfine couplings mediating DNP transfers can, however, dramatically shorten nuclear spin relaxation and impair spectral resolution[9,11,13–18]. Hyperfine couplings can be attenuated with a train of chirped microwave pulses applied during the NMR free induction decay (FID)[19].

These initial electron decoupling experiments were performed by directly transferring the polarization of the electrons to ^{13}C nuclei. The T_{1DNP} of the carbon nuclei leads to long magnetization recovery periods to maximize the signal-to-noise ratio per unit time. Signal averaging can be accelerated by first polarizing protons through DNP and then relying on proton spin diffusion to distribute the enhanced polarization throughout the sample. DNP to protons followed by cross polarization to carbon nuclei therefore dramatically improves signal-to-noise per unit time. Additionally, proton-proton spin diffusion allows for hyperpolarization of carbons distant from the broadening hyperfine interactions of the electrons, leading to further improvements in spectral resolution[20].

Here, electron decoupling in rotating solids in conjunction with cross polarization is demonstrated for the first time. Electron decoupling with cross polarization below 6 K and at 90 K is recorded. Furthermore, short polarization build-up times with cryogenic MAS DNP below 6 K are observed.

5.2 Experimental Methods

A custom-built, 4-channel, 3.2 mm MAS, transmission-line NMR probe with a Redstone spectrometer (Tecmag, Houston, TX) was used to record all data. Larmor frequencies for ^{1}H and ^{13}C were 300.184 MHz and 75.495 MHz, respectively. All spectra were recorded as rotor-synchronized, echo-detected, cross-polarization MAS (CPMAS) experiments. The Hartmann-Hahn condition was ν_{1H} = 50 kHz and ν_{13C} = 52 kHz with a contact time of 1 ms. For $\pi/2$ pulses and two-pulse phase-modulated (TPPM) decoupling on ^{1}H, a nutation frequency of ν_{1H} = 90 kHz was used. The ^{13}C refocusing pulse had a nutation frequency of ν_{13C} = 100 kHz. To destroy any

residual polarization, saturation trains on both ^{1}H and ^{13}C were employed before a DNP polarization time (τ_{pol}). Polarization build-up times (T_{1DNP}) were recorded using a saturation recovery sequence. Typical spinning frequencies were 5000 Hz but varied in each experiment. Experimental parameters corresponding to each experiment are shown in Table 5.1 below:

Sample	Radical	Experiment	DNP/ no DNP	Transients	ν_{rot} (kHz)	ν_{rot} Stability (+/- Hz)	τ_{pol} (s)
urea	20 mM AMUPol	Enhancement	DNP	1	4.4	200	3
urea	20 mM AMUPol	Enhancement	no DNP	1	4.4	200	3
urea	20 mM AMUPol	T_{1DNP}	DNP	1	4.4	200	-
urea	40 mM trityl	Enhancement	DNP	4	4.5	10	3
urea	40 mM trityl	Enhancement	no DNP	16	4.5	10	3
urea	40 mM trityl	T_{1DNP}	DNP	1	4.9	200	-
urea	20 mM AMUPol	Power Dependence (0.23 W)	DNP	1	4.4	100	3
urea	40 mM trityl	Power Dependence (0.23 W)	DNP	1	4.5	10	3
urea	40 mM trityl	^{13}C Hahn echo – eDEC 90 K	DNP	12	4.0	20	7
urea	40 mM trityl	^{13}C Hahn echo– no eDEC 90 K	DNP	12	4.0	20	7
urea	40 mM trityl	CP – eDEC 90 K	DNP	4	3.9	20	3
urea	40 mM trityl	CP – no eDEC 90 K	DNP	4	3.9	20	3
urea	40 mM trityl	^{13}C – eDEC 6 K	DNP	1	4.9	200	7
urea	40 mM trityl	^{13}C – no eDEC 6 K	DNP	1	4.9	200	7
urea	40 mM trityl	CP – eDEC 6 K	DNP	1	4.5	10	3
urea	40 mM trityl	CP - no eDEC 6 K	DNP	1	4.5	10	3
urea	no radical	CP – 90 K	no DNP	128	4.0	20	7
urea	no radical	CP – 6 K	no DNP	1	5.1	100	30
L-proline	40 mM Trityl	eDEC	DNP	4	5.0	150	3
L-proline	40 mM Trityl	Enhancement	DNP	4	5.0	150	3
L-proline	40 mM Trityl	Enhancement	no DNP	16	5.0	150	3

Table 5.1: Experimental parameters used in the experiments described here.

All spectra were referenced to adamantane at 193 K, and that reference was used to assign chemical shift values at 6 K. Enhancements were found by dividing the area of the spectra taken

with microwaves on by the area of the spectra obtained with microwaves off. The areas were determined by fitting the peaks in DMfit[21]. Microwave irradiation was produced by a custom-built frequency-agile gyrotron with an output power of 15 W[19,22], corresponding to approximately 5 W (ν_{1s} = 380 kHz) at the sample due to loss within the waveguide. The microwave power was attenuated with a 3% transmittance attenuator (Tydex LLC. St. Petersburg, Russia) placed in the waveguide. For low power experiments, 0.70 W was measured out of the attenuator with an estimated 0.23 W (ν_{1s} = 81 kHz) at the sample. Microwave powers were measured using a calorimeter. The microwave irradiation frequency was 197.674 GHz for AMUPol and 197.950 GHz for trityl. For electron decoupling (eDEC) experiments, the irradiation frequency during τ_{pol} was at the zero-quantum solid effect condition for ^{1}H (197.950 GHz). During the acquisition period, chirped pulses were applied around the EPR resonance condition (197.640 GHz) as shown in Figure 5.1a. The chirped pulses were 13.75 μs in length and 87 MHz wide in frequency[19]. Microwave chirps were produced using the spectrometer's arbitrary waveform generator and were amplified by a linear amplifier (Trek Inc., Lockport, NY) attached to the gyrotron[22].

Two-dimensional spectra were obtained on L-proline using the proton-driven spin diffusion (PDSD) NMR sequence[23] and the STATES method[24]. All microwave and RF frequencies were the same as for CPMAS experiments. For the PDSD spectrum taken below 6 K, a 30 μs dwell time was used in both the indirect and direct dimensions. 64 points were collected in the indirect dimension (t1) and 256 points in the direct dimension. Four transients were recorded with a τ_{pol} = 1 s. For the PDSD spectrum at 90 K, 32 transients were acquired in each slice with a polarization time of 3 s. 256 points were collected in the direct dimension and 128 in the indirect dimension.

For all PDSD experiments, the dwell time used in both dimensions was 30 μs, and both dimensions were zero filled to 1024 points. The mixing time was 5 ms, and the spinning frequency was 5,500 Hz. The PDSD pulse sequence is shown in Figure 5.1b. The microwave frequency was shifted off of the DNP condition to the nominal output frequency of the gyrotron at 197.839 GHz following the z-filter.

Figure 5.1c shows the input waveform on the arbitrary waveform generator used to modulate the output frequency of the gyrotron (black) and $0.001 \times$ the actual waveform output by the amplifier that it was fed into (red). The voltage modulation is similar to that presented in the precious chapter, but with some important differences. Most noticeably, the voltage jump from the DNP condition at 197.950 GHz to the electron resonance frequency at 197.640 GHz is much larger in the CP case than in the direct polarization case. This is due to the fact that the solid effect condition for protons is much further away from the electron resonance frequency than the carbon one is. Another difference between the two cases arises for the same reason. The gyrotron requires an anode voltage larger than the maximum 3.3 kV that the arbitrary waveform generator can pull in one direction. For this reason, the nominal output frequency of the gyrotron needs to be set in between the two conditions (it was set to 197.839 GHz for these experiments), rather than at the DNP condition.

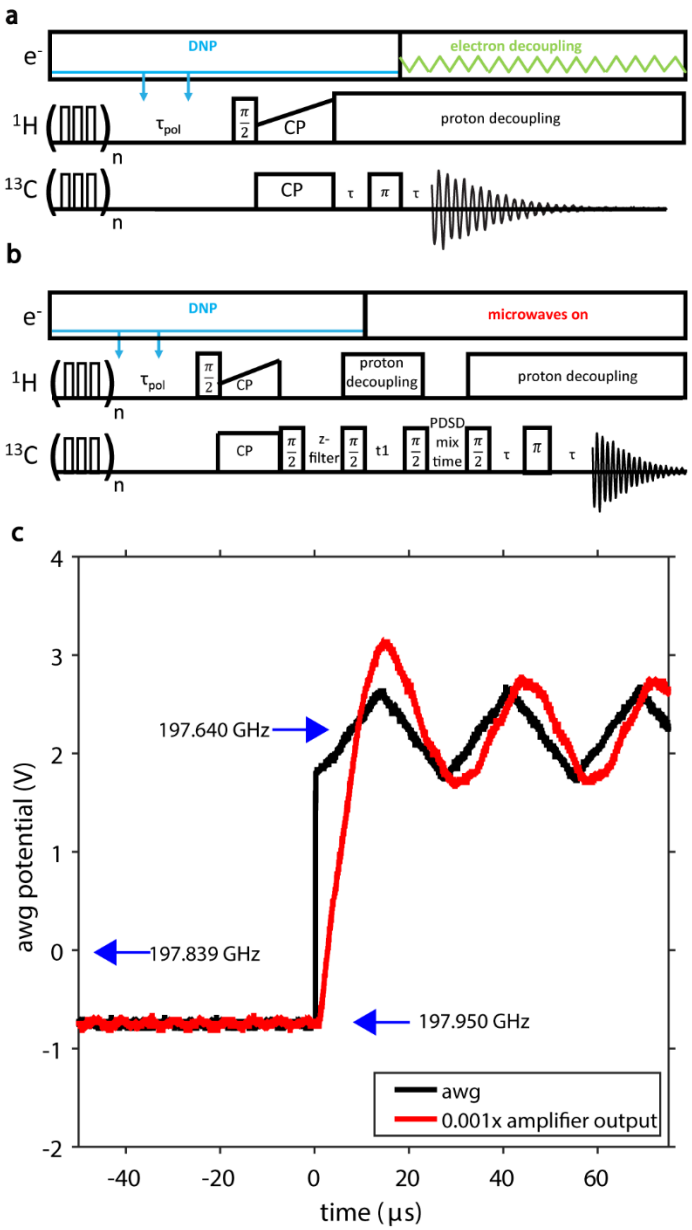

Figure 5.1: (a) Cross-polarization magic angle spinning (CPMAS) with electron decoupling. (b) Proton-driven spin diffusion (PDSD) CPMAS. (c) The waveform input into an arbitrary waveform generator to produce the voltage sweeps to generate the frequency chirps on the gyrotron (black) and 0.001 × the voltage modulation actually output by the amplifier (red).

Sample temperatures below 6 K were achieved with liquid helium as variable-temperature (VT) fluid directed at the center of the spinning rotor. Ultra-high-purity helium gas at 80 K was used for MAS bearing and drive gases. The sample temperature was monitored at the interface of the

VT outlet and NMR stator with a Cernox temperature sensor (Lake Shore Cyrotronics Inc., Westerville, OH). The temperature at this point was regarded as the sample temperature as demonstrated previously[25]. A Lakeshore temperature controller was used to monitor the temperature of the sample, the incoming transfer lines, and the exhaust line.

Three standard samples were prepared for this set of experiments. The first was a 4 M [U-^{13}C,^{15}N] urea sample (Cambridge Isotopes, Tewksbury, MA). Urea was dissolved in a solution of 60% d8-glycerol, 30% D_2O, and 10% H_2O. AMUPol (CortecNet Corp., Brooklyn, NY) was added to bring its concentration to 20 mM. The second sample was made by preparing a 4 M [U-^{13}C,^{15}N] urea sample in 60% d8-glycerol, 30% D_2O, and 10% H_2O. Trityl (Finland radical; Oxford Instruments, Abingdon. UK) was added to give a 40 mM radical concentration. The final sample consisted of 4 M [U-^{13}C,^{15}N] L-proline (Cambridge Isotopes) dissolved in 60% d8-glycerol, 30% D_2O, and 10% H_2O. This sample contained trityl at 40 mM. High concentrations (40 mM) of trityl were employed to study the effect of electron decoupling. Approximately 36 µL of each sample was added to separate 3.2 mm zirconia rotors.

5.3 Results

5.3.1 High-Resolution DNP-NMR Below 6 K in Model Systems

To investigate DNP-enhanced NMR spectroscopy below 6 K with a frequency-agile gyrotron, a series of experiments were performed using nitroxide biradicals or tertiary carbon monoradicals as polarizing agents on [U-^{13}C,^{15}N] urea and [U-^{13}C,^{15}N] L-proline within a frozen glassy matrix. Biradicals such as AMUPol, using the cross-effect mechanism, yielded the highest signal enhancements. A 282-fold signal enhancement of urea with 20 mM AMUPol was recorded under MAS with a sample temperature below 6 K (Figure 5.2a). It should be noted that this is not a true

enhancement value, as samples with AMUPol are susceptible to depolarization[9]. Due to combined DNP enhancement and improved thermal Boltzmann polarization, only a single transient was required to achieve an excellent signal-to-noise ratio. Remarkably, the polarization build-up time (T_{1DNP}, ^1H) was only 1.3 s (Figure 5.2c), making the optimal recycle delay to maximize signal-to-noise per unit time only 1.6 s ($1.26*T_1$)[26]. Polarizing agents also yield short polarization build-up times at 90 K (T_{1DNP} = 1.3 s)[13,27,28], but here we demonstrate similar build-up times below 6 K. While T_{1DNP} time constants in static samples at 1.2 K can be several minutes to hours[29,30], these short recovery time constants are comparable to those observed at room temperature.[31] Therefore, MAS DNP below 6 K delivers unprecedented NMR sensitivity per unit time.

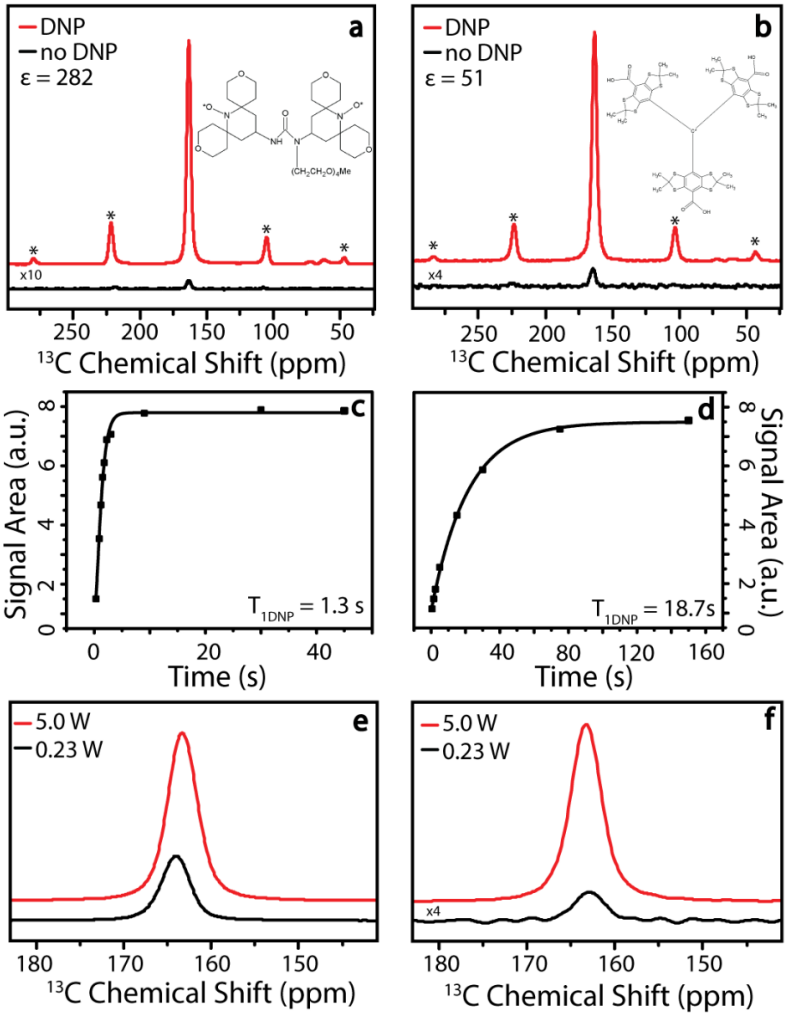

Figure 5.2. DNP CPMAS NMR spectra below 6 K on model systems. (a), (b) Enhancement spectra of urea with AMUPol and trityl, respectively. Spectra in black represent no microwave irradiation while spectra in red are with microwave irradiation. T_{1DNP} of ^{1}H for urea with AMUPol (c) and trityl (d). (e), (f) Microwave power dependence on urea with AMUPol and trityl, respectively. 5.0 W of microwave power incident to the sample is shown in red and 0.23 W of microwave power is shown in black. * denote spinning side bands.

The enhancement in Figure 5.2b demonstrates the solid effect using the tertiary monoradical, trityl, below 6 K. In contrast to the cross effect, the solid effect enhancement is polarization time dependent due to the effect of microwave intensity on magnetization buildup during DNP[16,17,32,33]. Accordingly, a solid effect DNP enhancement of 51-fold with a polarization time (τ_{pol}) of 3 s (Figure 5.2b) and 32-fold with a τ_{pol} of 30 s was observed. The T_{1DNP} (^{1}H) for urea

with trityl was 18.7 s below 6 K (Figure 5.2d). Shorter longitudinal recovery times (in this case, τ_{pol}) with solid effect DNP will be accessible with higher microwave intensity. DNP provided a signal increase of 51-fold with a further improvement of 41-fold due to Boltzmann spin polarization at 6 K compared to 298 K. At these temperatures, the polarization of the electrons at ~198 GHz has moved out of the high temperature approximation commonly employed in magnetic resonance calculations and the full Boltzmann expression, $P_e = \tanh\left(\frac{h\nu_e}{2k_BT}\right)$, must be used (Figure 5.3). Therefore, MAS DNP below 6 K can enhance NMR signals by over 2,000-fold over room temperature experiments.

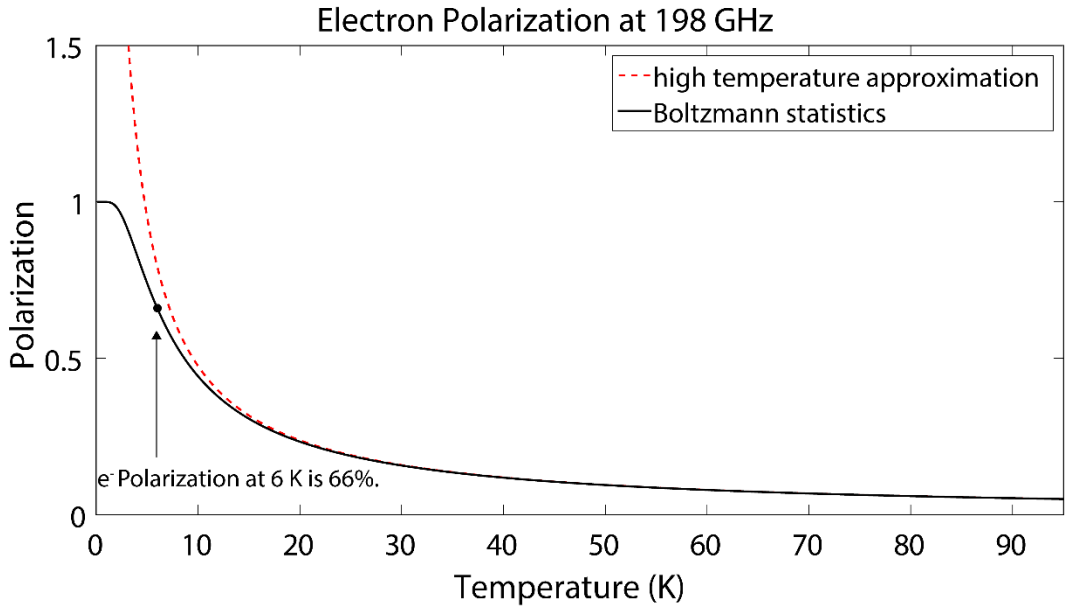

Figure 5.3: Plots of the $\frac{h\nu_0}{2k_BT}$ dependence of the electron polarization commonly used in the high temperature limit (red) and the full Boltzmann expression for a spin $\frac{1}{2}$ particle, $\tanh\left(\frac{h\nu_0}{2k_BT}\right)$ (black). At 6 K the two have begun to non-negligibly deviate from one another. This deviation becomes even larger as the temperature is cooled further and the polarization of the electrons begins to approach unity. Here $h = 6.626 \times 10^{-34} Js$, $k_B = 1.38 \times 10^{-23} \frac{J}{K}$, $\nu_0 = 198 \times 10^9\ Hz$, and T is the temperature in Kelvin. The point on the Boltzmann polarization curve marks the polarization at 6 K where it is equal to 66%.

Significantly higher DNP enhancements were obtained with an electron nutation frequency (ν_{1s}) of 380 kHz (5.0 W incident power)[34] compared to $\nu_{1s} \approx 83$ kHz (0.23 W incident power). DNP enhancement was dependent on microwave power with trityl monoradicals using the solid effect and also with nitroxide biradicals polarizing through the cross effect (Figure 5.2e, f). 2-fold and 26-fold gains in DNP signal enhancement were obtained for AMUPol and trityl, respectively, using 5.0 W versus 0.23 W.

Therefore, high-power microwave sources such as the gyrotron oscillator employed here improve DNP enhancements not only at higher temperatures (>80 K)[35] but also in MAS DNP below 6 K. Higher microwave powers also efficiently polarize nuclear spins with direct hyperfine couplings, resulting in a concomitant larger observed hyperfine shift (Figure 5.2e)[25,36,37].

5.3.2 Electron Decoupling with Cross Polarization

Previously, electron decoupling (eDEC) has been performed with direct electron-to-carbon DNP transfers on samples of urea with trityl at 90 K[19]. Note, moderate spinning frequencies of 4 kHz result in larger electron decoupling effects compared to higher spinning frequencies. Here we show electron decoupling of DNP-enhanced NMR spectra recorded with MAS below 6 K, also employing cross polarization (CP). Figures 5.3a and 5.3b illustrate the first CPMAS electron decoupling experiments with urea and L-proline, respectively. Polarization transfer from electron to proton spins, followed by ^{1}H-^{1}H spin diffusion, results is much faster longitudinal magnetization recovery over direct ^{13}C polarization. Following a subsequent polarization transfer from protons to carbons via CP, the ^{13}C free induction decay (FID) is recorded under both proton

and electron decoupling (Figure 5.1a). Electron decoupling on urea and L-proline improved signal intensity (5 ± 2% area increase) and reduced linewidths (11 ± 2 Hz narrowing) on average (Figure 5.4a and 5.4b), with an additional attenuation of the hyperfine shift resulting from the DNP polarizing agent. This is the first demonstration of electron decoupling attenuating an observable hyperfine shift in rotating solids.

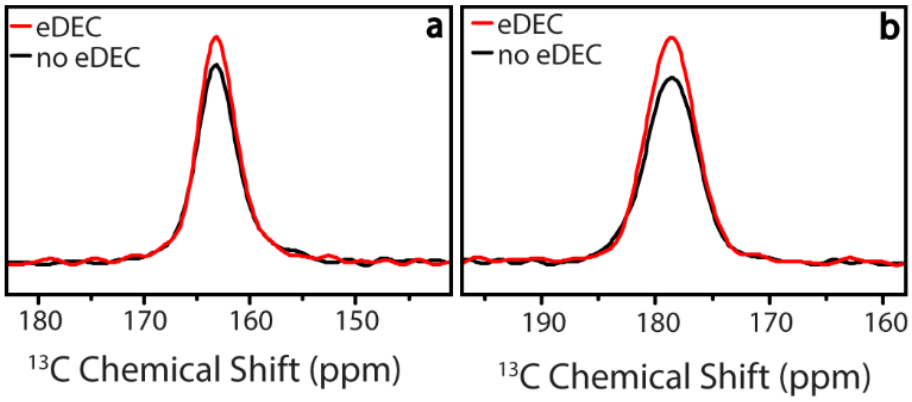

Figure 5.4: Electron decoupling with cross polarization. (a) CP-DNP spectra of urea with trityl. (b) Carbonyl region from the ^{13}C spectrum of L-proline with trityl. Black spectra were recorded with no electron decoupling, while red spectra were recorded with electron decoupling.

Detrimental hyperfine interactions are reduced using proton spin diffusion to relay enhanced polarization far from the radicals using CP. At 90 K, CP with electron decoupling on a sample of urea narrowed the ^{13}C resonance by 10 Hz. The overall linewidth of the resonance utilizing CP with electron decoupling approached the linewidth observed with no radical present (Table 5.1). ^{13}C direct DNP followed by electron decoupling narrowed the resonance to 306 Hz, while CP with electron decoupling gave a linewidth of 250 Hz. When electron decoupling was performed below 6 K, a similar trend was observed (Table 5.2). Note that, overall, there was more broadening from the radicals below 6 K compared to 90 K, suggesting that further DNP-NMR spectra improvements can be realized with improved electron decoupling.

Experiment	90 K linewidth (Hz)	Below 6 K linewidth (Hz)
^{13}C direct - no eDEC	339 ± 2	349 ± 2
^{13}C direct - eDEC	306 ± 2	328 ± 6
CP – no eDEC	259 ± 1	322 ± 6
CP – eDEC	250 ± 2	310 ± 6
CP – no radical present	228	225

Table 5.2: Effect of radicals and electron decoupling on linewidths of [U-^{13}C, ^{15}N] urea with and without trityl. Electron decoupling (eDEC) coupled with cross polarization (CP) results in ^{13}C linewidths approaching those without any radical present.

5.3.3 Electron Decoupling with Cross Polarization

Carbon-carbon correlation spectra were recorded on [U-^{13}C, ^{15}N] L-proline with trityl below 6 K to demonstrate the time savings afforded by DNP at this temperature in multidimensional experiments. The proton-driven spin diffusion (PDSD) pulse sequence is shown in Figure 5.1b. The total experimental time of the PDSD experiment performed below 6 K was 24 minutes (Figure 5.5a). For comparison, a PDSD at 90 K is shown containing a similar signal-to-noise ratio (Figure 5.5b); however, this experiment took 16 hours.

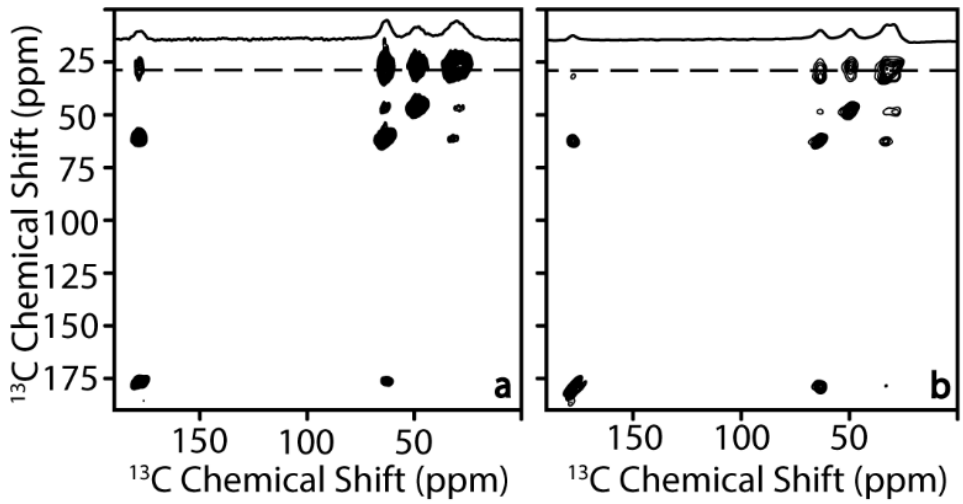

Figure 5.5. PDSD taken on [U-^{13}C, ^{15}N] L-proline with trityl below 6 K **(a)** and at 90 K **(b)**. The 1D spectrum at the top of each figure is the slice of the 2D spectrum indicated by the dashed line. The total experiment time was 16 hours for the spectrum recorded at 90 K, while the experiment at 6 K required only 24 minutes.

5.4 Conclusions

The radicals introduced into the sample for DNP can lead to broadening due to hyperfine interactions. Electron decoupling provides a means to mitigate these unwanted interactions. Performing electron decoupling with cross polarization has the dual advantages of faster recovery times and narrower resonances compared to direct polarization. One-dimensional NMR experiments employing CPMAS and electron decoupling on biomolecules frozen in a glassy matrix resulted in 11 Hz narrowing and a 5% increase in signal area.

The already sizeable enhancements afforded by DNP can be further improved by cooling the sample to below 6 K. DNP below 6 K leads to a 51-fold solid effect enhancement and a 282-fold cross-effect enhancement. The longitudinal magnetization recovery times remain short at these temperatures, allowing for large enhancements and quick recovery times. MAS below 6 K

combined with high-power frequency-agile microwave sources also provides a promising avenue for the implementation of pulsed DNP[38–41].

References

(1) Rossini, A. J.; Widdifield, C. M.; Zagdoun, A.; Lelli, M.; Schwarzwälder, M.; Copéret, C.; Lesage, A.; Emsley, L. Dynamic Nuclear Polarization Enhanced NMR Spectroscopy for Pharmaceutical Formulations. *J. Am. Chem. Soc.* **2014**, *136* (6), 2324–2334.

(2) Hayes, S.; Van Wüllen, L.; Eckert, H.; Even, W. R.; Crocker, R. W.; Zhang, Z. Solid-State NMR Strategies for the Structural Investigation of Carbon-Based Anode Materials. *Chem. Mater.* **1997**, *9* (4), 901–911.

(3) Mak-Jurkauskas, M. L.; Bajaj, V. S.; Hornstein, M. K.; Belenky, M.; Griffin, R. G.; Herzfeld, J. Energy Transformations Early in the Bacteriorhodopsin Photocycle Revealed by DNP-Enhanced Solid State NMR. *Proc. Natl. Acad. Sci. U. S. A.* **2008**, *105* (3), 883–888.

(4) Hall, D. A.; Maus, D. C.; Gerfen, G. J.; Inati, S. J.; Becerra, L. R.; Dahlquist, F. W.; Griffin, R. G. Polarization-Enhanced NMR Spectroscopy of Biomolecules in Frozen Solution. *Science (80-.).* **1997**, *276* (5314), 930–932.

(5) Lange, S.; Franks, W. T.; Rajagopalan, N.; Döring, K.; Geiger, M. A.; Linden, A.; van Rossum, B.-J.; Kramer, G.; Bukau, B.; Oschkinat, H. Structural Analysis of a Signal Peptide inside the Ribosome Tunnel by DNP MAS NMR. *Sci. Adv.* **2016**, *2* (8), e1600379.

(6) Carver, T. R.; Slichter, C. P. Polarization of Nuclear Spins in Metals. *Phys. Rev.* **1953**, *92* (1), 212–213.

(7) Kubicki, D. J.; Rossini, A. J.; Purea, A.; Zagdoun, A.; Ouari, O.; Tordo, P.; Engelke, F.; Lesage, A.; Emsley, L. Amplifying Dynamic Nuclear Polarization of Frozen Solutions by Incorporating Dielectric Particles. *J. Am. Chem. Soc.* **2014**, *136* (44), 15711–15718.

(8) Lilly Thankamony, A. S.; Wittmann, J. J.; Kaushik, M.; Corzilius, B. Dynamic Nuclear Polarization for Sensitivity Enhancement in Modern Solid-State NMR. *Prog. Nucl. Magn. Reson. Spectrosc.* **2017**, *102–103*, 120–195.

(9) Thurber, K. R.; Tycko, R. Perturbation of Nuclear Spin Polarizations in Solid State NMR of Nitroxide-Doped Samples by Magic-Angle Spinning without Microwaves. *J. Chem. Phys.* **2014**, *140* (18).

(10) Thurber, K.; Tycko, R. Low-Temperature Dynamic Nuclear Polarization with Helium-Cooled Samples and Nitrogen-Driven Magic-Angle Spinning. *J. Magn. Reson.* **2016**, *264*, 99–106.

(11) Mentink-Vigier, F.; Paul, S.; Lee, D.; Feintuch, A.; Hediger, S.; Vega, S.; De Paëpe, G. Nuclear Depolarization and Absolute Sensitivity in Magic-Angle Spinning Cross Effect Dynamic Nuclear Polarization. *Phys. Chem. Chem. Phys.* **2015**, *17* (34), 21824–21836.

(12) Lee, D.; Bouleau, E.; Saint-Bonnet, P.; Hediger, S.; De Paëpe, G. Ultra-Low Temperature MAS-DNP. *J. Magn. Reson.* **2016**, *264*, 116–124.

(13) Lange, S.; Linden, A. H.; Akbey, Ü.; Trent Franks, W.; Loening, N. M.; Rossum, B. J. Van; Oschkinat, H. The Effect of Biradical Concentration on the Performance of DNP-MAS-NMR. *J. Magn. Reson.* **2012**, *216*, 209–212.

(14) Corzilius, B.; Andreas, L. B.; Smith, A. A.; Ni, Q. Z.; Griffin, R. G. Paramagnet Induced Signal Quenching in MAS-DNP Experiments in Frozen Homogeneous Solutions. *J. Magn. Reson.* **2014**, *240*, 113–123.

(15) Hovav, Y.; Feintuch, A.; Vega, S. Theoretical Aspects of Dynamic Nuclear Polarization in the Solid State - The Cross Effect. *J. Magn. Reson.* **2012**, *214*, 29–41.

(16) Thurber, K. R.; Tycko, R. Theory for Cross Effect Dynamic Nuclear Polarization under Magic-Angle Spinning in Solid State Nuclear Magnetic Resonance: The Importance of Level Crossings. *J. Chem. Phys.* **2012**, *137* (8).

(17) Mentink-Vigier, F.; Akbey, Ü.; Oschkinat, H.; Vega, S.; Feintuch, A. Theoretical Aspects of Magic Angle Spinning - Dynamic Nuclear Polarization. *J. Magn. Reson.* **2015**, *258*, 102–120.

(18) Andreas, L. B.; Barnes, A. B.; Corzilius, B.; Chou, J. J.; Miller, E. A.; Caporini, M.; Rosay, M.; Griffin, R. G. Dynamic Nuclear Polarization Study of Inhibitor Binding to the M2(18-60) Proton Transporter from Influenza A. *Biochemistry* **2013**, *52* (16), 2774–2782.

(19) Saliba, E. P.; Sesti, E. L.; Scott, F. J.; Albert, B. J.; Choi, E. J.; Alaniva, N.; Gao, C.; Barnes, A. B. Electron Decoupling with Dynamic Nuclear Polarization in Rotating Solids. *J. Am. Chem. Soc.* **2017**, *139* (18), 6310–6313.

(20) Becerra, L. R.; Gerfen, G. J.; Temkin, R. J.; Singel, D. J.; Griffin, R. G. Dynamic Nuclear Polarization with a Cyclotron Resonance Maser at 5 T. *Phys. Rev. Lett.* **1993**, *71* (21), 3561–3564.

(21) Massiot, D.; Fayon, F.; Capron, M.; King, I.; Le Calvé, S.; Alonso, B.; Durand, J. O.; Bujoli, B.; Gan, Z.; Hoatson, G. Modelling One- and Two-Dimensional Solid-State NMR Spectra. *Magn. Reson. Chem.* **2002**, *40* (1), 70–76.

(22) Scott, F. J.; Saliba, E. P.; Albert, B. J.; Alaniva, N.; Sesti, E. L.; Gao, C.; Golota, N. C.; Choi, E. J.; Jagtap, A. P.; Wittmann, J. J.; et al. Frequency-Agile Gyrotron for Electron Decoupling and Pulsed Dynamic Nuclear Polarization. *J. Magn. Reson.* **2018**, *289*, 45–54.

(23) Szevereny, N. M.; Sullivan, M. J.; Maciel, G. E. Observation of Spin Exchange by Two-Dimensional Fourier Transfrom 13C Cross Polarization-Magic-Angle Spinning. *J. Magn. Reson.* **1982**, *47*, 462–475.

(24) States, D. J.; Haberkorn, R. A.; Ruben, D. J. A Two-Dimensional Nuclear Overhauser Experiment with Pure Absorption Phase in Four Quadrants. *J. Magn. Reson.* **1982**, *48* (2), 286–292.

(25) Sesti, E. L.; Alaniva, N.; Rand, P. W.; Choi, E. J.; Albert, B. J.; Saliba, E. P.; Scott, F. J.; Barnes, A. B. Magic Angle Spinning NMR Below 6 K with a Computational Fluid Dynamics Analysis of Fluid Flow and Temperature Gradients. *J. Magn. Reson.* **2017**, *286*, 1–9.

(26) Ernst, R. R.; Bodenhausen, G.; Wokaun, A. *Principles of Nuclear Magnetic Resonance in One and Two Dimensions*; Clarendon Press: Oxford, 1990.

(27) Barnes, A. B.; Corzilius, B.; Mak–Jurkauskas, M. L.; Andreas, L. B.; Bajaj, V. S.; Matsuki, Y.; Belenky, M. L.; Lugtenburg, J.; Sirigiri, J. R.; Temkin, R. J.; et al. Resolution and Polarization Distribution in Cryogenic DNP/MAS Experiments. *Phys. Chem. Chem. Phys.* **2010**, *12* (22), 5741–5751.

(28) Takahashi, H.; Fernández-De-Alba, C.; Lee, D.; Maurel, V.; Gambarelli, S.; Bardet, M.; Hediger, S.; Barra, A. L.; De Paëpe, G. Optimization of an Absolute Sensitivity in a Glassy Matrix during DNP-Enhanced Multidimensional Solid-State NMR Experiments. *J. Magn. Reson.* **2014**, *239*, 91–99.

(29) Filibian, M.; Elisei, E.; Serra, S. C.; Rosso, A.; Tedoldi, F.; Cesaro, A.; Carretta, P. Nuclear Magnetic Resonance Studies of DNP-Ready Trehalose Obtained by Solid State Mechanochemical Amorphization. *Phys. Chem. Chem. Phys.* **2016**, *18* (25), 16912–

16920.

(30) Thurber, K. R.; Yau, W. M.; Tycko, R. Low-Temperature Dynamic Nuclear Polarization at 9.4 T with a 30 MW Microwave Source. *J. Magn. Reson.* **2010**, *204* (2), 303–313.

(31) Wickramasinghe, N. P.; Parthasarathy, S.; Jones, C. R.; Bhardwaj, C.; Long, F.; Kotecha, M.; Mehboob, S.; Fung, L. W. M.; Past, J.; Samoson, A.; et al. Nanomole-Scale Protein Solid-State NMR by Breaking Intrinsic1H T1boundaries. *Nat. Methods* **2009**, *6* (3), 215–218.

(32) Shimon, D.; Hovav, Y.; Feintuch, A.; Goldfarb, D.; Vega, S. Dynamic Nuclear Polarization in the Solid State: A Transition between the Cross Effect and the Solid Effect. *Phys. Chem. Chem. Phys.* **2012**, *14* (16), 5729.

(33) Smith, A. A.; Corzilius, B.; Barnes, A. B.; Maly, T.; Griffin, R. G. Solid Effect Dynamic Nuclear Polarization and Polarization Pathways. *J. Chem. Phys.* **2012**, *136* (1).

(34) Hoff, D. E. M.; Albert, B. J.; Saliba, E. P.; Scott, F. J.; Choi, E. J.; Mardini, M.; Barnes, A. B. Frequency Swept Microwaves for Hyperfine Decoupling and Time Domain Dynamic Nuclear Polarization. *Solid State Nucl. Magn. Reson.* **2015**, *72*, 79–89.

(35) Corzilius, B.; Smith, A. A.; Griffin, R. G. Solid Effect in Magic Angle Spinning Dynamic Nuclear Polarization. *J. Chem. Phys.* **2012**, *137* (5), 054201.

(36) Sengupta, I.; Nadaud, P. S.; Helmus, J. J.; Schwieters, C. D.; Jaroniec, C. P. Protein Fold Determined by Paramagnetic Magic-Angle Spinning Solid-State NMR Spectroscopy. *Nat. Chem.* **2012**, *4* (5), 410–417.

(37) Lafon, O.; Thankamony, A. S. L.; Rosay, M.; Aussenac, F.; Lu, X.; Trébosc, J.; Bout-Roumazeilles, V.; Vezin, H.; Amoureux, J.-P. Indirect and Direct ^{29} Si Dynamic Nuclear Polarization of Dispersed Nanoparticles. *Chem. Commun.* **2013**, *49* (28), 2864–2866.

(38) Henstra, A.; Dirksen, P.; Wenckebach, W. T. Enhanced Dynamic Nuclear Polarization by the Integrated Solid Effect. *Phys. Lett. A* **1988**, *134* (2), 134–136.

(39) Henstra, A.; Wenckebach, W. T. The Theory of Nuclear Orientation via Electron Spin Locking (NOVEL). *Mol. Phys.* **2008**, *106* (7), 859–871.

(40) Jain, S. K.; Mathies, G.; Griffin, R. G. Off-Resonance NOVEL. *J. Chem. Phys.* **2017**, *147* (16), 164201.

(41) Can, T. V.; Weber, R. T.; Walish, J. J.; Swager, T. M.; Griffin, R. G. Frequency-Swept Integrated Solid Effect. *Angew. Chemie - Int. Ed.* **2017**, *56* (24), 6744–6748.

Chapter 6: Fast Electron Paramagnetic Resonance Magic Angle Spinning Simulations Using Analytical Powder Averaging Techniques

Forward

This chapter was adapted from the paper "Fast Electron Paramagnetic Resonance Magic Angle Spinning Simulations Using Analytical Powder Averaging Techniques" by Edward P. Saliba and Alexander B. Barnes, submitted to the Journal of Chemical Physics. This chapter describes a novel technique for performing powder averages in magnetic resonance simulations involving the analytical powder averaging over the α Euler angle in the sample. This has the advantage of drastically reducing simulation times in magnetic resonance experiments. The simulations presented in this chapter were performed using the g-tensor and hyperfine coupling tensor values of TEMPO, a nitroxide radical commonly used in DNP and EPR, as a first step towards understanding the spinning requirements for breaking its nearly 900 MHz (at a 7 T magnetic field) into a spinning sideband manifold. Although the simulations done here were to demonstrate the speed with which a broad line radical requiring a large number of powder angles to represent can be performed, the techniques described in this chapter are perfectly applicable to NMR as well. The ability to quickly simulate new experiments in both EPR and NMR will allow for a better understanding of the mechanisms involved in them and facilitate their development going forward.

Abstract

Simulations describing the spin physics which underpins nuclear magnetic resonance spectroscopy (NMR) and electron paramagnetic resonance (EPR) spectroscopy play an important role in the design of magnetic resonance experiments. In experiments performed in the solid state, samples are commonly composed of powders or glasses, with molecules oriented at a large number of angles with respect to the laboratory frame. These powder angles must be represented in simulations to account for anisotropic interactions. Numerical techniques are typically used to accurately compute such powder averages. In order to characterize the powder pattern, a large number of Euler Angles is usually required, leading to lengthy simulation times. This is particularly true in broad spectra, such as those observed in electron paramagnetic resonance (EPR). The combination of the traditionally separate techniques of EPR and magic angle spinning (MAS) NMR could play an important role in future electron detected experiments, combined with DNP, which will allow for exceptional detection sensitivity of NMR spin coherences. Presented herein is a method of reducing the required number of Euler angles in magnetic resonance simulations by analytically performing the powder average over one of the Euler angles in the static and MAS cases for the TEMPO nitroxide radical in a 7 Tesla field. In the static case, this leads to a 97.5% reduction in simulation time over the fully numerically averaged case, and accurately reproduces the expected spinning sideband manifold when simulated with a high MAS frequency of 150 kHz. This technique is applicable to more traditional NMR experiments as well, such as those involving quadrupolar nuclei or multiple dimensions.

6.1 Introduction

Nuclear magnetic resonance (NMR) spectroscopy is a powerful analytical tool used in a wide range of disciplines including structural biology, pharmacology, and materials science[1–5]. However, NMR suffers from poor sensitivity due to nuclear spin energy splittings that are typically much smaller than the thermal energy. As a result, there is considerable research focus on improving NMR sensitivity.

Sensitivity in magnetic resonance techniques, like NMR spectroscopy and the closely related electron paramagnetic resonance (EPR) spectroscopy, improves with detection frequency. The relative sensitivity of detecting two spins with different gyromagnetic ratios is $(\gamma_2/\gamma_1)^{3/2}$; one power of (γ_2/γ_1) arises from the relative magnitudes of each of the polarized magnetic moments, and one arises from the fact that the magnitude of the voltage induced across a coil by an alternating current increases with frequency. One half power of (γ_2/γ_1) is lost at higher detection frequencies because, in addition to improved signal detection, noise detection is also improved. The combined contributions of each of these effects leads to the $(\gamma_2/\gamma_1)^{3/2}$ dependence of the sensitivity[6]. This is often exploited in NMR spectroscopy by detecting protons which have roughly $4\times$ higher gyromagnetic ratio than ^{13}C spins. The fact that a proton has a $4\times$ higher gyromagnetic ratio than that of a ^{13}C nucleus results in a sensitivity improvement of $4^{3/2} = 8$. Furthermore, another (γ_2/γ_1) factor is acquired from the higher Boltzmann polarization of protons in the high temperature limit, resulting in a $(\gamma_2/\gamma_1)^{5/2}$ dependence of the sensitivity on (γ_2/γ_1). The increase in sensitivity over a ^{13}C Bloch Decay experiment then increases from 8 to 16. Due to the stochastic nature of signal averaging experiments, the $16\times$

improved signal-to-noise (SNR) manifests as a gain of $16^2 = 256\times$ time improvement of a ^{1}H Bloch decay experiment over a ^{13}C Bloch decay experiment. While solution-state NMR has leveraged proton detection for many years[7,8] , solid-state NMR has only recently turned to proton detection to push the limits of NMR sensitivity, which has been enabled by the advent of magic angle spinning (MAS) frequencies > 40 kHz[9–13].

Dynamic nuclear polarization (DNP) is another technique to enhance NMR sensitivity that employs the transfer of the large electron spin polarization to nuclear spins[14–23]. DNP could theoretically increase ^{1}H spin state polarizations by up to $657\times$, with enhancements of up to 515 having been achieved experimentally[24,25]. Direct detection of unpaired electrons could result in up to a $657^{3/2} = 16{,}840\times$ gain in sensitivity over conventional DNP. Electron detected magnetic resonance experiments are already commonly performed without MAS using techniques such as electron-nuclear double resonance (ENDOR)[26]and electron spin echo envelope modulation (ESEEM)[27]. Such strategies could be used to drastically improve the rate at which typically lengthy experiments such as multidimensional spectroscopy and in-cell NMR can be collected by collapsing the directly detected electron dimension down to give an NMR spectrum in the remaining dimensions with excellent sensitivity. Similar strategies have previously been used in ^{1}H detected NMR experiments.

Nevertheless, the theoretical limit of $657^{3/2} = 16840\times$ the sensitivity over conventional DNP will only be approached with improved instrumentation that enables the averaging of anisotropic electron spin interactions. In principle, the electron spin powder pattern will break into sidebands when the spinning frequency is faster than homogeneous spin interactions[28]. Stable organic

radicals are commonly used in EPR spectroscopy. EPR spectroscopy of biological chemical architectures often employs nitroxides for analysis of structures and dynamics[29] with the TEMPO radical being one such nitroxide. Therefore, to examine behavior of the nearly 900 MHz wide powder pattern of TEMPO under MAS, a series of simulations were performed employing a home-written PYTHON computer code.

In traditional magnetic resonance simulations, the time dependence of the signal is simulated at many different powder angles. Averaging all of these time dependencies yields an approximation of the powder pattern[30,31]. However, such numerical integration schemes can be quite slow, with the powder average dominating the total simulation time. This problem is exacerbated in EPR spectra, which are orders of magnitude broader than typical spin-1/2 NMR spectra due to much stronger interactions of the electron spins. Simulation times can be dramatically reduced with an analytical solution for the functional form of the powder average, reducing hundreds or even thousands of calculations to a relatively small number. Such techniques have proven useful in the analytical powder averaging of spin echo double resonance (SEDOR), rotational echo double resonance (REDOR), and transferred echo double resonance (TEDOR) standard curves[32]. Here, derivations of analytical solutions for the powder averaging of the TEMPO EPR signal over one of the three Euler angles in both the static and MAS cases are presented. These solutions are used to perform simulations that demonstrate significant time savings over traditional numerical techniques. The improvement in simulation time will allow for new experiments to be designed that leverage the sensitivity afforded by MAS electron detected magnetic resonance combined with DNP.

6.2 Theory

6.2.1 Static TEMPO Powder Pattern

As a demonstration of how to directly integrate the signal over the α Euler angle, the static TEMPO powder pattern was examined first. The powder-averaged signal ($\bar{s}(t)$) with the carrier frequency set to remove the isotropic component of the g-tensor is given in Equation (6.1):

$$\bar{s}(t) \propto \int_0^{2\pi} \int_0^{\pi} \exp(i\omega t)\sin(\beta)\, d\alpha\, d\beta \tag{6.1}$$

Here, t is the time and α and β are the Euler angles that describe the orientation of the principal axis frame of the g tensor relative to the lab frame. Rather fortuitously, the g-tensor of TEMPO shares a principal axis frame with the hyperfine coupling tensor, removing the need to perform an intermediate rotation between the two. i is the imaginary unit and ω is defined in Equation (6.2):

$$\omega = mA_{iso} + \frac{1}{2}\omega_{aniso}\left[3\cos^2(\beta) - 1 - \eta\sin^2(\beta)\cos(2\alpha)\right] \tag{6.2}$$

ω_{aniso} and η are defined in Equations (6.3)-(6.5):

$$\Delta\omega_S = -\frac{g_{aniso}\mu_B B_0}{\hbar} \tag{6.3}$$

$$\omega_{aniso} = \Delta\omega_S + mA_{aniso} \tag{6.4}$$

$$\eta = \frac{\Delta\omega_S \eta_S + m A_{aniso} \eta_A}{\omega_{aniso}} \tag{6.5}$$

where $\hbar$ is the reduced Planck's Constant, μ_B is the Bohr Magneton, and m is the magnetic quantum number of the spin-1 ^{14}N nucleus that is hyperfine coupled to the electron on the TEMPO radical. g_{iso}, g_{aniso}, η_g, A_{iso}, A_{aniso}, and η_A are defined in Equations (6.6)-(6.11):

$$g_{iso} = \frac{1}{3}\left(g_{XX} + g_{YY} + g_{ZZ}\right) \tag{6.6}$$

$$g_{aniso} = g_{ZZ} - g_{iso} \tag{6.7}$$

$$\eta_g = \frac{g_{YY} - g_{XX}}{g_{aniso}} \tag{6.8}$$

$$A_{iso} = \frac{1}{3}\left(A_{XX} + A_{YY} + A_{ZZ}\right) \tag{6.9}$$

$$A_{aniso} = A_{ZZ} - A_{iso} \tag{6.10}$$

$$\eta_A = \frac{A_{YY} - A_{XX}}{A_{aniso}} \tag{6.11}$$

Here, g_{iso}, g_{aniso}, and η_g are the isotropic component, anisotropic component, and asymmetry of the the g-tensor, respectively. A_{iso}, A_{aniso}, and η_A are the analogous values for the hyperfine coupling tensor. To obtain the full signal, Equation (6.1) should be summed over the possible

values of m, which are $m = +1$, $m = 0$, and $m = -1$. All the derived equations assume a secular Hamiltonian. The quadrupolar coupling of the nitrogen nucleus has been ignored.

Visual representations of the effective tensor quantities described in Equations (6.3)-(6.5) made with the TensorView[33] Mathematica notebook are shown in Figure 6.1. Figure 6.1a shows the TEMPO molecule. Images of the TEMPO molecule down the oxygen-nitrogen bond are shown with the effective tensor superimposed on the oxygen molecule for the $m = -1$ (b), $m = 0$ (c) and $m = +1$ (d) cases. Note that the shape of the surfaces are not ellipsoids, as they are commonly represented[33,34]. A more accurate visual representation of the values taken by the Hamiltonian as a function of the angle of the molecule is given by these "Jorgenson-Salem" plots, where the radial component of the surface is proportional to the magnitude of the energy splitting induced by the interaction when the molecule is oriented at the α and β angles of that point on the surface, relative to the external magnetic field[33–36]. ω_{XX}, ω_{YY}, and ω_{ZZ} are defined in Equations (6.12)-(6.14) below:

$$\omega_{XX} = \frac{\left(g_{XX} - g_{iso}\right)\mu_B B_0}{\hbar} + mA_{XX} \tag{6.12}$$

$$\omega_{YY} = \frac{\left(g_{YY} - g_{iso}\right)\mu_B B_0}{\hbar} + mA_{YY} \tag{6.13}$$

$$\omega_{ZZ} = \frac{\left(g_{ZZ} - g_{iso}\right)\mu_B B_0}{\hbar} + mA_{ZZ} \tag{6.14}$$

The orientation of the principal axis frame of the g-tensor and hyperfine coupling tensor (they are coincident with one another) relative the lab frame was calculated using Gaussian09.

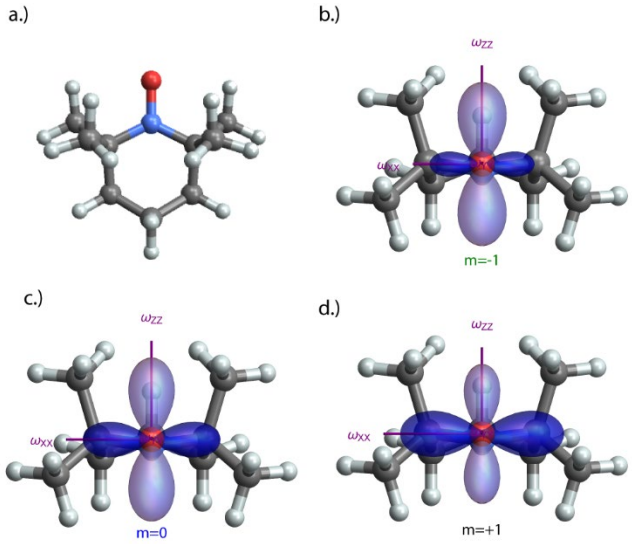

Figure 6.1: The TensorView Mathematica notebook was used to produce graphical representations of the g-tensor, which is the effective tensor that is the result of the combined effects of the g-tensor and hyperfine coupling tensor. The TEMPO molecule is shown in (a) perpendicular to the N-O bond. The ω tensor superimposed on the TEMPO molecule is shown down the N-O bond for the $m = -1$ (b), $m = 0$ (c), and $m = +1$ (d) cases.

The exponential portion of the integrand of Equation (6.1) can be split into a portion that depends on the α Euler angle and a portion that does not. In Equation (6.15), the portion that does not depend on α has been pulled out of the appropriate integral:

$$\begin{aligned}\bar{s}(t) \propto & \int_0^{\pi} \exp\left[i\left[mA_{iso} + \frac{1}{2}\omega_{aniso}\left(3\cos^2(\beta) - 1\right)\right] t\right] \\ & \times \left[\int_0^{2\pi} \exp\left[-i\left(\frac{1}{2}\right)\omega_{aniso}\eta t \sin^2(\beta)\cos(2\alpha)\right] d\alpha \right] \\ & \times \sin(\beta)\, d\beta\end{aligned} \tag{6.15}$$

We can now make the definitions in Equations (6.16) and (6.17):

$$C = \left[mA_{iso} + \frac{1}{2}\omega_{aniso}\left(3\cos^2(\beta) - 1\right) \right] t \tag{6.16}$$

$$z = -\left(\frac{1}{2}\right)\omega_{aniso}\eta t \sin^2(\beta) \tag{6.17}$$

Substitution of Equations (6.16) and (6.17) into Equation (6.15) gives Equation (6.18):

$$\bar{s}(t) \propto \int_0^{\pi} \exp[iC] \times \left[\int_0^{2\pi} \exp\left[iz\cos(2\alpha) \right] d\alpha \right] \times \sin(\beta)\, d\beta \tag{6.18}$$

The following substitution can be made using the Jacobi-Anger identity[32,37], which is the Fourier series in 2α for $\exp[iz\cos(2\alpha)]$:

$$\exp\left[iz\cos(2\alpha) \right] = J_0(z) + 2\sum_{n=1}^{\infty} i^n J_n(z)\cos(2n\alpha) \tag{6.19}$$

where, the J_n's are the n^{th}-order Bessel functions of the first kind, the first five of which are plotted in Figure 6.2.

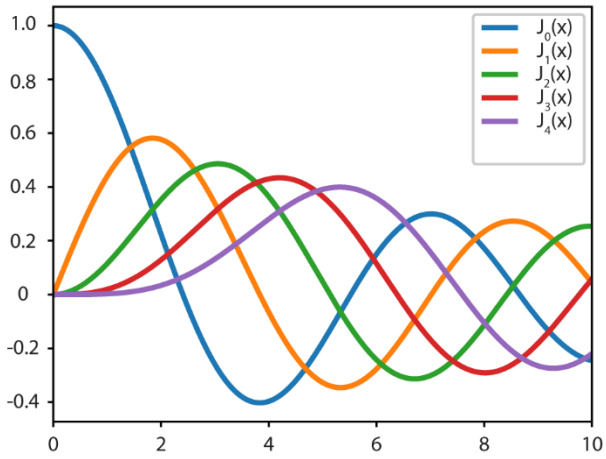

Figure 6.2: The first five Bessel functions (orders 0-4). The Bessel Functions contribute to the weighting factors in the Jacobi-Anger expansion used to produce an analytical solution for the integration over the α Euler angle.

Equation (6.19) can be substituted into Equation (6.18) to give Equation (6.20):

$$\bar{s}(t) \propto \int_0^{\pi} \exp[iC] \times \left[\int_0^{2\pi} J_0(z)\, d\alpha + 2 \int_0^{2\pi} \sum_{n=1}^{\infty} i^n J_n(z) \cos(2n\alpha)\, d\alpha \right] \times \sin(\beta)\, d\beta \qquad (6.20)$$

Noting that all of the components in the second term (in red) integrate to 0 on the interval from 0 to 2π, the integration over α is greatly simplified, and this is performed in Equation (6.21):

$$\begin{aligned} \bar{s}(t) &\propto 2\pi \int_0^{\pi} \exp\left[i \left[mA_{iso} + \frac{1}{2} \omega_{aniso} \left(3\cos^2(\beta) - 1 \right) \right] t \right] \\ &\times J_0\left(\left(\frac{1}{2} \right) \omega_{aniso} \eta t \sin^2(\beta) \right) \sin(\beta)\, d\beta \end{aligned} \qquad (6.21)$$

The expressions for C and z have been substituted back into the equation. The sign of z has been changed, recognizing that $J_0(z)$ is a symmetric function of z. From here, the integration over β can be performed using traditional numerical techniques.

It should be noted that a fully analytical solution over both the α and β Euler angles involving elliptic integrals of the first kind does exist[38]. However, the technique presented here was chosen because it has strong parallels to the analytical averaging technique used for the magic angle spinning case derived in the next section.

6.2.2 TEMPO Powder Pattern Under MAS

The analytical powder averaging strategy described above can be extended to include MAS. The expression for the signal given in Equation (6.22) needs to be modified to:

$$\bar{s}(t) \propto \int_0^{2\pi}\int_0^{\pi}\int_0^{2\pi} \exp\left[i\int_0^t \omega(t',\alpha,\beta,\gamma)\,dt' \right] \sin(\beta)\,d\alpha\,d\beta\,d\gamma \tag{6.22}$$

Here, the integral of the frequency function over time needs to be computed, as it acquires a time dependence under MAS. Also, the integral over the γ Euler angle needs to be computed because the function is no longer independent of it, as in the static case. Furthermore, the definitions of all three Euler angles have changed, and now characterize the rotations from the principal axis frame of the g-tensor to a frame of reference fixed on the rotor. $\omega(t,\alpha,\beta,\gamma)$ is defined in Equation (6.23). This expression can be derived using the spherical tensor formalism described

by Mueller[39]. The curly brackets ({}) denote a part of an expression that has been broken up into multiple lines:

$$\omega(t,\alpha,\beta,\gamma)=\omega_{aniso} \times\left\{\begin{array}{l}\left[\frac{1}{2}\sin^2(\beta)-\frac{1}{4}\eta\cos(2\alpha)\left(1+\frac{1}{3}\cos(2\beta)\right)\right]\times\cos(2\omega_r t+2\gamma)\\ +\frac{1}{3}\eta\sin(2\alpha)\cos(\beta)\times\sin(2\omega_r t+2\gamma)\\ -\frac{1}{\sqrt{2}}\left(1+\frac{1}{3}\eta\cos(2\alpha)\right)\sin(2\beta)\times\cos(\omega_r t+\gamma)\\ +\frac{\sqrt{2}}{3}\eta\sin(2\alpha)\sin(\beta)\times\sin(\omega_r t+\gamma)\end{array}\right\} \tag{6.23}$$

Integration of Equation (6.23) over time yields Equation (6.24):

$$\int_0^t\omega(t',\alpha,\beta,\gamma)dt'=\omega_{aniso} \times\left\{\begin{array}{l}\left[\frac{1}{2}\sin^2(\beta)-\frac{1}{4}\eta\cos(2\alpha)\left(1+\frac{1}{3}\cos(2\beta)\right)\right]\times\left[\frac{\sin(2\omega_r t+2\gamma)-\sin(2\gamma)}{2\omega_r}\right]\\ +\frac{1}{3}\eta\sin(2\alpha)\cos(\beta)\times\left[\frac{\cos(2\omega_r t+2\gamma)-\cos(2\gamma)}{2\omega_r}\right]\\ -\frac{1}{\sqrt{2}}\left(1+\frac{1}{3}\eta\cos(2\alpha)\right)\sin(2\beta)\times\left[\frac{\sin(\omega_r t+\gamma)-\sin(\gamma)}{\omega_r}\right]\\ +\frac{\sqrt{2}}{3}\eta\sin(2\alpha)\sin(\beta)\times\left[\frac{\cos(\omega_r t+\gamma)-\cos(\gamma)}{\omega_r}\right]\end{array}\right\} \tag{6.24}$$

If Equation (6.24) is substituted into Equation (6.22), it can be divided into three parts: (i) one that does not depend on the α Euler Angle, (ii) one that depends on $\cos(2\alpha)$, and (iii) one that depends on $\sin(2\alpha)$. This is performed in Equation (6.25):

$$\bar{s}(t) \propto \int_0^{2\pi}\int_0^{\pi} \exp[iC] \times \left[\int_0^{2\pi} \exp\left[iz_c \cos(2\alpha) \right] \exp\left[iz_s \sin(2\alpha) \right] d\alpha \right] \times \sin(\beta)\, d\beta d\gamma \quad (6.25)$$

Here, C, z_c, and z_s are given by Equations (6.26)-(6.28):

$$C = \omega_{aniso} \times \left\{ \begin{array}{l} \frac{1}{2}\sin^2(\beta)\left(\frac{\sin(2\omega_r t + 2\gamma) - \sin(2\gamma)}{2\omega_r} \right) \\ -\frac{1}{\sqrt{2}}\sin(2\beta)\left(\frac{\sin(\omega_r t + \gamma) - \sin(\gamma)}{\omega_r} \right) \end{array} \right\} \quad (6.26)$$

$$z_c = \omega_{aniso}\eta \left\{ \begin{array}{l} -\frac{1}{4}\left(1 + \frac{1}{3}\cos(2\beta) \right)\left(\frac{\sin(2\omega_r t + 2\gamma) - \sin(2\gamma)}{2\omega_r} \right) \\ -\frac{1}{3}\left(\frac{1}{\sqrt{2}} \right)\sin(2\beta)\left(\frac{\sin(\omega_r t + 2\gamma) - \sin(\gamma)}{\omega_r} \right) \end{array} \right\} \quad (6.27)$$

$$z_s = \omega_{aniso}\eta \left\{ \begin{array}{l} -\frac{1}{3}\cos(\beta)\left(\frac{\cos(2\omega_r t + 2\gamma) - \cos(2\gamma)}{2\omega_r} \right) \\ -\left(\frac{\sqrt{2}}{3} \right)\sin(\beta)\left(\frac{\cos(\omega_r t + 2\gamma) - \cos(\gamma)}{\omega_r} \right) \end{array} \right\} \quad (6.28)$$

The exponential terms of Equation (6.25) can now be expanded using the Jacobi-Anger Identities:

$$\exp\left[iz_c\cos\left(2\alpha\right)\right]=J_0\left(z_c\right)+2\sum_{n=1}^{\infty}i^nJ_n\left(z_c\right)\cos\left(2n\alpha\right) \tag{6.29}$$

$$\begin{aligned}\exp\left[iz_s\cos\left(2\alpha\right)\right]&=J_0\left(z_s\right)+2\sum_{m=1}^{\infty}J_{2m}\left(z_s\right)\cos\left(4m\alpha\right)\\&+2i\sum_{m=1}^{\infty}J_{2m-1}\left(z_s\right)\cos\left(2\left(2m-1\right)\alpha\right)\end{aligned} \tag{6.30}$$

If Equations (6.29) and (6.30) are substituted into Equation (6.25), we obtain Equation (6.31):

$$\begin{aligned}\bar{s}\left(t\right)\propto&\int_0^{2\pi}\int_0^{\pi}\exp\left[iC\right]\times\int_0^{2\pi}\left[J_0\left(z_c\right)+2\sum_{n=1}^{\infty}i^nJ_n\left(z_c\right)\cos\left(2n\alpha\right)\right]\\&\times\left[J_0\left(z_s\right)+2\sum_{m=1}^{\infty}J_{2m}\left(z_s\right)\cos\left(4m\alpha\right)+2i\sum_{m=1}^{\infty}J_{2m-1}\left(z_s\right)\cos\left(2\left(2m-1\right)\alpha\right)\right]\\&\times d\alpha\sin\left(\beta\right)d\beta d\gamma\end{aligned} \tag{6.31}$$

Expansion of Equation (6.31) yields Equation (6.32):

$$\bar{s}(t) \propto \int_0^{2\pi}\int_0^{\pi} \exp[iC]$$
$$\times\int_0^{2\pi}\left\{\begin{array}{l} J_0(z_c)J_0(z_s) \\ +2J_0(z_c)\left[\sum_{m=1}^{\infty} J_{2m}(z_s)\cos(4m\alpha)\right] \\ +2iJ_0(z_c)\left[\sum_{m=1}^{\infty} J_{2m-1}(z_s)\cos(2(2m-1)\alpha)\right] \\ +2J_0(z_s)\left[\sum_{n=1}^{\infty} i^n J_n(z_c)\cos(2n\alpha)\right] \\ +4\left[\sum_{n=1}^{\infty} i^n J_n(z_c)\cos(2n\alpha)\right]\left[\sum_{m=1}^{\infty} J_{2m}(z_s)\cos(4m\alpha)\right] \\ +4i\left[\sum_{n=1}^{\infty} i^n J_n(z_c)\cos(2n\alpha)\right]\left[\sum_{m=1}^{\infty} J_{2m-1}(z_s)\sin(2(2m-1)\alpha)\right] \end{array}\right\} \tag{6.32}$$
$$\times da\sin(\beta)\,d\beta d\gamma$$

As in the static case, the terms in red integrate to 0 on the interval from 0 to 2π. For the term in purple, *most* of the terms are 0. In Equation (6.33), the terms in red have been removed:

$$\bar{s}(t) \propto \int_0^{2\pi}\int_0^{\pi} \exp[iC]$$
$$\times\int_0^{2\pi}\left[J_0(z_c)J_0(z_s)+4\left[\sum_{n=1}^{\infty} i^n J_n(z_c)\cos(2n\alpha)\right]\left[\sum_{m=1}^{\infty} J_{2m}(z_s)\cos(4m\alpha)\right]\right] \tag{6.33}$$
$$\times da\sin(\beta)\,d\beta d\gamma$$

In order to determine which terms zero out in the purple term of Equations (6.32) and (6.33), the indices are shifted down by 1, so that they start at 0, rather than 1, as is done in Equation (6.34). Altered items have been colored in orange:

$$\bar{s}(t) \propto \int_0^{2\pi}\int_0^{\pi} \exp[iC] \times \int_0^{2\pi}\left[J_0(z_c)J_0(z_s) + 4\left[\sum_{n=0}^{\infty} i^{n+1} J_{n+1}(z_c)\cos\left(2(n+1)\alpha\right)\right]\left[\sum_{m=0}^{\infty} J_{2(m+1)}(z_s)\cos\left(4(m+1)\alpha\right)\right]\right] \times da\sin(\beta)\,d\beta\,d\gamma \tag{6.34}$$

From here, the Cauchy product of the two sums can be taken, replacing the product of two infinite sums with two nested sums:

$$\bar{s}(t) \propto \int_0^{2\pi}\int_0^{\pi} \exp[iC] \times \int_0^{2\pi}\left[J_0(z_c)J_0(z_s) + 4\sum_{k=0}^{\infty}\sum_{l=0}^{k} i^{l+1} J_{l+1}(z_c)J_{2(k-l+1)}(z_s)\cos\left(2(l+1)\alpha\right)\cos\left(4(k-l+1)\alpha\right)\right] \times da\sin(\beta)\,d\beta\,d\gamma \tag{6.35}$$

The terms in these sums are only non-zero when the condition given by Equation (6.36) is met:

$$2(l+1) = 4(k-l+1) \tag{6.36}$$

Solving Equation (6.36) for l yields Equation (6.37):

$$l = \frac{2}{3}k + \frac{1}{3} \tag{6.37}$$

Because l has to be an integer, this condition can only be fulfilled for certain values of k. Values of k that fulfill Equation (6.37) are $k = 1,4,7$ ... and so on. All other values of k should be removed from the sum. l is replaced with the expression given in Equation (6.37), and remove the sum over l. These are both done in Equation (6.38):

$$\begin{aligned}&\bar{s}(t) \propto \int_0^{2\pi}\int_0^{\pi} \exp[iC] \\ &\times\int_0^{2\pi}\left[J_0(z_c)J_0(z_s)+4\sum_{k=1,4,7...}^{\infty} i^{\frac{2}{3}k+\frac{4}{3}}J_{\frac{2}{3}k+\frac{4}{3}}(z_c)J_{\frac{2}{3}k+\frac{4}{3}}(z_s)\cos^2\left(\left(\frac{4}{3}k+\frac{8}{3}\right)\alpha\right)\right] \\ &\times da\sin(\beta)\,d\beta d\gamma\end{aligned} \tag{6.38}$$

The first term in black is constant with respect to α, and simply picks up a factor of 2π under the integration over α. k has been chosen such that $\frac{4}{3}k+\frac{8}{3}$ is always an integer, so all of the squared cosine terms in the purple sum integrate to π on the interval from 0 to 2π, giving Equation (6.39) :

$$\begin{aligned}&\bar{s}(t) \propto \int_0^{2\pi}\int_0^{\pi} \exp[iC] \\ &\times\int_0^{2\pi}\left[2\pi J_0(z_c)J_0(z_s)+4\pi\sum_{k=1,4,7...}^{\infty} i^{\frac{2}{3}k+\frac{4}{3}}J_{\frac{2}{3}k+\frac{4}{3}}(z_c)J_{\frac{2}{3}k+\frac{4}{3}}(z_s)\right] \\ &\times da\sin(\beta)\,d\beta d\gamma\end{aligned} \tag{6.39}$$

Now we can make the substitution $k \Rightarrow 3k-2$, which allows us to sum from $k = 1$ to $k = \infty$, rather than a complicated list of nonconsecutive numbers. This is performed in Equation(6.40):

$$\bar{s}(t) \propto \int_0^{2\pi}\int_0^{\pi} \exp[iC] \times \int_0^{2\pi}\left[2\pi J_0(z_c)J_0(z_s) + 4\pi\sum_{k=1}^{\infty} i^{2k} J_{2k}(z_c)J_{2k}(z_s)\right] \times da \sin(\beta)\, d\beta d\gamma \tag{6.40}$$

From here, the β and γ Euler angles can be numerically integrated using traditional numerical techniques.

6.3 Simulations

Figures 6.3a and 6.3b show simulations of static powder patterns of the TEMPO radical. The g-tensor and hyperfine coupling tensor principal axis values used in all simulations were obtained from Wenckebach[40], where the g-tensor is given as a gyromagnetic ratio tensor with principal axis values $\gamma_{XX} = -28.124 \times 10^9$ Hz, $\gamma_{YY} = -28.084 \times 10^9$ Hz, and $\gamma_{ZZ} = -28.016 \times 10^9$ Hz. The hyperfine coupling tensor principal axis values provided are $A_{XX} = 17.7 \times 10^6$ Hz, $A_{YY} = 20.5 \times 10^6$ Hz, and $A_{ZZ} = 100.96 \times 10^6$ Hz. Note that all of these values should be multiplied by a factor of 2π to convert them into angular frequency units for use in the equations derived here.

The calculation of the time domain signal for Figure 6.3a was carried out on 8 computer processors. 200,000 (α, β) powder angle pairs were chosen to reside on a Fibonacci sphere, a method for generating a very uniform distribution of points over the unit sphere and commonly used in numerical integration schemes in other fields[41,42]. However, it has not seen use in

magnetic resonance simulations to our knowledge. The Fibonacci sphere was chosen because of its ease of programming compared with more common magnetic resonance powder averaging schemes such as REPULSION[31], as well its excellent performance in in equitably distributing points on the unit sphere. An example of the distribution of points over a Fibonacci Sphere is demonstrated in Figure 6.4. For simplicity, except when the signal is totally independent of a given Euler Angle (as is the case with γ in the static case), integration was performed over the full ranges of all of the Euler angles, and symmetries of the system were not exploited to reduce the number of powder angles. The simulation was performed assuming a 7 T external magnetic field. 2,048 points were simulated with the dwell time set to give a spectral window of 1.6 GHz. The resulting time domain simulation was zero filled to 2,097,152 points and a Fast Fourier Transform (FFT) was applied. Processing was performed on a desktop computer after the time domain simulation on a computer cluster.

The simulation time for the time domain signal was 115 seconds. 200,000 powder angles were clearly not nearly enough to accurately characterize this powder pattern. This is the result of the "noise" in the simulated spectrum. This can be remedied by adding more powder angles to the simulation, but at the cost of longer simulation times.

Figure 6.3b was simulated using Equation (6.21). This expression, which is analytically averaged over the α Euler angle, removes the need to perform that part of the integral numerically, drastically reducing the number of powder angles needed to accurately characterize the powder pattern. The simulation in Figure 6.3b used only 4,096, equally spaced β powder angles to average over Equation (6.21). All other parameters were the same as the fully

numerically integrated case shown in Figure 6.3a. Calculation of the time domain signal and processing was performed on a single processor of a desktop computer and it took only 23 seconds, representing an 80% decrease in simulation time over the 115 seconds of the fully numerically integrated case, with fewer resources. If the reduction in resources is taken into account, this amounts to a total time saving of 97.5%. The individual powder patterns contributing to the summed spectrum (in red) are also shown with the $m = -1$ powder pattern shown in green, $m = 0$ in blue, and $m = +1$ in black. It should be noted that the size of the powder average can be reduced through spectral binning techniques[43] and through broadening of the resonance, which has a similar affect of "smearing out" the spectrum and removing the resolution of the individual powder angles that are present when an insufficient powder set is used. This can be applied to both the numerically averaged and analytically averaged spectra.

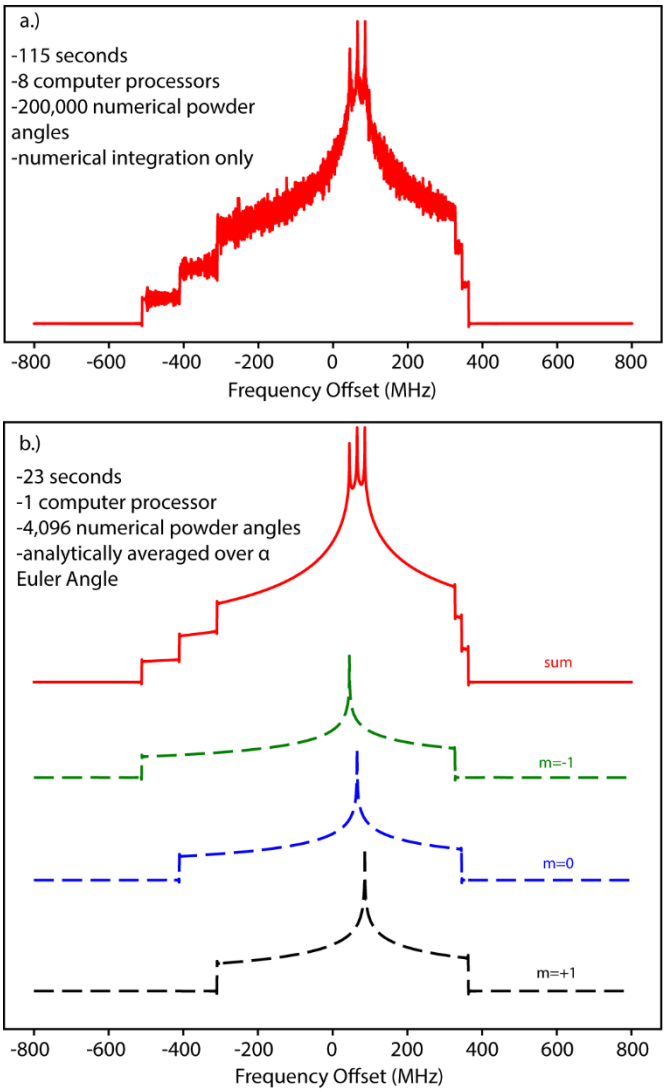

Figure 6.3: Simulations performed using only numerical integration for the powder average (a) and analytical integration over the α Euler angle (b). In (b), the individual powder patterns that correspond to each value of m for the ^{14}N nucleus are plotted. If the reduction in resources is considered, a 97.5% reduction in simulation time using analytical averaging methods over numerical methods is observed, with higher quality results.

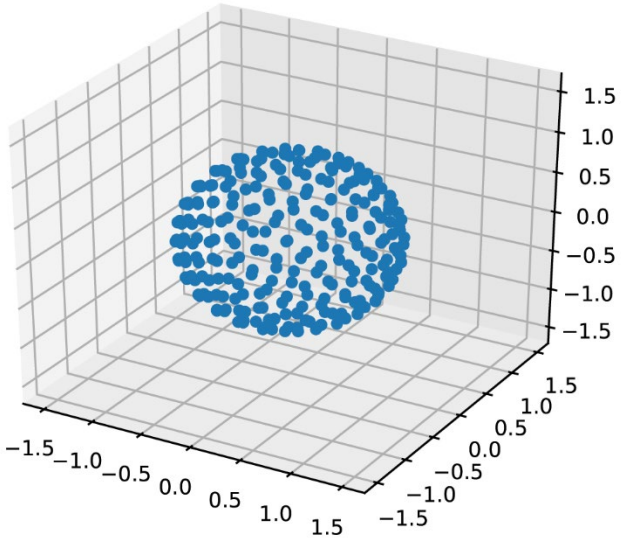

Figure 6.4: An example Fibonacci sphere. The Fibonacci Sphere is an extremely uniform distribution of points over a unit sphere, and was used to generate the powder set used for numerical averaging. The homogeneity of the distribution of powder angles helps to keep the number of required angles relatively low.

The MAS case is demonstrated in Figure 6.5a, which was simulated using Equation (6.40). The analytical solution for the integration over the α Euler angle successfully reproduced the extensive spinning sideband manifold expected for spinning frequencies much less than the linewidth of the spectrum. Each inset in Figure 6.5a shows an expansion around the frequency range from -0.7 MHz to 0.7 MHz offset. Figure 6.5b shows a further expansion of the spectra in Figure 6.5a. The spinning sidebands are split by the simulated spinning frequency of 150 kHz. The groups of 3 partially resolved resonances arise from various different spinning sidebands of each m state's signal overlapping one another. $16{,}384$ (β, γ) Euler angle pairs were chosen on a Fibonacci sphere to perform the numerical integration, and the first 10 terms (terms $0-9$) were included in the sum given by Equation (6.40). $262{,}144$ time domain points were simulated with zero filling to $2{,}097{,}152$ points. 20 μs of homogeneous broadening was applied, which is comparable to values that have been determined experimentally in heavily deuterated protein

samples[44,45]. Finally, an FFT was performed. The time domain simulation took 61 hours, 20 minutes, 49 seconds on 8 computer processors.

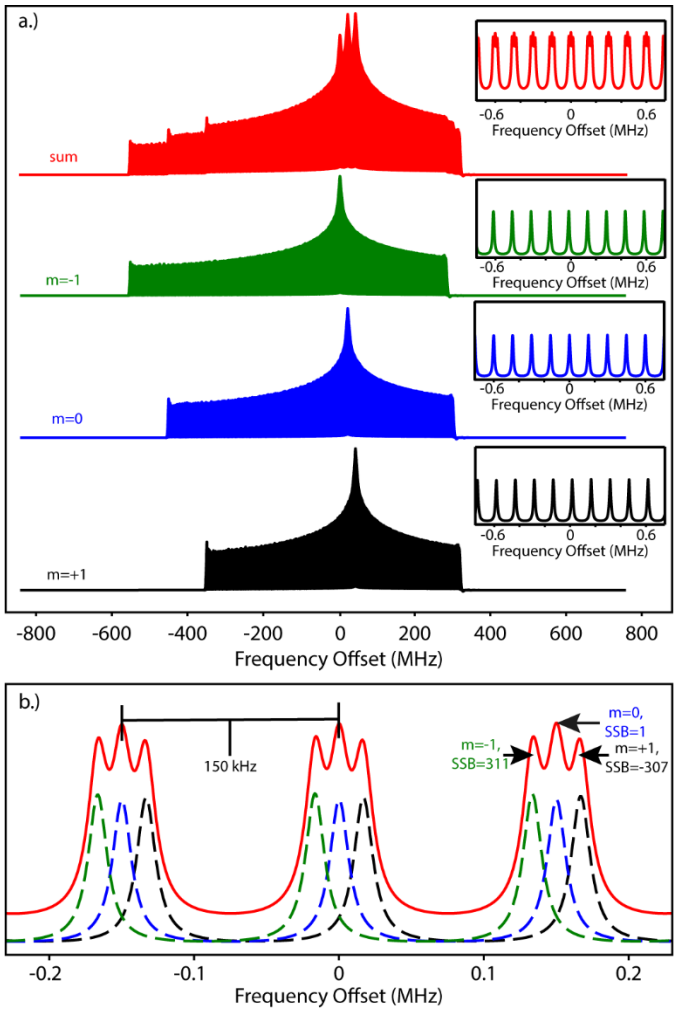

Figure 6.5: (a) The spinning sideband manifolds produced in simulations of the TEMPO powder patterns for the $m = -1$ (green), $m = 0$ (blue), and $m = +1$ (black) states of the ^{14}N nucleus. The sum is shown in red. The insets show expansions of their respective powder patterns on the interval from -0.7 MHz to 0.7 MHz offset. (b) An expansion of the curves shown in (a) on the interval from -0.23 MHz to 0.23 MHz offset. The spinning sidebands (SSB) are spit by the spinning frequency of 150 kHz.

The resolution of spinning sidebands in electron detected magnetic resonance will improve with spinning frequency and with application of electron decoupling[14–17,46,47]. This will be accompanied by a concomitant improvements in the homogeneous T_2. Spinning frequencies of

up to 1 MHz could potentially be achieved in the coming years as rotors are pushed to smaller diameters. Figure 6.6 provides much the same information as Figure 6.5, except with 1 MHz MAS. The simulation was performed with the first 6 terms of Equation (6.40), and with 10,000 (β,γ) Euler angle pairs residing on a Fibonacci sphere were simulated. In this case, 50 μs of homogeneous broadening was applied. All other parameters were the same as those used to produce Figure 6.5.

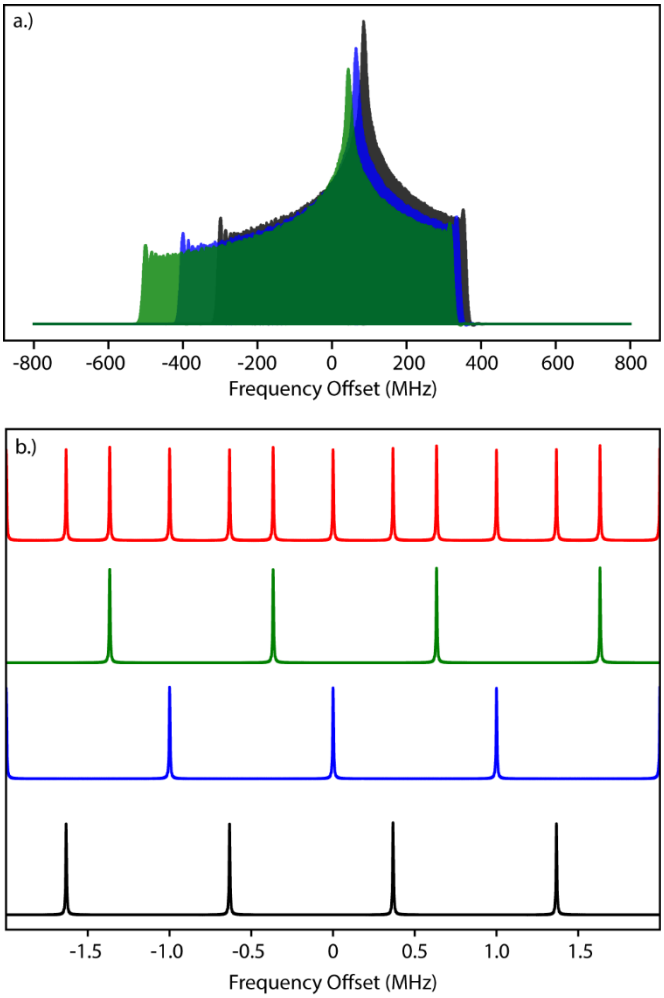

Figure 6.6: (a) The TEMPO powder patterns corresponding to the $m = +1$ (black), $m = 0$ (blue), and $m = -1$ (green) states of the ^{14}N that the electron is coupled to under 1 MHz MAS superimposed on one another. The shadow effect allows each individual powder pattern to be seen. (b) An expansion of (a) about 0 MHz offset. The summed powder pattern is shown in red. Unlike Figure 6.5b, the spinning sideband manifolds are resolved from one another at the new spinning frequency.

Figure 6.7 demonstrates the favorable convergence properties of the infinite sum solution presented in Equation (6.40). The blue spectrum was simulated using only the first term in the sum, $\int_0^{2\pi}\int_0^{\pi} \exp[iC]\,[2\pi J_0(z_c)J_0(z_s)]\sin(\beta)\,d\beta d\gamma$. By including only the first term, the major feature of the spectrum, the hyperfine splitting at the low frequency end, is already reproduced. The green spectrum included the first 6 terms in the sum and the red spectrum the first 10 (the red spectrum is the same one used in Figure 6.5). The difference between these is small, manifesting as only slight differences in resonance intensities in the cusps centered around 63 MHz offset.

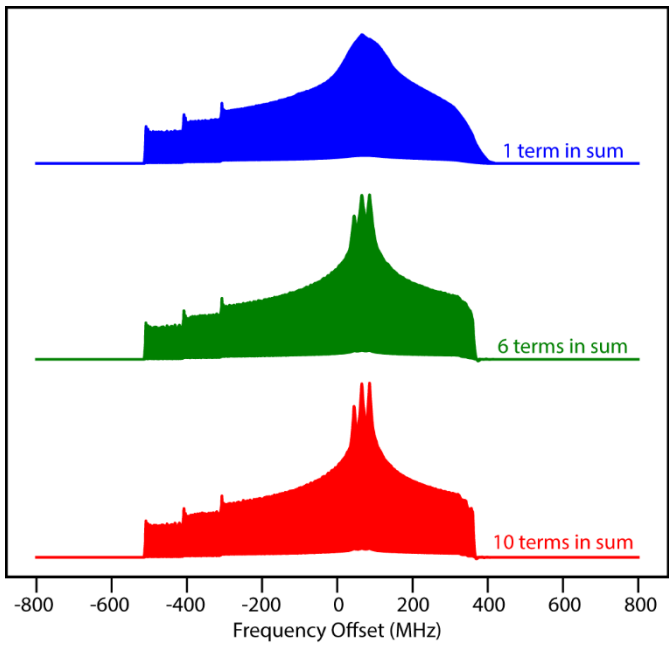

Figure 6.7: Simulations of the TEMPO powder pattern including the first term in Equation (6.40) (blue), the first 6 terms (green) and the first 10 terms (red). There is only a small difference between the one involving 6 terms and the one with 10 terms. The rapid convergence of the series in Equation (6.40) means that it can be heavily truncated to save time.

6.4 Conclusions

Simulations of electron-detected magnetic resonance spectra under magic angle spinning (MAS) are presented, which will be crucial to the design and implementation of sensitive new magnetic resonance experiments. The spectral width of EPR spectra compared with those typically observed in spin 1/2 NMR spectra are orders of magnitude larger, requiring large powder averages to accurately reproduce them. Here, expressions for the analytical averaging of the TEMPO powder pattern over the α Euler angle in both the static and MAS cases are derived.

In the static case, the simulation time is reduced by 97.5% over the fully numerical calculation. In the MAS case, the rapidly converging series derived here successfully reproduces the expected spinning sideband manifolds. Although the simulation strategies described here were used to calculate the spinning sideband manifold of a nitroxide electron spin, the theory is also applicable to theoretical analysis of conventional NMR pulse sequences which require powder averaging.

As electron nutation and MAS frequencies increase with improvements in microwave and spinning technology, future pulse sequences will be able to fully incorporate the electron spin into combined NMR and EPR experiments. For instance, MAS EPR detection will enable sensitive detection of electron spins which encode nuclear coherences. The fast analytical powder averaging and simulation techniques shown here will play an impactful role in describing experiments involving electron detected MAS NMR, and its implementation with other techniques, such as pulsed DNP and electron decoupling[14–17].

References

(1) Rossini, A. J.; Widdifield, C. M.; Zagdoun, A.; Lelli, M.; Schwarzwälder, M.; Copéret, C.; Lesage, A.; Emsley, L. Dynamic Nuclear Polarization Enhanced NMR Spectroscopy for Pharmaceutical Formulations. *J. Am. Chem. Soc.* **2014**, *136* (6), 2324–2334.

(2) Hayes, S.; Van Wüllen, L.; Eckert, H.; Even, W. R.; Crocker, R. W.; Zhang, Z. Solid-State NMR Strategies for the Structural Investigation of Carbon-Based Anode Materials. *Chem. Mater.* **1997**, *9* (4), 901–911.

(3) Baker, L. A.; Sinnige, T.; Schellenberger, P.; de Keyzer, J.; Siebert, C. A.; Driessen, A. J. M.; Baldus, M.; Grünewald, K. Combined 1H-Detected Solid-State NMR Spectroscopy and Electron Cryotomography to Study Membrane Proteins across Resolutions in Native Environments. *Structure* **2018**, *26* (1), 161-170.e3.

(4) Mak-Jurkauskas, M. L.; Bajaj, V. S.; Hornstein, M. K.; Belenky, M.; Griffin, R. G.; Herzfeld, J. Energy Transformations Early in the Bacteriorhodopsin Photocycle Revealed by DNP-Enhanced Solid-State NMR. *Proc. Natl. Acad. Sci.* **2008**, *105* (3), 883–888.

(5) Yang, H.; Staveness, D.; Ryckbosch, S. M.; Axtman, A. D.; Loy, B. A.; Barnes, A. B.; Pande, V. S.; Schaefer, J.; Wender, P. A.; Cegelski, L. REDOR NMR Reveals Multiple Conformers for a Protein Kinase c Ligand in a Membrane Environment. *ACS Cent. Sci.* **2018**, *4* (1), 89–96.

(6) Levitt, M. H. *Spin Dynamics*, 2nd ed.; John Wiley & Sons Ltd.: West Sussex, 2008.

(7) Bax, A.; Freeman, R. Investigation of Complex Networks of Spin-Spin Coupling by Two-Dimensional NMR. *J. Magn. Reson.* **1981**, *44* (3), 542–561.

(8) Reid Alderson, T.; Charlier, C.; Torchia, D. A.; Anfinrud, P.; Bax, A. Monitoring

Hydrogen Exchange during Protein Folding by Fast Pressure Jump NMR Spectroscopy. *J. Am. Chem. Soc.* **2017**, *139* (32), 11036–11039.

(9) Bertarello, A.; Jaudzems, K.; Herrmann, T.; Hiller, M.; Griffin, R. G.; Franks, W. T.; Chou, J. J.; Tars, K.; Akopjana, I.; Emsley, L.; et al. Rapid Proton-Detected NMR Assignment for Proteins with Fast Magic Angle Spinning. *J. Am. Chem. Soc.* **2014**, *136* (35), 12489–12497.

(10) Zhou, D. H.; Shah, G.; Cormos, M.; Mullen, C.; Sandoz, D.; Rienstra, C. M. Proton-Detected Solid-State NMR Spectroscopy of Fully Protonated Proteins at 40 KHz Magic-Angle Spinning. *J. Am. Chem. Soc.* **2007**, *129* (38), 11791–11801.

(11) Andreas, L. B.; Jaudzems, K.; Stanek, J.; Lalli, D.; Bertarello, A.; Le Marchand, T.; Cala-De Paepe, D.; Kotelovica, S.; Akopjana, I.; Knott, B.; et al. Structure of Fully Protonated Proteins by Proton-Detected Magic-Angle Spinning NMR. *Proc. Natl. Acad. Sci. U. S. A.* **2016**, *113* (33), 9187–9192.

(12) Lesage, A. Recent Advances in Solid-State NMR Spectroscopy of I=1/2 Nuclei. *Phys. Chem. Chem. Phys.* **2009**, *11*, 6876–6891.

(13) Zhou, D. H.; Shea, J. J.; Nieuwkoop, A. J.; Franks, W. T.; Wylie, B. J.; Mullen, C.; Sandoz, D.; Rienstra, C. M. Solid-State Protein-Structure Determination with Proton-Detected Triple-Resonance 3D Magic-Angle-Spinning NMR Spectroscopy. *Angew. Chemie - Int. Ed.* **2007**, *46* (44), 8380–8383.

(14) Saliba, E. P.; Sesti, E. L.; Scott, F. J.; Albert, B. J.; Choi, E. J.; Alaniva, N.; Gao, C.; Barnes, A. B. Electron Decoupling with Dynamic Nuclear Polarization in Rotating Solids. *J. Am. Chem. Soc.* **2017**, *139* (18).

(15) Sesti, E. L. .; Saliba, E. P. .; Alaniva, N.; Barnes, A. B. Electron Decoupling with Cross

Polarization and Dynamic Nuclear Polarization below 6 K. *J. Magn. Reson.* **2018**, *295*, 1–5.

(16) Saliba, E. P.; Sesti, E. L.; Alaniva, N.; Barnes, A. B. Pulsed Electron Decoupling and Strategies for Time Domain Dynamic Nuclear Polarization with Magic Angle Spinning. *J. Phys. Chem. Lett.* **2018**, *9*, 5539–5547.

(17) Alaniva, N.; Saliba, E. P. .; Sesti, E. L.; Judge, P. T.; Barnes, A. B. Electron Decoupling with Chirped Microwave Pulses for Rapid Signal Acquisition and Electron Saturation Recovery. *Angew. Chemie* **2019**, *0* (just accepted).

(18) Becerra, L. R.; Gerfen, G. J.; Temkin, R. J.; Singel, D. J.; Griffin, R. G. Dynamic Nuclear Polarization with a Cyclotron Resonance Maser at 5 T. *Phys. Rev. Lett.* **1993**, *71* (21), 3561–3564.

(19) Tan, K. O.; Yang, C.; Weber, R. T.; Mathies, G.; Griffin, R. G. Time-Optimized Pulsed Dynamic Nuclear Polarization. **2019**, No. January, 1–8.

(20) Doll, A.; Bordignon, E.; Joseph, B.; Tschaggelar, R.; Jeschke, G. Liquid State DNP for Water Accessibility Measurements on Spin-Labeled Membrane Proteins at Physiological Temperatures. *J. Magn. Reson.* **2012**, *222*, 34–43.

(21) Batel, M.; Däpp, A.; Hunkeler, A.; Meier, B. H.; Kozerke, S.; Ernst, M. Cross-Polarization for Dissolution Dynamic Nuclear Polarization. *Phys. Chem. Chem. Phys.* **2014**, *16* (39), 21407–21416.

(22) Lee, D.; Bouleau, E.; Saint-Bonnet, P.; Hediger, S.; De Paëpe, G. Ultra-Low Temperature MAS-DNP. *J. Magn. Reson.* **2016**, *264*, 116–124.

(23) Nesbitt, D. J.; Suhm, M. A.; Chem, P.; Winnewisser, B. P.; Winnewisser, M.; Ivan, R.; Lucia, F. C. De; Ross, S. C.; Kunitski, M.; Knippenberg, S.; et al. This Paper Is Published

as Part of a PCCP Themed Issue on Chemical Dynamics of Large Amplitude Motion. *Phys. Chem. Chem. Phys.* **2010**.

(24) Kubicki, D. J.; Rossini, A. J.; Purea, A.; Zagdoun, A.; Ouari, O.; Tordo, P.; Engelke, F.; Lesage, A.; Emsley, L. Amplifying Dynamic Nuclear Polarization of Frozen Solutions by Incorporating Dielectric Particles. *J. Am. Chem. Soc.* **2014**, *136* (44), 15711–15718.

(25) Wang, X.; Caulkins, B. G.; Riviere, G.; Mueller, L. J.; Mentink-Vigier, F.; Long, J. R. Direct Dynamic Nuclear Polarization of 15 N and 13 C Spins at 14.1 T Using a Trityl Radical and Magic Angle Spinning. *Solid State Nucl. Magn. Reson.* **2019**, *100* (March), 85–91.

(26) Kwikam, A. L. Electron Nuclear Double Resonance. *Annu. Rev. Phys. Chem.* **1971**, *700* (22), 133–170.

(27) Rowan, L. G.; Hahn, E. L.; Mims, W. B. Electron-Spin-Echo Envelope Modulation. *Phys. Rev.* **1965**, *137* (1), A61–A71.

(28) Waugh, J. S. Rotational Spin Echoes And High Resolution NMR in Powders. **1976**, *47* (2), 1–3.

(29) McHaourab, H. S.; Steed, P. R.; Kazmier, K. Toward the Fourth Dimension of Membrane Protein Structure: Insight into Dynamics from Spin-Labeling EPR Spectroscopy. *Structure* **2011**, *19* (11), 1549–1561.

(30) Edén, M. Computer Simulations in Solid-State NMR. III. Powder Averaging. *Concepts Magn. Reson. Part A Bridg. Educ. Res.* **2003**, *18* (1), 24–55.

(31) Bak, M.; Nielsen, N. C. Repulsion, A Novel Approach to Efficient Powder Averaging in Solid-State NMR. *J. Magn. Reson.* **1997**, *125* (1), 132–139.

(32) Mueller, K. T. Analytic Solutions for the Time Evolution of Dipolar-Dephasing NMR

Signals. *Journal of Magnetic Resonance, Series A*. 1995, pp 81–93.

(33) Young, R. P.; Lewis, C. R.; Yang, C.; Wang, L.; Harper, J. K.; Mueller, L. J. TensorView: A Software Tool for Displaying NMR Tensors. *Magn. Reson. Chem.* **2018**, No. September, 211–223.

(34) Radeglia, R. On the Pictorial Representation of the Magnetic Screening Tensor: Ellipsoid or Ovaloid? *Solid State Nucl. Magn. Reson.* **1995**, *4* (5), 317–321.

(35) Hansen, A. E.; Bouman, T. D. Calculation, Display, and Analysis of the Nature of Nonsymmetric Nuclear Magnetic Resonance Shielding Tensors: Application to Three-Membered Rings. *J. Chem. Phys.* **1989**, *91* (6), 3552–3560.

(36) Jameson, C. J. Theoretical and Physical Aspects of Nuclear Shielding. In *Specialist Periodical Reports: Nuclear Magnetic Resonance, Volume 20*; Webbs, G. A., Ed.; Royal Society of Chemistry, 2007; p 50.

(37) Herzfeld, J.; Berger, A. E. Sideband Intensities in NMR Spectra of Samples Spinning at the Magic Angle. *J. Chem. Phys.* **1980**, *73* (12), 6021–6030.

(38) Bloembergen, N.; Rowland, T. J. On the Nuclear Magnetic Resonance in Metals and Alloys. *Acta Metall.* **1953**, *1* (6), 731–746.

(39) Mueller, L. J. Tensors and Rotations in NMR. *Concepts Magn. Reson. Part A* **2011**, *38A*, 221–235.

(40) Wenckebach, T. *Essentials of Dynamic Nuclear Polarization*; Spindrift Publications, 2016.

(41) González, Á. Measurement of Areas on a Sphere Using Fibonacci and Latitude-Longitude Lattices. *Math. Geosci.* **2010**, *42* (1), 49–64.

(42) Marques, R.; Bouville, C.; Ribardière, M.; Santos, L. P.; Bouatouch, K. Spherical

Fibonacci Point Sets for Illumination Integrals. *Comput. Graph. Forum* **2013**, *32* (8), 134–143.

(43) Alderman, D. W.; Solum, M. S.; Grant, D. M. Methods for Analyzing Spectroscopic Line Shapes. NMR Solid Powder Patterns. *J. Chem. Phys.* **2002**, *84* (7), 3717–3725.

(44) Ward, R.; Bowman, A.; Erman, S.; El Mkami, H.; Owen-Hughes, T. EPR Distance Measurements in Deuterated Proteins. *J. Magn. Reson.* **2010**, *207*, 164–167.

(45) El Mkami, H.; Ward, R.; Bowman, A.; Owen-Hughes, T.; Norman, D. G. The Spatial Effect of Protein Deuteration on Nitroxide Spin-Label Relaxation: Implications for EPR Distance Measurement. *Journal of Magnetic Resonance*. 2014, pp 36–41.

(46) Böckmann, A.; Ernst, M.; Meier, B. H. Spinning Proteins, the Faster, the Better? *J. Magn. Reson.* **2015**, *253*, 71–79.

(47) Jeschke, G.; Schweiger, A. Hyperfine Decoupling in Electron Spin Resonance. *J. Chem. Phys.* **1997**, *106* (24), 9979–9991.

Chapter 7: Conclusions and Outlook

7.1 Electron Decoupling

7.1.1 Conclusions

This dissertation describes the implementation of electron decoupling of the Trityl Finland with dynamic nuclear polarization (DNP) radical under magic angle spinning (MAS) using a frequency agile gyrotron. The frequency agility of the gyrotron allowed for the microwave frequency to be chirped through the Trityl electron resonance frequency following a period of DNP to produce the decoupling effect. Electron decoupling both narrows resonances and improves their integrated area[1–4].

Electron decoupling was demonstrated using both direct polarization of the ^{13}C from the electrons[1] and using indirect polarization with cross polarization (CP) by first transferring the electron polarization to the protons in the sample[2]. In the direct polarization case, a narrowing of 48 Hz was observed, with an improvement in integrated area of 13.84% at 0.5 s of polarization time[1]. Electron decoupling using CP showed a narrowing of 11 Hz with an improvement in integrated area of 5%[2]. The dependence of the degree of electron decoupling achieved was studied as a function of various parameters including the spinning frequency, polarization times, sweep time, and sweep width[1]. As higher microwave powers are made accessible through improved microwave technology, improved electron decoupling performance will be achieved.

7.1.2 Outlook

Access to ever higher electron nutation frequencies will allow for further improvements in electron decoupling to be made. For example, if sufficiently high adiabaticity factors can be achieved, full adiabatic inversions of the electron spins could be performed, fully averaging out the electron nuclear interactions. This could allow for direct transfer DNP to be performed while maintaining the high resolution that makes NMR such an invaluable technique.

7.2 Magic Angle Spinning Below 6 K with Liquid Helium

7.2.1 Conclusions

Electron decoupling with cross polarization (CP) was used in conjunction with MAS below 6 K. This was achieved by using liquid helium as a variable temperature fluid for MAS. In addition to the liquid helium, compressed helium gas was used for the bearing and drive gasses, to avoid the liquefaction and solidification of nitrogen that occurs at such temperatures. Performing experiments at such temperatures provides dramatic improvements in sensitivity through improved Boltzmann polarization and reduced noise in the NMR probe[2].

7.2.2 Outlook

The temperature that these experiments are performed at could potentially be lowered even further by lowering the pressure inside the probe head. This would cause the helium to boil at a lower temperature. The further reduction in temperature will improve the polarization of the spins in the system, leading to even better sensitivity.

7.3 Analytical Powder Averaging

7.3.1 Conclusions

Magnetic resonance simulations are commonly used to predict the outcome of experiments. When simulations are performed on solid powders, the time needed to perform the powder average can lead to very long simulation times. In this dissertation, solutions to the analytical powder averaging over the α Euler angle in both the static and magic angle spinning cases are derived. In the static case, use of analytical powder averaging leads to a 97.5% reduction in simulation time if the reduction in resources is considered along with the reduction in simulation time. In the magic angle spinning case, the computer code using the analytical powder averaging technique described successfully reproduces the expected spinning sideband manifold with the spinning sidebands separated by the simulated 150 kHz.

7.3.2 Outlook

Although the system simulated here was that of a TEMPO radical for electron detected magnetic resonance, the analytical powder averaging method is completely applicable to more common NMR techniques. Additionally, the analytical powder averaging strategy described could be used in a theoretical description of the mechanism of electron decoupling.

References

(1) Saliba, E. P.; Sesti, E. L.; Scott, F. J.; Albert, B. J.; Choi, E. J.; Alaniva, N.; Gao, C.; Barnes, A. B. Electron Decoupling with Dynamic Nuclear Polarization in Rotating Solids. *J. Am. Chem. Soc.* **2017**, *139* (18).

(2) Sesti, E. L. .; Saliba, E. P. .; Alaniva, N.; Barnes, A. B. Electron Decoupling with Cross Polarization and Dynamic Nuclear Polarization below 6 K. *J. Magn. Reson.* **2018**, *295*, 1–5.

(3) Alaniva, N.; Saliba, E. P. .; Sesti, E. L.; Judge, P. T.; Barnes, A. B. Electron Decoupling with Chirped Microwave Pulses for Rapid Signal Acquisition and Electron Saturation Recovery. *Angew. Chemie* **2019**, *0* (just accepted).

(4) Saliba, E. P.; Sesti, E. L.; Alaniva, N.; Barnes, A. B. Pulsed Electron Decoupling and Strategies for Time Domain Dynamic Nuclear Polarization with Magic Angle Spinning. *J. Phys. Chem. Lett.* **2018**, *9*, 5539–5547.